Reconfigurable RF-MEMS Capacitive SPST and SPDT Switches for Wireless Communication Systems

THESIS

Submitted in the partial fulfillment of the requirements for the degree of

DOCTOR OF PHILOSOPHY

by

MAHESH ANGIRA

Under the supervision of

Dr. KAMALJIT RANGRA

BIRLA INSTITUTE OF TECHNOLOGY & SCIENCE
PILANI – 333 031 (RAJASTHAN) INDIA

2016

BIRLA INSTITUTE OF TECHNOLOGY & SCIENCE

PILANI- 333031 (RAJASTHAN) INDIA

CERTIFICATE

This is to certify that the thesis entitled **" Reconfigurable RF-MEMS Capacitive SPST and SPDT Switches for Wireless Communication Systems"** submitted by **MAHESH ANGIRA,** ID. No**. 2008PHXF428P** for award of Ph.D. of the Institute embodies original work done by him under my supervision.

Signature in full of the Supervisor   **_____**

Name   : **Dr. Kamaljit Rangra**

Designation   : **Chief Scientist and Professor AcSIR**

                    Sensors and Nanotechnology Group

                    CSIR-Central Electronics Engineering Research Institute (CEERI), Pilani

Date   : _____

Dedicated

to

My Father

Acknowledgements

wonderful children Arnav, Aarav and wife Purna without whose love and support it would have been impossible to complete this work.

Mahesh Angira

Abstract

This thesis presents various design approaches of low pull-in voltage and multi-band reconfigurable RF-MEMS capacitive switches, which are analyzed by using simulations and are fabricated using surface micromachining techniques. The work is inspired by the superior performance of electrostatic RF MEMS switches over the state-of-the-art solid-state devices. In any communication system, switches consume a significant part of the power budget. RF MEMS switches with virtually zero dc power consumption, excellent RF performance and their small size have many applications in electronic communication. This work focuses on the limitations of MEMS capacitive switches, such as high actuation voltage and low capacitance ratio. To obviate the above issues, various designs have been investigated for capacitive shunt RF-MEMS switches.

In a conventional approach based design, the switch is implemented with a non-uniform bridge structure. The device shows an insertion loss better than 0.8 dB and return loss below 9 dB up to 25 GHz. For improving the ON-state response, a floating metal based switch has been designed. The device shows the insertion loss of ≈ 0.1 dB and return loss below 26.3 dB up to 25 GHz. The bandwidth is also increased by around 2.5 times than the conventional switch. In an alternative approach, a switch based on a high-k dielectric material (HfO_2) has been explored. However, the above devices are suitable for single band applications and are not compatible with multi-band wireless systems. To overcome this issue, the current study presents novel reconfigurable multi-band switches based on non-uniform cantilever based structures, where the optimum value of isolation has been shifted to different frequency bands. For symmetric structures based design, the optimum value of isolation has been tuned to C and X bands, whereas for asymmetric structures, it is tuned to C, X and K bands. For wideband applications, a combination of metal-to-metal contact switch and capacitive switch has been used. The proposed design shows the insertion loss better than 0.4 dB and return loss below 14 dB up to 30 GHz as compared to conventional switch, where 1.65 dB is the insertion loss and 6.2 dB is the return loss. Isolation peaks of 75.33, 71.58 and 72.98 dB have been observed at 8.2, 7.3 and 15.5 GHz when left, right or both cantilevers are electrostatically actuated in the down-state respectively, while conventional switch had only one peak at 7.0 GHz. Further, a reduction of about 60 % in the pull-in voltage of capacitive switch and 17.5 % in device area have been observed in the proposed design. As an application, switches

have been used to implement the SPDT device. The above discussed switches are fabricated at CSIR-CEERI, Pilani.

Keywords: Asymmetric structures, Capacitive shunt switch, Cantilever structure based switches, Multi-band, Metal-to-Metal contact switch, RF-MEMS, Series-shunt configuration, SPDT, Surface micromachining.

Table of Contents

Contents	Page No.

List of Tables

List of Figures

List of Abbreviations

Abbreviations	Description
MEMS	Micro Electro Mechanical Systems
MST	Micro System Technology
RF	Radio Frequency
RFIC	Radio Frequency Integrated Circuit
RF-MEMS	Radio Frequency Micro Electro Mechanical Systems
Bi CMOS	Bipolar Complementary Metal Oxide Semiconductor
PECVD	Plasma Enhanced Chemical Vapor Deposition
CPW	Coplanar Waveguide
DC	Direct Current
FET	Field Effect Transistor
PIN	Positive-Intrinsic-Negative
SPST	Single-pole Single-throw
SPDT	Single-pole Double-throw
LNA	Low Noise Amplifier
1-D	One-dimensional
2-D	Two-dimensional
3-D	Three-dimensional
HFSS	High Frequency Structure Simulator
SEM	Scanning Electron Microscope
MIM	Metal-Insulator-Metal
FEM	Finite Element Method
LPCVD	Low Pressure Chemical Vapor Deposition
TEOS	Tetraethylorthosilane
LTO	Low Temperature Oxidation
PVD	Physical Vapor Deposition
C-V	Capacitance-Voltage

Chapter - 1

Introduction

1.1 MEMS Technology

Micro Electro Mechanical Systems is a technology used to fabricate devices and systems based on a multidisciplinary approach. This technology is known by a wide variety of names in different parts of the world, e.g. in the United States it is known as Micro Electro Mechanical Systems (MEMS), in Europe as Micro System Technology (MST), and in Japan it is named Micromechanics. Device fabrication is based on a traditional, highly developed and optimized integrated circuits batch processing techniques and has size in the range of micrometers to millimeters. In addition, it includes comparatively new unit processes like surface and bulk micromachining. Silicon micromachining is the technique in which mechanical or structural layers are fabricated through thin film deposition techniques on the wafer surface and sacrificial layers. Finally, the sacrificial layer is etched using dry or wet techniques to obtain hanging or suspended structures. Bulk micromachining is the technique in which structures are etched into the silicon substrate by wet or dry etching techniques. This technique is mainly used in pressure sensors, silicon valves and accelerometers. The interdisciplinary nature of MEMS utilizes expertise from a wide and diverse range of technical areas including integrated circuit fabrication technology, mechanical engineering, materials science, electrical engineering, chemistry and chemical engineering, as well as fluid engineering, optics, instrumentation and packaging [1-4].

MEMS technology was initiated in 1970s and has been developed for accelerometers, gyroscopes and pressure sensors. MEMS technology has spread in several application fields, such as in the automotive industry, healthcare industry, aerospace industry, consumer products, and telecommunications. Some of the most successful MEMS devices are accelerometers for the automotive industry, ink-jet printheads, devices for information storage, such as the IBM millipede. MEMS devices can be divided into four classes on the basis of their mechanical complexity [5]. Table 1.1 shows the classification and the corresponding devices. Beyond its mature adoption in the sensors and actuators fields, MEMS technology exhibits an enormous potential in telecommunication systems, it being the main focus of this thesis.

Tables 1.1: Classification of MEMS devices in terms of their mechanical complexity.

Category	Devices
1. No moving structures	Pressure sensors, strain gauges
2. Moving structures, but no rubbing and impacting surfaces	Gyroscopes, resonators, and filters
3. Moving structures and impacting surfaces	RF switches (ohmic and capacitive)
4. Moving structures and impacting and rubbing surfaces	Gear, micro-locking mechanisms, and micro motors

1.2 RF-MEMS Technology

In recent years, telecommunication industries have been growing at a rapid pace. New wireless standards are coming up which require replacement of bulky, expensive and off-chip passive RF components with small size, high linearity, low power consumption and multi-band devices to ensure reconfigurability of the front-end without compromising the performance and cost of the system. Despite many years of research, RFIC technologies, including BiCMOS, SiGe and GaAs were not able to deliver the high quality factor of discrete passive components. RF-MEMS technology has paved the way for the development of such devices. As shown in Fig. 1.1, the front-end of a super-heterodyne wireless transceiver typically contains a good number of off-chip, high-Q components that are potentially replaceable by their micromachined versions. MEMS replaceable transceiver components are highlighted with coloured blocks. Among the components targeted for replacement are RF filters, including image rejection filters, tunable capacitors, high-Q inductors, resonators, tunable filters, oscillators, and switches for transmitter/receiver selection.

For higher frequency applications e.g., past X-band (8-12 GHz), antenna size become so small that it can be manufactured using micromachining techniques. In addition to the device size reduction as compared to the off-chip counterpart, the technology also offers monolithic integration of various RF-MEMS components leading to further miniaturization and cost reduction. The above cited devices constitute the fundamental building blocks of radio frequency applications and are most vigorously pursued by academic and industrial research communities. In general the outstanding performance of

the RF-MEMS is due to the air gap between the active elements and lossy substrate, use of high conductivity metals and integration compatibility with existing IC fabrication technologies. For example, on-chip inductor with quality factor of 57 at 10 GHz has been micromachined with spirals suspended over a gap of 50 microns from the bottom substrate. Due to its outstanding performance, RF-MEMS has immense potential for commercial and defense applications. One of the most important components in the RF/Microwave applications is RF-MEMS switch [7-11].
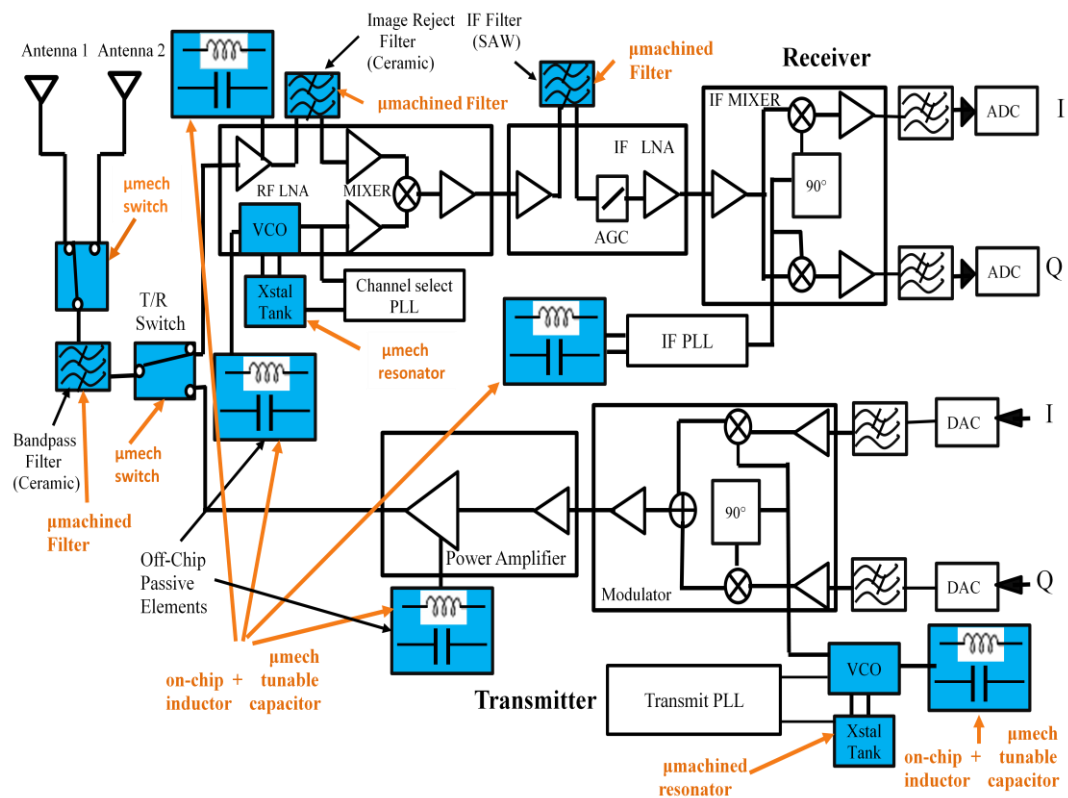
Figure 1.1: System level schematic detailing the front-end design for a typical wireless transceiver [6].

1.2.1 RF-MEMS Switches

RF-MEMS switches are basically used to place a short circuit or an open circuit in the RF transmission line. They are essentially the miniaturized form of the bulky mechanical RF relay, where switching between the ON and OFF states is achieved through the displacement of a movable structure. The displacement is usually generated from the electrostatic forces. MEMS switches outperform the solid-state switches such as FETs and PIN diodes. They show very low insertion loss and high isolation respectively due to the high conductivity of the metal and 1-3 μm of air gap. As metal beams are used for

switching purpose, the inevitable non-linearity in the I-V characteristics associated with solid-state devices is also non-existent. The RF-MEMS switches require negligible power consumption and thus can be used in many telecommunication systems, including cellular base stations, mobile handsets, radar, missile systems, satellite communication systems and automobiles. The switches are mostly used for RF signal routing, e.g. selecting the right antenna for switching between the transmitter and receiver paths, or routing signals to the different blocks in multi-band mobile phones. They also serve as fundamental building blocks for tunable filters, multiport switches, phase shifters, switch matrix and thus has been chosen as the topic of research for this thesis [6, 9].

1.3 Motivation

A switch is the most basic and essential component of any communication system. The ubiquitous switches consume a significant part of the power budget. Thus the selection of appropriate technology, cost, size, and RF performance becomes very critical. The current state-of-the-art RF circuit designs use a combination of mechanical switches (coaxial and waveguide) and solid-state switches (FETs, PIN diodes) to realize the switching function. Semiconductor switches are smaller in size, weight and provide much faster switching speed, but are inferior in terms of insertion loss, dc power consumption, isolation and power handling to their mechanical counterparts. MEMS switches offer the performance advantages of both mechanical and semiconductor switches. They offer high RF performance and low dc power consumption of mechanical switches, and small size, weight and low fabrication cost of semiconductor switches. In many cases, a single MEMS component can replace and outperform an entire solid-state circuit, e.g. low loss, high isolation and with negligible dc power consumption RF-MEMS switches can eliminate the need for an amplifier stage in T/R modules and thus result in considerable power saving and size reduction. The above cited points are the motivations for carrying out research in the RF-MEMS field, particularly in RF-MEMS switches.

1.4 The Problem, Objective and Methodology

MEMS switches show remarkable advantages over their solid-state counterparts such as low insertion loss, high isolation, less power consumption and high linearity. RF-MEMS switches have their share of problems and couldn't be used in every telecommunication

application. Pull-in voltage, switching time and power handling capability are the major shortcomings of the RF-MEMS switches. There is also scope for improving the RF performance parameters (insertion loss, isolation and bandwidth) when switches are used as building blocks for tunable filters, multiport switches, phase shifters and switch matrix because of the combined effect of multiple switches. Further, the modern RF systems also need the reconfigurable front end. This can significantly reduce the number of components, hardware complexity, and cost of the system. MEMS technology based RF devices could provide a potential solution in the above cited areas without compromising the performance.

The main objectives of the thesis and adopted approaches are as follows:

- **To design RF-MEMS switches having pull-in voltage ranging from 3 to 12 V.**

    The switches with high pull-in voltage are impractical for many wireless applications as the additional requirement for up-converters increase the system size. Further, for capacitive switches, high electric field of the order of 3-5 MV/cm across the dielectric layer (80-100 nm) leads to charge injection into the dielectric which dominates the stiction mechanism and reduces the device reliability. The charge injection is exponential with applied voltage. A reduction of 6 V results in a ten-fold increase in the lifetime of a MEMS switch, whereas low pull-in voltage based switches have stiction and self biasing problems. The stiction in the down state is due to the electrostatic force, the capillary force, hydrogen bonding, and Van der Waal forces. The pull-in voltage is a function of the beam spring constant, air gap and actuation area. For reducing the pull-in voltage, low height and cantilever structure based switches are designed. For alleviating the stiction, self and hold down problems, the transmission line is kept at a height of 0.5 μm above the actuation electrodes and a floating metal layer is used to minimize overlap area between the central conductor of CPW and hanging structure. The designed switches have pull-in voltage ranging from 3 V to 12 V.

- **To design RF-MEMS switches having insertion loss ≤ 0.1 dB and isolation ≥ 20 dB in X-band.**

In shunt capacitive switch, ON and OFF-state can be achieved by changing the value of capacitance between the movable structure and the transmission line. Thus a figure of merit is the ratio of capacitance in the down to up-state position of the movable beam. A high capacitance ratio is required for better isolation and insertion characteristics. However, degraded capacitance in the down-state due to surface micro-roughness decreases the capacitance ratio. This also makes the down-state behavior unpredictable in terms of resonant frequency. The issue has been addressed by introducing a floating metal layer. This also allows reduction of the RF overlap area between the movable structure and central conductor of CPW without affecting the down-state response and thus improves the ON-state response of the device. The switches based on floating metal concept have insertion loss < 0.1 dB and isolation > 30 dB, whereas at the SPDT level insertion loss < 0.5 dB and isolation > 20 dB for *X*-band applications.

- **To design reconfigurable multi-band switches**

  The modern RF systems require reconfigurable multi-band microwave components as theses components allow increased system functionality with lower weight, cost and consume less chip area. A number of structures have been reported in the literature for capacitive switches having good RF performance in a single band. However, these devices lag in multi-band functionality. This thesis presents novel reconfigurable multi-band shunt capacitive switches based on a non-uniform cantilever structures. Further, both symmetric and asymmetric structures have been used on the either side of the transmission line. The cantilever structure based capacitive switch has also been used to implement the reconfigurable multi-band SPDT device.

1.5 Novelty

This thesis presents novel designs for the performance enhancement of the electrostatically actuated capacitive shunt RF-MEMS switches. Switches have asymmetric structure on either side of the transmission line. Different shapes of non-uniform cantilevers are used to introduce asymmetry, which changes the inductance in the down-state of the switch. The following points support the novelty in the presented work.

- The inductance value can be changed by the actuating either left, right or both cantilevers to the down-state. This control over the down-state inductance value can't be achieved with the capacitive switches reported in the literature.

- As the resonant frequency (f_o) $= \frac{1}{2\pi\sqrt{LC}}$ is dependent on the L and C, where L and C are the inductance and capacitance in the down-state of the switch, thus by changing the inductance in the down-state, the isolation peaks have been tuned to the different frequency bands, whereas traditional capacitive switches have only single optimum value. Therefore, presented switch can work in different bands with optimal value of isolation in that band.

- Further, for improving the ON-state response beam active area has been reduced by incorporating a floating metal layer. This has been done without affecting the OFF-state response.

- For reducing the pull-in voltage capacitive switches are implemented with non-uniform cantilever based structures.
- The cantilever structure based capacitive switch has been used to implement the reconfigurable multi-band SPDT switch.

1.6 Thesis Organization

This thesis is divided into seven chapters. The organization of this thesis is as follows:

Chapter 1 gives an introduction for the MEMS and RF-MEMS technology. The thesis problem is defined in this chapter. Further the objectives and methodology are also covered. This chapter also talks about the contributions of this thesis in the RF-MEMS field.

Chapter 2 introduces the different switching technologies for RF applications. The main emphasis of this chapter is to briefly explain the working of RF-MEMS technology based switches and their types. A comparison of the solid-state vs. RF-MEMS switches are also covered in the tabular form. This chapter also discusses the state-of-the-art devices and general motivation for research in the RF-MEMS switches area.

Chapter 3 presents the design aspects of the switches in the different domain, i.e. mechanical, electromechanical and RF. Under mechanical response, spring constant and in the electromechanical response pull-in voltage and switching time has been discussed. Under RF domain, the electrical behavior of a capacitive device has been studied through the lumped equivalent model of the switch. A capacitive switch based on conventional approach has been designed and the response has been compared with floating metal based design. This chapter also presents the devices based on interdigitated topology with HfO_2 as a dielectric material.

Chapter 4 deals with the reconfigurable multi-band capacitive switches. Mainly two approaches are discussed in this chapter, a bridge structure anchored in between ground planes and attached to two cantilevers on either side of the transmission line and non-uniform cantilever based switch anchored on the ground plane. A model for spring constant of the non-uniform cantilever is derived through basic force deflection calculation. The non-uniform beam, which is wider at the electrode area and narrower at the anchor area, is used to reduce the pull-in voltage. Further, a broadband switch based on series-shunt topology has been investigated. This device also has the capability of shifting the OFF-state isolation optimum value to the different bands.

Chapter 5 presents the design of SPDT device based on capacitive switches. Initially, SPDT has been designed using conventional capacitive switch and the response has been compared with the SPDT implemented using cantilever structure based switch. Further, a reconfigurable multi-band SPDT using cantilever structure based switch is also discussed.

Chapter 6 presents the fabrication process flow for RF-MEMS switches. The fabricated structures show out of plane deformation due to the residual stress, which affects the performance of the switches. Under device measurements, the gap between the hanging structure and transmission line is measured using the 3-D optical profiler and the mechanical resonant frequency is measured using the Laser Doppler Vibrometer (LDV).

Chapter 7 concludes the thesis work by highlighting the contribution made in RF-MEMS switches area and discusses scope for future work.

Capacitive Switch

Ohmic Switch

Capacitive Switch
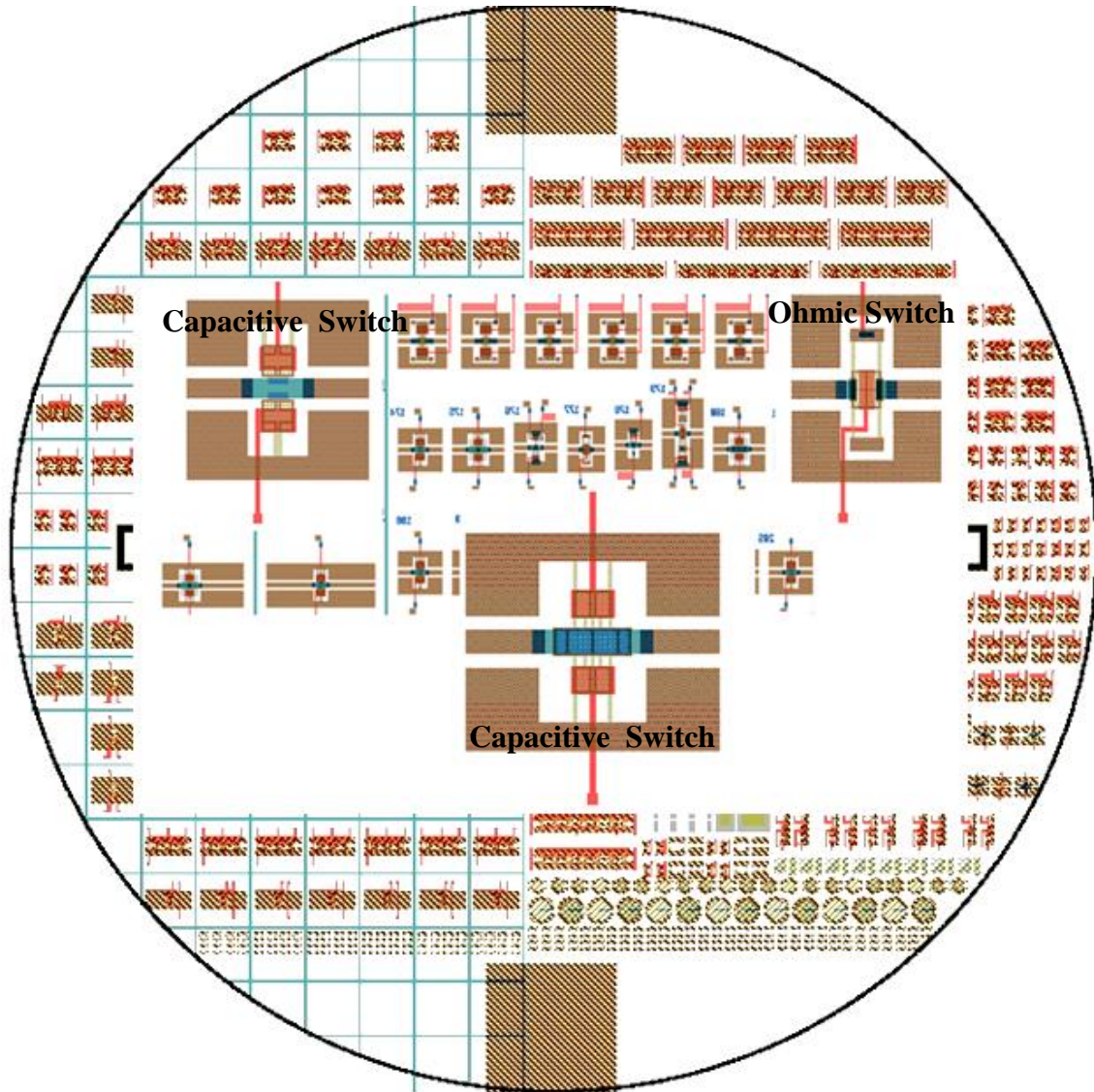
Chapter - 2

Background and Literature Review

2.1 Introduction

This chapter provides a basic introduction to RF switches and their applications. Different technology based RF switches that are currently used for RF applications are first introduced. Then, a more detailed survey of RF-MEMS switches is covered. This chapter also covers the comparison of the RF-MEMS switches with state-of-the-art solid-state switches.

2.2 Switches for RF Applications

RF switch is a device used for achieving a short circuit or an open circuit in the RF transmission line. The main use of RF switches is in signal routing. Telecommunication applications cover a broad range of frequencies, ranging from MHz to GHz. In this broad spectrum, switch specifications can vary with the change in the operating frequency. This can also bring changes in the switching technology. There are many parameters that decide the selection of an appropriate technology for a particular RF application. These are insertion loss, isolation, bandwidth, RF power handling, resonant frequency, switching time and actuation voltage [12, 13].

Currently in RF applications, either mechanical, semiconductor or MEMS technology based switches are being used. The selection of a switching technology for a particular application is decided according to the above discussed parameters, e.g. in some applications high power handling is required, thus a mechanical switch can be used for this type of requirement [14], in some areas very high speed is required with moderate isolation and low insertion loss and power handling is not an issue, thus PIN diodes or FETs can be used for this purpose [6, 12], whereas some applications require high isolation, low insertion, negligible dc power consumption are required with moderate speed and hence MEMS switches are best candidates to fulfill this criteria [6, 12]. But each technology has its own set of pros and cons. In the case of the solid-state switches, they operate well at low frequencies, but at high frequencies, these devices have a high insertion loss and poor isolation. In case of the mechanical coaxial and waveguide switches, they offer the advantage of low insertion loss, high isolation, large power

handling and high linearity, but are heavy and slow. On the other hand semiconductor switches provide faster switching speed and are smaller in size, but have inferior RF performance than mechanical coaxial switches [6, 12]. For the above cited problem, the best remedy can be the use of MEMS technology based switches. MEMS switches provide the advantages of both mechanical and semiconductor switches and thus can replace many of the microwave switches in today's communication systems.

2.3 RF-MEMS Switches

A MEMS switch is a micro scaled mechanical device with two stable states. The device allows the propagation of an RF signal from the input to the output in one state and blocks the signal in the other state. Switching between the states is achieved through the mechanical movement of a hanging structure essentially a cantilever or bridge anchored at the one or both ends respectively. The movement can be induced through different types of actuation mechanisms, e.g., electrostatic, piezoelectric, thermal or magnetic actuation. Majority of switches reported in the literature use electrostatic actuation due to low power consumption.

Table 2.1: Different Configurations of RF-MEMS Switches

Actuation Mechanism	Type of Contact	Circuit Configuration	Movement
Electrostatic	↑	↑	↑
	Metal-to-Metal	Series	Vertical
Thermal			
	Capacitive	Shunt	Lateral
Magnetostatic			
Piezoelectric	↓	↓	↓

The other advantages of using electrostatic actuation are low fabrication complexity, compact size, possibility of biasing the switch using high resistance bias lines and easy integration with coplanar waveguide and microstrip lines. Table 2.1 tabulates the different configurations of RF-MEMS switches [6]. The series metal-to-metal contact switch is generally preferred for the applications with operating frequency from dc to C-band (4-8 GHz), whereas the capacitive shunt device is suitable for further higher frequencies [9, 11] .

2.3.1 Electrostatically Actuated Ohmic Series Switch

The Series ohmic switch is based on the same principle as the simple mechanical moving switch. The beam moves mechanically when actuated to close the switch. Switches of this category are normally OFF, and the incoming RF wave is reflected by the interrupted signal line in the OFF-state. In this type of switch, beam can be placed either in broadside or inline relative to the RF signal line. The armature (bridge) is the integral part of the transmission line in the inline switching device and the actuation is in the same plane as the transmission line. The signal enters at the fixed end, travels through the length of the cantilever beam and exits to the transmission line through the contacts at the end of the cantilever. For broadside configuration the switch is placed perpendicular to the signal line [15].
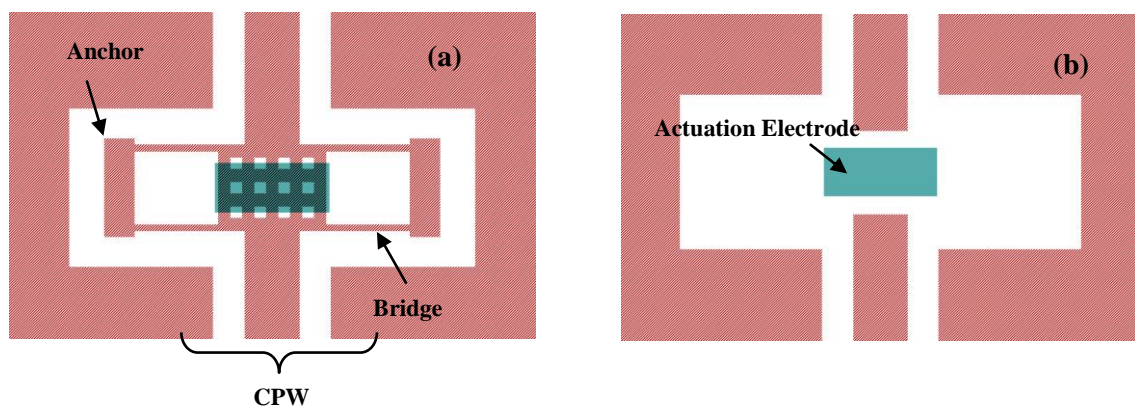
Figure 2.1: Series ohmic switch (a) Shows the bridge and anchor point (b) To highlight the actuation pad, bridge is removed.

The movable armature could be a metallic beam or a dielectric beam with metallic contact and can be configured as a single fixed end or a fixed-fixed type of structures. Figure 2.1 (a) shows series ohmic switch, where the bridge type structure is used for its implementation, whereas Fig. 2.1 (b) depicts the ohmic switch when bridge structure is removed for showing the underlying actuation electrode and interrupted signal line. This switch type is capable of switching dc to RF signals.

2.3.2 Electrostatically Actuated Capacitive Shunt Switch

A basic capacitive shunt switch consists of a movable metal bridge anchored on the ground plane of the coplanar waveguide (see chapter 3 for details on coplanar waveguide) as illustrated in Fig. 2.2. The dc control voltage and the RF signal are

superimposed and applied to the signal line. For shunt switches, the principle is based on capacitive coupling. There is a thin dielectric film on the signal line that prevents them from making a metal contact.
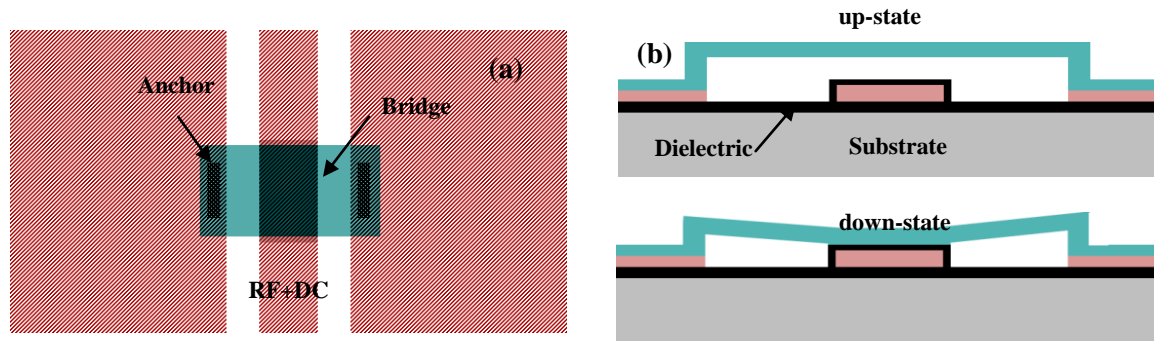
Figure 2.2: Shunt capacitive switch (a) Top view (b) Side view showing the two states.

The air gap is electrostatically adjusted to achieve a capacitance change between the up and down-state. As typical of shunt configuration the input and output RF ports are physically connected to each other through the transmission line and therefore normally switch is ON. By applying the dc voltage, bridge is pulled down and turns the ON switch OFF. Due to the capacitive coupling, this switch is not suitable for low frequency applications. A high down-state capacitance and a low up-state capacitance implies high isolation and a low insertion loss [6].

2.3.3 Separate Actuation Electrode Based Switch

The capacitive shunt switches are generally implemented as two terminal devices, where the dc control voltage is also applied to the signal line along with the RF signal. In three terminal switches, a separate dc electrode is provided for electrostatic actuation [16]. Both capacitive shunt and series contact type RF-MEMS devices discussed in this thesis are based on this approach. Capacitive switches of this type do not require biasing, decoupling elements and thus simplify the design and fabrication process. In addition, pull-in voltage can be made independent from the up-state capacitance.

2.4 Comparison between RF-MEMS Switches and Semiconductor Switches

RF-MEMS switches with virtually no mass, insensitive to acceleration, consuming no dc power, having cut-off frequency 30-50 times higher than semiconductor devices,

outstanding isolation and insertion loss at microwave frequencies and low manufacturing cost are the prime candidates for replacing existing semiconductor or mechanical counterparts. Table 2.2 shows a comparison between electrostatic MEMS switches, PIN diode and FET switches [6, 17]. It is evident that MEMS switches, with their extremely low up-state capacitance (series switches) and their very high capacitance ratio (capacitance contact switches), offer a far superior performance compared to solid-state switches for low to medium power applications. However, RF-MEMS Switches are slow as compared to their semiconductor counterpart.

Table 2.2: Comparison between RF-MEMS and semiconductor switches.

Parameter	RF-MEMS	PIN	FET
Voltage (V)	20-80	±3-5	3-5
Current (mA)	≈ 0	3-20	0
Power consumption (mW)	0.05-0.1	5-100	0.05-0.1
Switching time	1-300 µs	1-100 ns	1-100 ns
C_{up} (series) (fF)	1-6	40-80	70-140
R_s (series) (Ω)	0.5-2	2-4	4-6
Capacitance ratio	40-500[a]	10	N/A
Cut-off frequency (THz)	20-80	1-4	0.5-2
Isolation (1-10 GHz)	Very High	High	Medium
Isolation (60-100 GHz)	High	Medium	N/A
Insertion Loss (1-100 GHz) (dB)	0.05-0.2	0.3-1.2	0.4-2.5
Power Handling (W)	< 1	< 10	< 10

[a]Capacitive switch only

2.5 General Fabrication Process and Materials

The selection of materials and fabrication process is based on the compatibility with standard IC fabrication processes. Most of the reported switches, are fabricated using a four to five mask level process. The general steps for the fabrication of RF-MEMS capacitive switch are shown in the Fig. 2.3. A high resistivity Si substrate (> 3 kΩ-cm) is

the starting material. The thermal oxide layer is generally grown over the substrate to isolate it from the up-coming layers stack. The signal line and ground planes are fabricated in the *Au* or *Al* metal [16, 18-20]. A thin dielectric layer (0.1-0.3 μm) is deposited and patterned. Mostly PECVD Si_3N_4, or SiO_2 are preferred, but use of high-*k* dielectric materials such as HfO_2, $SrTiO_3$, Ta_2O_5 have also been demonstrated [21-24]. The next step is to deposit and pattern the spacer layer. The thickness of the spacer layer is decided by the air gap required air gap between the CPW and suspended structure. The positive photoresist or polyamide is generally selected as the material for spacer layer. The next step is to deposit and pattern the spacer layer. The hanging structure is defined by depositing and patterning around 1-2 μm thick metal layer over the sacrificial layer. This followed by the removal of sacrificial layer using an isotropic dry etch in oxygen plasma to avoid the stiction. In case of ohmic switch, dielectric deposition step is replaced by a contact metal.

Si   Dielectric   Metal   Dielectric   Spacer
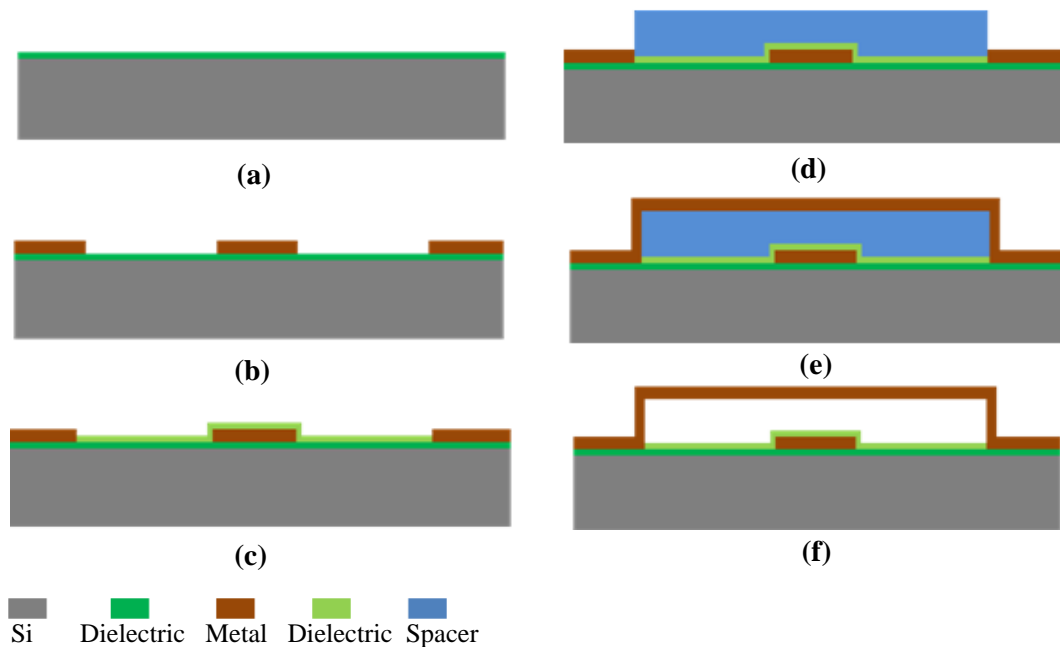
Figure 2.3: Fabrication process sequence for RF-MEMS capacitive switch

2.6 Applications of RF-MEMS Switches

MEMS switches are used to select the electrical signal, e.g. the incoming and the outgoing signal of an antenna, or to reconfigure a sub-system. Typical applications include the switching of filter banks, tuning of filters, switching of delay lines in phase-shifters, impedance matching, switch matrix and in reconfigurable antenna. Depending on the frequency, either shunt capacitive or series metal contact switches are preferred

for certain applications. The series metal-to-metal contact switch is generally used for below C-band, whereas the capacitive shunt device is suitable for the further higher frequencies. A few of the important applications are briefly described as follows.

2.6.1 Digitized Capacitor Banks

Figure 2.4 shows an example for use of MEMS switches in digital capacitor banks. This is a promising way to get a variable capacitance although not with continuous variability, but with high linearity and high-Q factor up to microwave frequencies. Existing semiconductor devices can provide continuous tunability of capacitance up to very high frequencies e.g. back-biased Schottky diodes. However, the quality factor is limited to the values less than 10 because of the significant conductance in semiconductor devices. The schematic diagram of a binary capacitor bank has been made by using the air-bridge metal–insulator–metal structure as a capacitance bit. Due to this the ratio of unactuated to actuated capacitance is so large, typically 100 in this structure. A multi-bit capacitance bank is then formed by fabricating other structures with a binary relationship in the area, and connecting them in parallel [25].
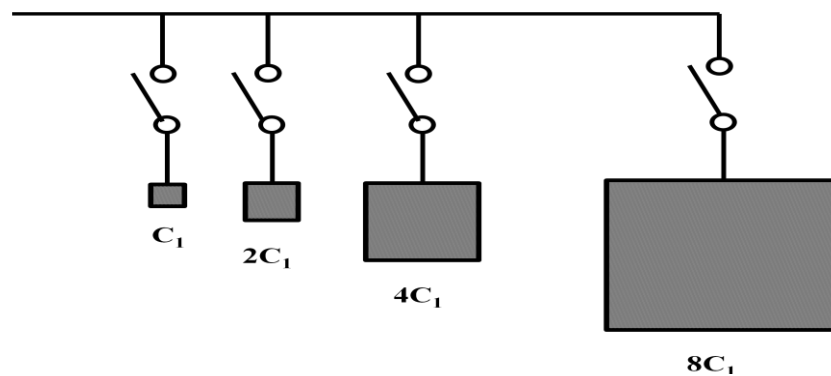
Figure 2.4: A 4-bit capacitance bank connected to an external circuit through MEMS switches.

2.6.2 Switching Networks

Switching networks are used in every communication system. In satellite systems, the switching networks are built using coaxial switches while in base station systems, they are implemented using PIN diodes. Coaxial switches result in outstanding isolation and insertion loss. However, they are heavy and costly. A typical satellite has around 100-300 switches depending on the configuration, and the switching network itself can cost millions of dollars per satellite. RF-MEMS switches can easily meet the RF performance

and result in much smaller and lighter systems which is essential for satellite applications [6, 9].

2.6.3 Multi-band Wireless System

Figure 2.5 is an example of MEMS switch application in an integrated multi-band wireless transceiver. As MEMS switches offer the high isolation, a SPDT switch is employed to isolate transmitter and receiver paths from each other. In the receive path, RF-MEMS switches are used to select a certain low noise amplifier for the desired frequency band. The image reject filter can be either developed as a RF-MEMS switched bank filter or a RF-MEMS tunable filter. In the transmit path, MEMS switches can select a specific power amplifier and bandpass filter for the band of interest. The frequency of voltage controlled oscillator can also programmed by a bank of RF-MEMS switches [26].
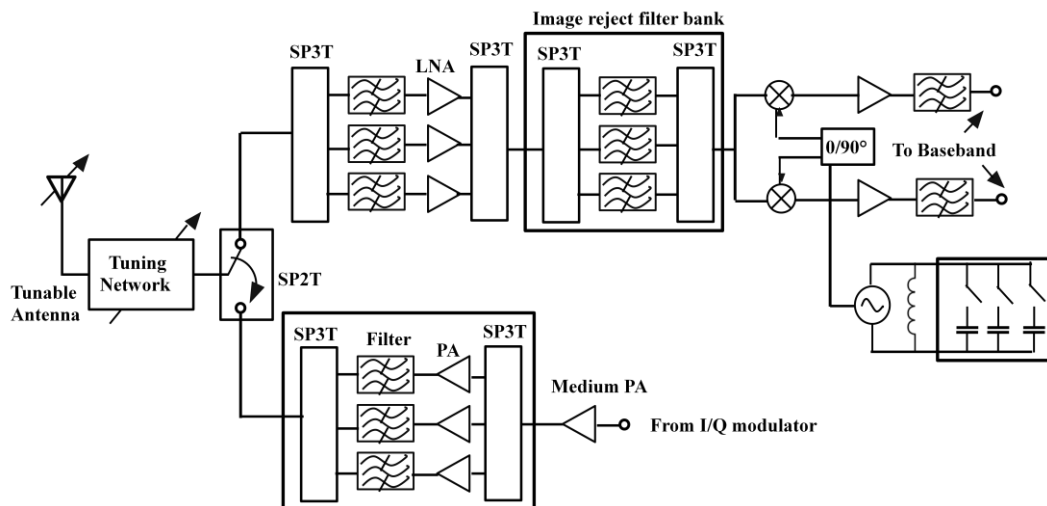
Figure 2.5: Block diagram of a multi-band wireless transceiver showing MEMS switches.

2.6.4 Phased Arrays

RF-MEMS switches are best suited to communication systems, e.g. phased arrays that use a large number of switching devices. The average loss of the state-of-the-art 3-bit MEMS phase shifter shows an improvement of more than 3 dB over comparable GaAs FET devices [9]. This translates to 6 to 8 dB improvement in radar or a two-way telecommunication system. Therefore, one can eliminate a few amplifier stages in T/R chain.

2.6.5 Redundant Millimeter Wave Communication

Figure 2.6 presents a redundant low noise front-end using MEMS technology. The redundant character is assured by a SPDT which addresses the RF signal in the selected amplifier path constituted by filters and LNA [27]. MEMS based SPDT switching circuit exhibits high performances in term of insertion loss and isolation with negligible dc power consumption that cannot be achieved by solid-state devices.
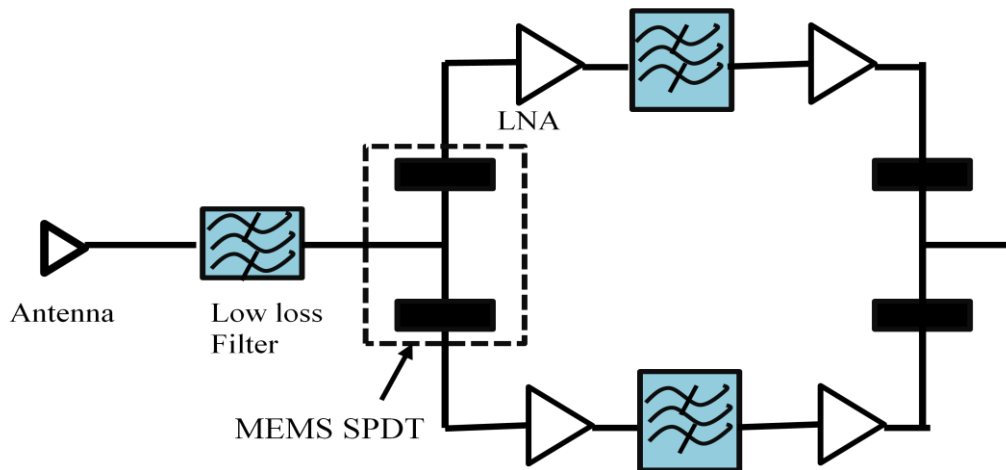
Figure 2.6: MEMS SPDT based redundancy front-end for secured millimeter wave communications.

2.7 Literature Review on Capacitive Shunt Switch

Research on RF-MEMS switch has been strongly pursued by many researchers in universities and industrial research communities. From the first day of MEMS switch finding, till today, lots of MEMS shunt switches have been developed with different designs, parameters, dimensions and materials to achieve better performances. All the switches discussed below are based on the electrostatic actuation as it is compatible with IC technology. The first MEMS switch for microwave applications was developed by Dr. Larry Larson at the Hughes Research Labs (Malibu, California) in 1991 [8]. However, it was far from mature and had poor yield and virtually no reliability. Still, it demonstrated excellent RF performance up to 50 GHz. In 1995, Raytheon (formerly Texas Instrument) developed the first practical capacitive shunt switch [28]. The bridge structure is composed of 0.3 μm of aluminum that is suspended 4 μm above the transmission line. Si_3N_4 with a thickness of 1000 Å was used as a dielectric layer on the

central conductor of the CPW. At 10 GHz, the insertion loss and the isolation of the switch are approximately 0.5 dB and 15 dB respectively. An improved version of the MEMS switch, in term of RF losses, is reported in [19]. The insertion loss is enhanced to 0.14 dB and isolation up to 24 dB at a frequency of 20 GHz. The required actuation voltage is 50 V, with a switching ON time of 6 μs and a switching OFF time of 4 μs. An interesting design variation was introduced in 2001 by Robert Bosch GmbH, Germany. The membrane of their longitudinal capacitive shunt switch is part of the signal line and, when lowered by applying approximately 25 V, is capacitively short circuited by a ground potential connection between the two ground lines of the coplanar waveguide. Design is optimized for 24 GHz ($S21$ (ON) > -0.3 dB, $S21$ (OFF) < -33 dB) [29]. Despite extensive research over the past few years, the commercial market for RF-MEMS switches is still in the pioneering stage. One of the primary hurdles to commercialization is high voltages required to actuate the switches. A typical MEMS switch requires 20 V-80 V for operations. The details of the low actuation voltage based capacitive switches will be subsequently presented in this chapter. The selection criteria for the switches listed below are: novelty at the time they were introduced, RF performance, special design features, fabrication processes or special choice of structural materials.

2.7.1 MEMS Switch with Low Actuation Voltage

A. Low Spring Constant Switches

In 1998, the University of Michigan, Ann Arbor, USA, published on an electrostatically actuated switch with the pull-in voltage of 14-16 V [30]. The idea is to suspend the membrane using meander support structures, which results in low spring constant design. The 2 μm thick, electroplated gold membrane of this switch was embedded between bottom and top electrodes. A constant applied voltage maintains the switch clamped to the top electrode preventing any undesired movement of the switch. At the time of switching, the voltage between top electrode and switch is removed and the necessary pull-in voltage is applied between the ground plane of the CPW line and the switch. Once the switch clamps down, the high capacitance present at the center conductor provides a virtual short at RF. Aluminum was used as sacrificial layer material, and 50 nm of parylene was coated on the metal structure for isolation and anti-stiction

purpose. The RF performance of the switch was quite good (ON-state: $S21$= - 0.2 dB at 20 GHz, OFF-state: $S21$ < - 40 dB for frequencies up to 40 GHz). In 2003, a novel low spring constant switch was developed by the Peroulis *et al.* [31]. In this switch, the inductance of the signal path in the down-state is determined by the special geometry of the beams supporting the membrane, providing improved isolation because of resonance behavior in the target frequency range. Around 80 % reduction in the actuation voltage was obtained by increasing the number of meanders in a serpentine folded configuration of the mechanical spring from 1 to 5. The ideal actuation voltage and spring constant of the switch for 5 meanders are at 3 V and 0.27 N/m respectively. However, the actuation voltage is 6 V for a spring constant of 1.1 N/m. The difference between the theoretical and the experimental values of the actuation voltage is attributed to an intrinsic axial stress in the nickel armature during fabrication. After this, many MEMS switches were designed using the similar meander structure to lower the spring constant and lower the actuation voltage actuation [23, 32-37]. However, the problems with these kind of switches are their sensitivity to mechanical force such as acceleration, vibration and the slow response time.

B. Bridge Structure Material

Efforts are also made to reduce the mechanical spring constant with the use of different materials. MEMS switch with Al and $Al_{0.96}Si_{0.04}$ alloy are used as the armature material for reducing the pull-in voltage [38]. The switch structure is optimized by calculating actuated voltages which depend on membrane materials and geometrical sizes of Young's modulus. The experimental results showed that the alloy has a lower actuation voltage of 5 V compared to the gold counterpart with an actuation voltage of 45 V. However, the transmission loss of the alloy membrane is twice in comparison to the gold membrane. In 2006, Dai *et al.* used Al as a bridge material. Switch has a pull-in voltage of 7 V, but poor RF response (insertion loss and isolation of the switch are 3.1 dB and 15 dB at 40 GHz) [39]. The study demonstrated an improvement in the actuation voltage at the expense of the RF performance.

C. MEMS Switch with Low Height

As discussed in the above section, meander type anchors can be used to decrease the spring constant, and to reduce the devices vulnerability to shocks and vibration, another

electrode can be fabricated on the top of the suspended membrane. This will increase the cost and complexity of the fabrication process. In view of this the University of Michigan developed, a low height switch with *Ti/Au* membrane, having high spring constant [6]. The switch is based on a 0.8-1.0 μm thick *Ti/Au* membrane, suspended at a height of 1.5-2.2 μm above the transmission line. A low gap height results in a low pull-down voltage of 12-24 Volts while still maintaining a high spring constant for the membrane. The low height switch therefore has a relatively high mechanical resonant frequency and a fast switching time. Also, it is not sensitive to vibrations, but the price is paid in the form of reduction in the capacitance ratio in the range of 20-40 [40, 41].

D. Switch without Mechanical Spring

There are research groups working towards ultra low actuating voltage MEMS. The concept of the switch relies on a mechanically unconstrained armature actuated over a coplanar waveguide using electrostatic forces (kiang et al.) [42]. The minimum actuation voltage of the switch is < 2 V, with an isolation of 40 dB and insertion loss < 0.7 dB at 78 GHz. Springless armatures has also been used for implementing the shunt and series dc contact switches. Shen *et al.* proposed an anchorless armature that is hinged to the substrate by metal posts [43]. Nevertheless, the switch must overcome the friction force when the armature contacts with the metal hinges during the switching. The actuation voltage has reported less than 10 V. Lee *et al.* [44] reported a series contact RF-MEMS switch using a pull-up structure without involving an elastic deformation during the switching operation. The actuation voltage of the switch was 4.5 V and the time required to switch ON is 120 ns while the reverse operation required 130 ns. The insertion loss and the isolation are 0.5 dB and 55 dB respectively at 50 GHz. But, fabricating the pull-up electrode on top of the suspended membrane is a complex fabrication process, which requires extra masks and need of special and costly releasing equipments and techniques.

E. MEMS Switch with See-saw Electrostatic Actuation

Rangra *et al.* suggested another solution to reduce the actuation voltage. The design used a push-pull configuration to drive the electrostatic actuator. The torsion springs and the levers are placed on both sides of the transmission line [9, 16]. With the application of the dc biasing voltage at either the pull or the push electrode, the armature moves towards ('ON' position) or away ('OFF' position) the signal line accordingly. Since

voltages are applied at both ON and OFF states, the switch is more robust to vibration. The simulated actuation voltages have a range of 8-10 V. After this, a number of researchers have used push-pull type of actuation [45-47] but these switches are very bulky due to pull-up actuation electrodes.

F. MEMS Switch with High-k Dielectrics

High-k dielectric materials, such as strontium titanate oxide ($SrTiO_3$), barium strontium titanate (BST), hafnium oxide (HfO_2) and tantalum pentoxide (Ta_2O_5) , have been explored as alternatives to silicon nitride and silicon dioxide for improving the overall switch performance with compact size. Park *et al.* presented very high capacitance ratio MEMS capacitive switches by using a 0.190 μm thick strontium titanate oxide [23, 24]. The dielectric constant of $SrTiO_3$ is 30-120, depending on the deposition temperature with loss tangent less than 0.02. The reported capacitance ratio of fabricated device is 600 with a down-state capacitance of 60 pF. The gold or copper switch membrane was electroplated on top of a polyimide or photoresist sacrificial layer. The membrane is suspended through the low spring constant springs, resulting in actuation voltages of 8-15 V. The overall RF performance of the switch was very impressive ($S21$ (ON) = - 0.08 dB at 10 GHz, $S21$ (OFF) = - 42 dB at 5 GHz). Barium Strontium Titanate is used in [48] as a dielectric material of the proposed metal-insulator-metal (MIM) switch. The utilization of barium strontium titanate improves the RF performance in comparison to the silicon nitride. An initial gap of 1.85 μm yielded a capacitive ratio of more than 4500, with an actuation voltage of 18 V. Reducing the gap to 0.85 μm, the capacitive ratio is still more than 2000 and the actuation voltage is 7 V. These ratios could only be achieved if the initial gap is more than 44 μm when silicon nitride is used as a dielectric layer. Zhang *et al.* [21] reports a high RF performance π-type RF capacitive switch, using hafnium oxide as the dielectric layer in the MIM structure. The simulation shows that thinner layers of the dielectric produce a better isolation at RF frequencies of less than 20 GHz. The dielectric constant of the material is 17 and could produce a capacitive ratio of 540. The experimental insertion loss and the isolation at a RF frequency of 50 GHz are better than 0.8 dB and 30 dB respectively. The paper also describes some fabrication and reliability issues using the hafnium oxide. This material exhibits an increase in leakage current after the introduction of an annealing step, which has a negative impact on the quality of hafnium oxide. This effect can be attributed to the change in the crystalline

structure after a high temperature treatment. Without the annealing process, the dielectric material had a leakage current with ranges of 10^{-6}Acm^{-2} to 10^{-7}Acm^{-2} at 15 V. The material is able to withstand greater than 10^7 cycles of voltage changes without degradation. The most recent work that used different material for dielectric layer was developed by Persano *et al.* [49, 50]. They used tantalum nitride (*TaN*) and tantalum pentoxide as the dielectric layers for the switches. Switches showed actuation voltages of 15–20 V, an insertion loss > 0.8 dB up to 30 GHz, and an isolation of 40 dB at 25 GHz. As discussed in the above cited section, High-*k* dielectrics can be a good candidate material for capacitive MEMS switches, but with few related experimental studies related to the reliability issues. Their physical and chemical properties need to be studied thoroughly such as in case of SiO_2. For a large number of high-*k* materials, the band gap is inversely proportional to *k*. To reduce leakage current tunneling, while maintaining the same gate capacitance, the material should have a large band gap and barrier height between the electrode and the conduction band of the dielectric. In addition, many of high-*k* dielectric materials are thermodynamically unstable on silicon or lack in other desirable properties such as high dielectric breakdown voltage, resistance to dielectric charging, low defect density, good adhesion, thermal stability, low deposition temperature, low surface roughness at the interface and the ability to generate patterns [51-53].

2.8 Conclusion

RF-MEMS switches with negligible dc power consumption and excellent RF performance can replace the state-of-art semiconductor switches in various telecommunication applications. However, there are quite a few challenges associated with RF-MEMS switches such high pull-in voltage and low switching speed. Various approaches have been discussed in the literature to reduce the pull-in voltage. In this work, low height and cantilever structures based switches have been designed for reducing the pull-in voltage as detailed in the chapters 3 and 4.

Chapter - 3
Design Aspects of RF-MEMS Switches

3.1 Introduction

This chapter is divided mainly into two sections i.e. electromechanical and electromagnetic design aspects of the MEMS switches. Under electromechanical design, spring constant, pull-in voltage and dynamic response (pull-in and release time) dependency on the switch material has been explored. In electromagnetic design, RF behavior of a capacitive device has been studied through the electrical equivalent model of the switch. The dependence of the S-parameters on the air gap between bridge and transmission line, and central overlap area has also been investigated. This chapter also presents improved designs for enhancing the performance of the capacitive switch as compared to the conventional approach based switch.

3.2 Electromechanical Design

This section deals with the electromechanical design of electrostatically actuated MEMS switches. RF-MEMS switches are based on the beams either fixed at one end (cantilever) or both ends (bridge). The electrostatic actuation is used to deflect the structure in the direction perpendicular to the beam plane. The section is started with the general approach and the expressions for the spring constant of the simple structures used to implement the MEMS switches. Later, electrostatic actuation, pull-in voltage and dynamic response analysis has also been discussed. The major part of this section is devoted to the analysis of a non uniform bridge structure, commonly used for MEMS switches. This structure has been used for implementing the metal-to-metal contact switch as discussed in the chapter 4.

3.2.1 Spring Constant for the Structures Specific to RF-MEMS Switches

Fig. 3.1 shows various structures like, cantilever with free end and guided end, and fixed-fixed type beams. A concentrated load F (N) is applied to the free end, guided end and to the center of the fixed-fixed beam in Fig. 3.1 (a-c), whereas a uniform distributed load f (N/m) has been applied to the surface of each beam in Fig. 3.1 (d-f). If the operation of the structure is limited to small deflections (0.2-0.5 % of the beam length) as

is the case of RF-MEMS devices, the mechanical behavior can be modeled using a linear spring constant, k (N/m) [54, 55] and can obtained using the relation, $F_z = k_z z$, $F_y = k_y y$, $F_x = k_x x$. The displacement table is summarized in the Table 3.1. The cantilever beam is less stiff as compared to the fixed-fixed beam if the dimensions are equal for the both cases.
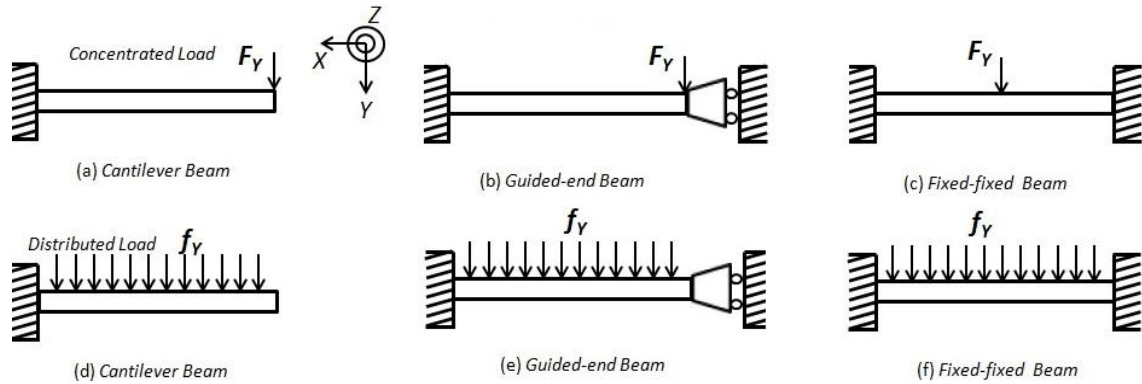
Figure 3.1: Various structures with concentrated load (F) or distributed load (f). In all cases only the y-component of force is shown.

Table 3.1 Displacement equations derived from small displacement theory (a) Concentrated load (b) Uniformly distributed load [54].

(a)

Cantilever	Guided End Cantilever	Fixed-Fixed Beam
$x = \dfrac{F_x L}{Ewt}$ $y = \dfrac{4F_y L^3}{Ew^3 t}$ $z = \dfrac{4F_z L^3}{Ewt^3}$	$x = \dfrac{F_x L}{Ewt}$ $y = \dfrac{F_y L^3}{Ew^3 t}$ $z = \dfrac{F_z L^3}{Ewt^3}$	$x = \dfrac{F_x L}{Ewt}$ $y = \dfrac{F_y L^3}{16Ew^3 t}$ $z = \dfrac{F_z L^3}{16Ewt^3}$

(b)

Cantilever	Guided End Cantilever	Fixed-Fixed Beam
$x = \dfrac{f_x L}{E}$ $y = \dfrac{3f_y L^3}{2Ew^3 t}$ $z = \dfrac{3f_z L^4}{2Ewt^3}$	$x = \dfrac{f_x L}{Ewt}$ $y = \dfrac{f_y L^4}{2Ew^3 t}$ $z = \dfrac{f_z L^4}{2Ewt^3}$	$x = \dfrac{f_x L}{4E}$ $y = \dfrac{f_y L^4}{32Ew^3 t}$ $z = \dfrac{f_z L^4}{32Ewt^3}$

3.2.2 Electrostatic Actuation and Pull-in Voltage

This section details the electromechanical model and closed form expression for the parallel plate capacitor. Electrostatic actuation is produced by the electrostatic force which exists on the plates of a capacitor under an applied voltage. Although actual capacitance is more due to the fringing field, still this model provides a good understanding of the electrostatic actuation.
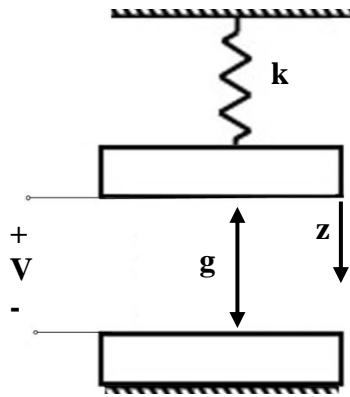
Figure 3.2: Spring and parallel plate capacitor.

The capacitance of a fixed parallel plate capacitor is given by the relation $C = \varepsilon_o \frac{A}{g}$. For a variable parallel plate capacitor, the movable plate moves normally to the fixed plate as defined by the coordinate, z (Figure 3.2). The capacitance of the movable capacitor can be calculated as follows:

$$C = \varepsilon_o \frac{A}{(g-z)}$$

(3.1)

The energy stored, W, in a capacitor with a voltage, V, between the plates is given by equation (3.2).

$$W = 0.5\varepsilon_o \frac{A}{(g-z)} V^2$$

(3.2)

The electrostatic force between the plates can be determined by differentiating the energy function with respect to the coordinate in the direction of the force.

$$\frac{dW}{dz} = F = 0.5\varepsilon_o \frac{A}{(g-z)^2} V^2$$

(3.3)

If the movable parallel plate is attached to a spring, k, then under equilibrium condition

$$kz = 0.5\varepsilon_o \frac{A}{(g-z)^2} V^2$$

(3.4)

$$V = \sqrt{\frac{2kz(g-z)^2}{\varepsilon_0 A}}$$

(3.5)

When voltage is increased, the force is increased due to an increase in the charge; simultaneously the increased force decreases the beam height, which, in turn, increases the capacitance and thus the charge and the electric field. At some voltage (pull-in voltage) the increase in the electrostatic force is greater than the increase in the restoring force, resulting in the beam position becoming unstable and collapse of the beam to the down-state position. By taking the derivative of equation (3.5) with respect to the beam height and setting that to zero, the height at which the instability occurs is found to be exactly two-thirds of the zero-bias beam height. Substituting this value back into the equation (3.5), the ''pull-in'' voltage is given by the equation (3.6) [6]:

$$V_p = V(\frac{2g}{3}) = \sqrt{\frac{8kg^3}{27\varepsilon_0 A}}$$

(3.6)

3.2.3 Dynamic Response

Pull-in voltage expression derived in the previous section describes the static response of the switch. For dynamic response (switching time), Fig. 3.2 should be modified by inclusion of finite mass and mechanical damping force that arise from the viscosity of the air between the plates of the actuator. The resulting one dimensional model is given in Fig. 3.3.

A. Switching Time

Switching time can be modeled using the force balance equations involving mass, spring and damper equivalent model of parallel plate capacitor e.g.

$$m\frac{d^2z}{dt^2} + ky + b\frac{dz}{dt} = \frac{0.5\varepsilon_o A V^2}{(g-z)^2}$$

(3.7)

where m is the mass of the movable plate and b is the damping coefficient which is given by:

$$b = \frac{3}{2\pi} \frac{\mu}{g^3} A^2 \qquad (3.8)$$

where μ the is coefficient of viscosity. Non-linearity in the actuation dynamics makes it necessary to use non-linear solver for calculating the switching time [6, 56]. Therefore closed form expressions are needed for design intuition.
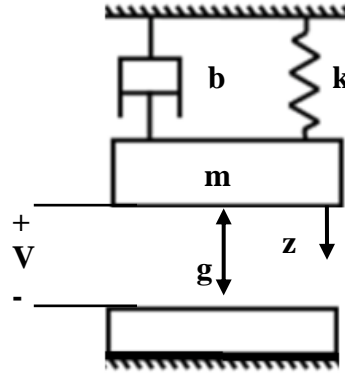
Figure 3.3: Mechanical equivalent of actuator.

A.1. Pull-in Time

It is defined as the time taken by a movable structure to make contact with the underlying plate. A closed form expression for the pull-in time can be obtained for the acceleration limited system ($b = 0$) by assuming the electrostatic force to be constant and equal to the initial applied value [57]. Under the above approximations, the equation of motion becomes:

$$m\frac{d^2 z}{dt^2} + kz = \frac{0.5\varepsilon_o A V^2}{(g)^2} \qquad (3.9)$$

The pull-in time is calculated for $z = g$ and is given by:

$$\text{Pull\_in time } (t_p) = \frac{3.67 V_p}{\omega_o V} \qquad (3.10)$$

where ω_o is the mechanical angular resonant frequency of the movable structure.

A.2. Release Time

The time taken by a movable structure (acceleration limited system) to regain its original position when applied voltage is zero and can be calculated as follows [57]:

$$\frac{md^2z}{dt^2} = kg - kz \tag{3.11}$$

$$\frac{dz}{dt} = \sqrt{\frac{k(g^2 - z^2)}{m}} \tag{3.12}$$

$$\text{Release time } (t_r) = \frac{\pi}{2\omega_o} \tag{3.13}$$

3.2.4 Case Study of a Common Structure Used for RF-MEMS Switches

In this section, we discuss about the electromechanical behavior for one of the common RF-MEMS switch structure. The structure has four flexures attached to a central plate as shown in the Fig. 3.4. Two metal stoppers on either side of the central plate have been used to avoid the short circuit in the actuated state. Stoppers are laying 2 μm below the bridge structure. The actuation electrode is placed 3 μm below the central plate of the bridge structure and has actuation area of 110×80 μm². As electrostatic actuation is used, non-linearity in the actuation dynamics makes it necessary to use non-linear solver for calculating the switching time. Therefore, closed form expressions are needed for design intuition. In literature, a number of studies have been reported for analyzing the switching time behavior of an electrostatic actuator [15, 56, 58, 59]. The closed form expression for the pull-in time given in [6, 56] doesn't incorporate the gap dependency of electrostatic force and hence is inaccurate. Thus, the main emphasis of this section is to derive the improved analytical expression for the pull-in time which takes the above discrepancy into account for its derivation. The pull-in time expression has also been derived for the case when the beam is stopped at 2 μm distance before it touches the actuator. Further, pull-in time dependency on perforations in movable structure, the ratio of the applied voltage to the pull-in voltage, materials with Young moduli, E (70-200 GPa) and density, ρ (2.7-19.3 g/cm³) have also been explored. The results obtained using closed form expressions has been compared to the standard 3-D FEM simulator and with Ref. [56]. The derived expressions can be used as guidelines for RF-MEMS switch design.

A. Spring Constant

In mechanical design, important parameter is the spring constant 'k' of the structure. The beam is modeled as cantilever with four guided ends. The spring constant for a guided end cantilever is given by the equation (3.14) [60]:

$$k = \frac{EWt^3}{L^3} \qquad (3.14)$$
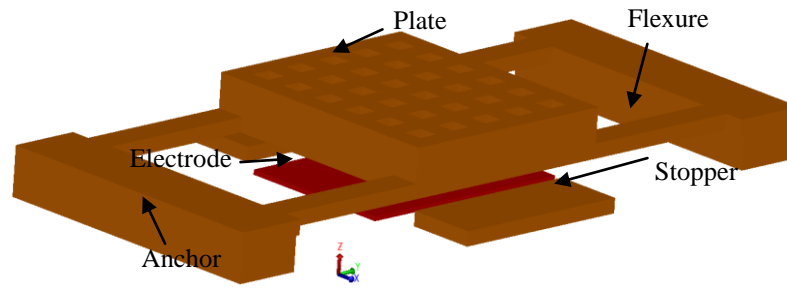
Figure 3.4: 3-D view of the electrostatic actuator.

where E (70, 80, 130, 200 GPa) is the Young's modulus of the *Al, Au, Cu*, and Ni beam respectively, W (15 μm) is the width of flexure, t (1.5 μm) is the thickness of flexure, L (80 μm) is the length of flexure. The equivalent spring constant of the structure with four such guided cantilevers is $K = 4E\ Wt^3/L^3$. The calculated value of the spring constant is 27.69, 31.64, 51.42, 79.10 N/m for *Al, Au, Cu*, and *Ni* beam respectively.

B. Pull-in Voltage

Figure 3.5 shows the simulated value of the pull-in voltage for the perforated and imperforated bridge. Among the four metals, *Ni* has the high simulated pull-in voltage of 91.56 V, while *Al* has low pull-in voltage of 55.31 V. The simulated results are in close agreement with the values calculated from the equation (3.6) as shown in Table 3.2. Further, Fig. 3.5 shows that perforated structure has higher pull-in voltage as compared to imperforated as active overlap area is decreased.

Table 3.2: Comparison of the simulated and calculated voltage for various bridge materials with imperforated bridge.

Bridge Material	Pull-in Voltage (V) Simulated	Pull-in Voltage (V) Calculated
Al	55.31	52.89
Au	60.30	56.53
Cu	75.30	72.07
Ni	91.56	89.39

C. Analytical modeling for Pull-in Time

In case of acceleration limited systems, if we incorporate the gap dependency of the electrostatic force, equation (3.9) can be modified as follows:

(a)   **(b)**
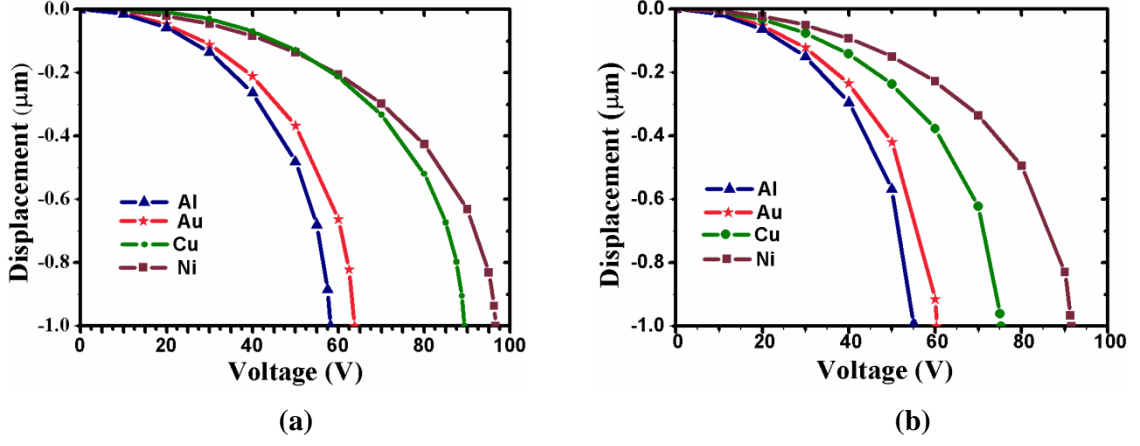
Figure 3.5: Pull-in voltage analysis (voltage applied at the actuation pad vs. displacement of the bridge) with different bridge materials (a) Perforated bridge (b) Imperforated bridge

$$m.\left(\frac{dz}{dt}\right)^2 + kz = \frac{0.5\varepsilon_o AV^2}{(g-z)^2} \tag{3.15}$$

$$\frac{dz}{dt} = \sqrt{\frac{A\varepsilon_o V^2 z}{m\,g\,(g-z)} - \frac{kz^2}{m}} \tag{3.16}$$

$$t_p = \sqrt{\frac{m\,g}{\varepsilon_o A\,V^2}} \int_0^g \sqrt{\frac{(g-z)}{z\left(1 - \frac{k\,z\,g(g-z)}{\varepsilon_o AV^2}\right)}}\, dz \tag{3.17}$$

$$t_p = \sqrt{\frac{m\,g}{\varepsilon_o AV^2}} \int_0^g \sqrt{\frac{(g-z)}{z}}\left[1 - \frac{k\,z\,g(g-z)}{\varepsilon_o V^2}\right]^{-\frac{1}{2}} dz \tag{3.18}$$

As above equation doesn't have closed form solution using Taylor series expansion, the integrand can be simplified as:

$$t_p = \left[2.88\frac{V_p}{\omega_0 V} + 0.608\frac{V_p^3}{\omega_0 V^3} + 0.29\frac{V_p^5}{\omega_0 V^5} + 0.17\frac{V_p^7}{\omega_0 V^7} + 0.11\frac{V_p^9}{\omega_0 V^9} \cdots \right.$$
$$\left. + 0.07\frac{V_p^{11}}{\omega_0 V^{11}}\right] \tag{3.19}$$

The above equation is applicable when a beam makes contact with the lower electrode. In the present case, since the beam is stopped at a distance of 2 μm, the expression can be modified as follows:

$$t_p = \sqrt{m}\,\frac{10^{-11}}{V\sqrt{\varepsilon_o A}}\left[740 + \frac{152.66V_p^2}{V^2} + \frac{73.04V_p^4}{V^4} + \frac{43.38V_p^6}{V^6} + \frac{28.36V_p^8}{V^8} \cdots \right.$$
$$\left. + \frac{19.54V_p^{10}}{V^{10}}\right] \tag{3.20}$$

As shown in Figs. 3.6 and 3.7, beam spends majority of time in travelling the g/3 distance. Increasing the electrostatic force during this phase can decrease the switching time.

Table 3.3: Comparison of pull-in time for perforated bridge.

Bridge Materials	Natural frequency (kHz) (Simulated)	V / V_p (V)	t_p (µs) eq. (3.10)	t_p (µs) eq. (3.20)	t_p(µs) (Simulated)
Au	27.3	1.0	21.41	19.05	19.50
		1.5	14.27	10.19	10.63
		2.0	10.73	7.25	7.60
Al	72.1	1.0	8.10	7.28	7.53
		1.5	5.40	3.86	4.12
		2.0	4.05	2.75	2.90
Cu	50.1	1.0	11.66	10.63	10.84
		1.5	7.77	5.61	5.80
		2.0	5.83	3.98	4.22
Ni	61.0	1.0	9.58	8.77	8.90
		1.5	6.39	4.62	4.80
		2.0	4.79	3.29	3.50
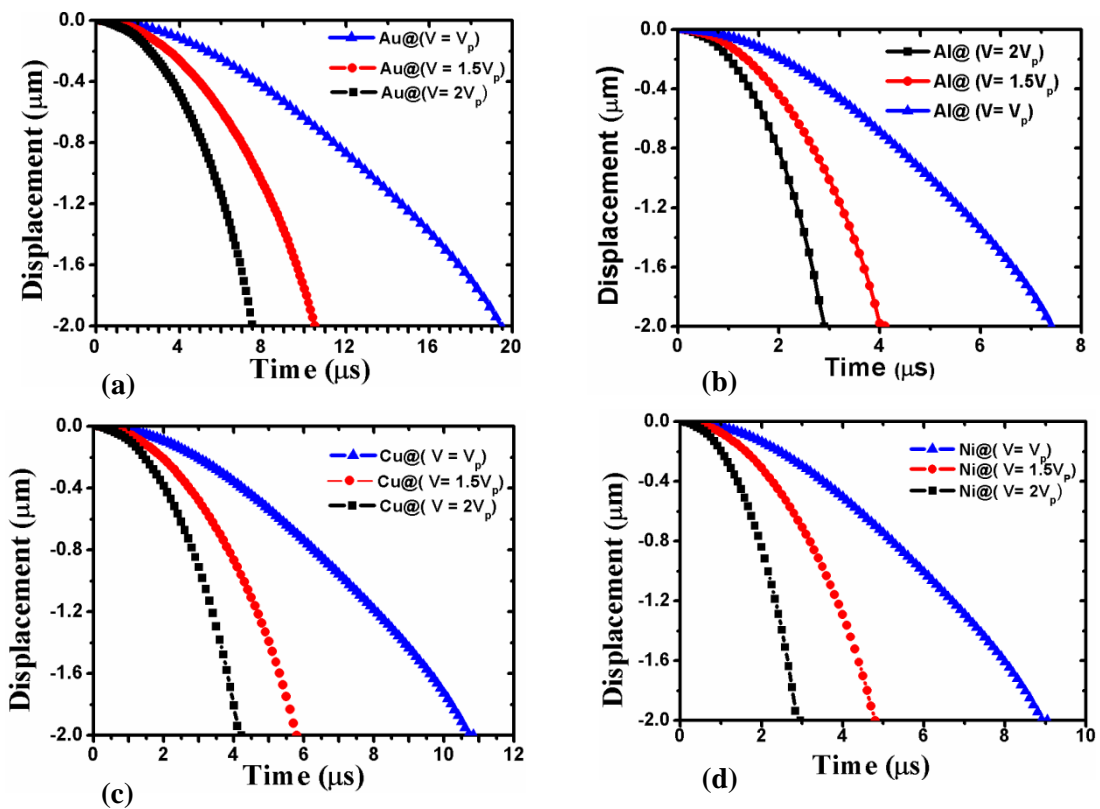
Figure 3.6: Simulated displacement versus time for perforated bridge with (a) *Au*, (b) *Al*, (c) *Cu*, (d) *Ni* at $V = V_p$, 1.5V_p and 2V_p.

This can be done by applying $V/V_p \geq 1$. Secondly, perforations in the beam decrease the switching time because of increase in natural frequency. Further, materials with high E/ρ can also reduce the pull-in time.
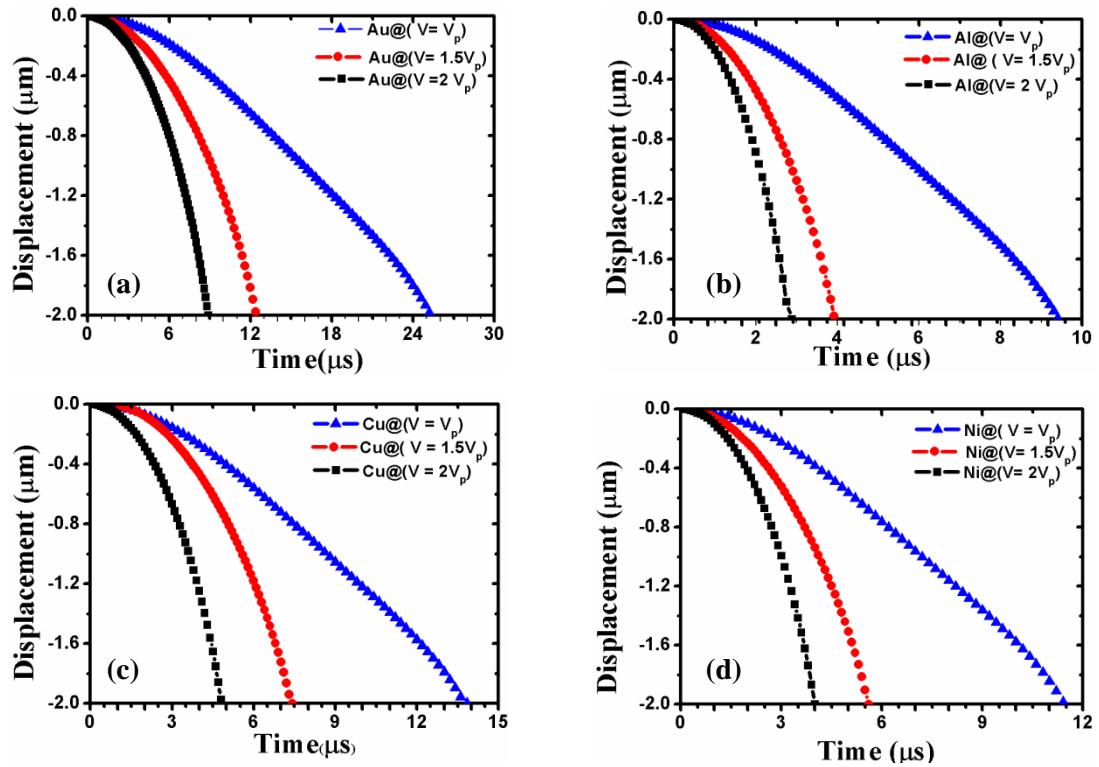
Figure 3.7: Simulated displacement versus time for imperforated bridge with (a) *Au*, (b) *Al*, (c) *Cu*, (d) *Ni* at $V = V_p$, $1.5V_p$ and $2V_p$.

Table 3.4: Comparison of pull-in time for imperforated bridge.

Bridge Materials	Natural Frequency (kHz) (Simulated)	V/V_p (V)	$t_{\text{pull-in}}$ (μs) eq. (3.10)	$t_{\text{pull-in}}$ (μs) eq. (3.20)	$t_{\text{pull-in}}$ (μs) (Simulated)
Au	25.3	1.0	23.09	23.47	25.30
		1.5	15.39	12.24	12.50
		2.0	11.55	8.75	8.90
Al	66.7	1.0	8.76	8.80	9.40
		1.5	5.84	4.61	4.70
		2.0	4.38	3.28	3.40
Cu	46.4	1.0	12.59	12.73	13.80
		1.5	8.39	6.64	7.40
		2.0	6.30	4.72	4.80
Ni	56.5	1.0	10.34	10.49	10.40
		1.5	6.89	5.47	5.60
		2.0	5.17	3.89	4.00

D. Release Time

Table 3.5 verifies the inverse relationship between t_r and f_o as shown in the equation (3.13). Further, it can be observed from the Tables (3.4) and (3.5) that pull-in time is more than the release time because of non-linear behavior of beam displacement while being actuated by electrostatic force. In case of release time, spring restoring force varies linearly w.r.t to displacement and starts from its maximum value so more momentum is available during release phase. The condition for two times to be equal can be derived from equations (3.10) and (3.13) i.e.

$$V \approx 2V_p \tag{3.21}$$

Table 3.5 Comparison of the Release time (a) Imperforated bridge (b) Perforated bridge.

(a) Release time for imperforated bridge			(b) Release time for perforated bridge		
Bridge Material	Natural Frequency (kHz)	$t_{release}$ (μs) (3.13)	Bridge Material	Natural Frequency (kHz)	$t_{release}$ (μs) (3.13)
Au	25.3	9.88	Au	27.3	9.15
Al	66.7	3.75	Al	72.1	3.47
Cu	46.4	5.39	Cu	50.1	4.99
Ni	56.5	4.42	Ni	61.0	4.10

Improved closed form expressions for pull-in and release time have been presented for an electrostatically actuated RF-MEMS switch. The results obtained from new expressions differ only by 5 % compared to that obtained using 3-D FEM simulator. It is observed that $V/V_p > 1$, perforation in the hanging structure and material with high value of E/ρ provides high switching speed.

3.3 Electromagnetic Design

In this section, we present the electromagnetic design of the RF-MEMS capacitive switch. The device is represented by a lumped $R, L, C,$ model together with parts of the CPW (coplanar waveguide) transmission line [40, 61, 62]. The lumped electrical model is required to study the RF behavior and building the physical insight of the device. Switch resistance, inductance, and capacitance values are extracted using S-parameters from simulated results, and compared with the numerically calculated values. All the designs are based on a 50 Ω coplanar waveguide a commonly used connector for RF-

MEMS switches. The following section describes the design aspects of the coplanar waveguide.

3.3.1 Coplanar Waveguide

Microstrip and CPW are the two commonly used transmission lines for RF-MEMS devices. For RF-MEMS switches, CPW offers many advantages over the microstrip line such as simple fabrication, eliminates the need of via holes, easy shunt as well as series surface mounting of MEMS switches, and less radiation loss. As the ground planes are available on either side of the transmission lines, this also minimizes the crosstalk.
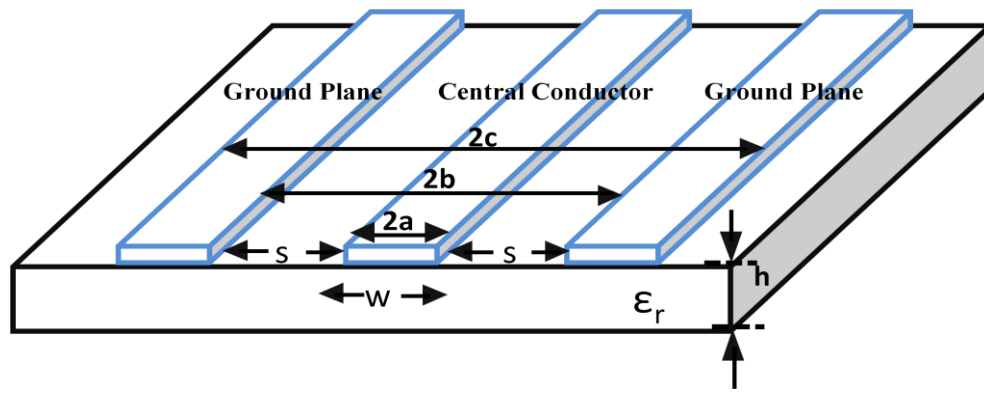
Figure 3.8: 3-D illustration of the CPW.

The first demonstration of the CPW was given by C. P. Wen [63]. The basic structure of CPW is illustrated in Fig. 3.8. A CPW consists of a center conductor line with parallel running ground planes on a dielectric substrate. The characteristic impedance (Z_o) of a coplanar waveguide is given as follows [64]:

$$Z_o = {1}/{C_{cpw}\, v_{ph}} \tag{3.22}$$

$$v_{ph} = {c}/{\sqrt{\varepsilon_{eff}}} \tag{3.23}$$

$$\varepsilon_{eff} = {C_{cpw}}/{C_{air}} \tag{3.24}$$

where C_{cpw} is total capacitance of the transmission line per unit length, C_{air} is the capacitance in absence of the substrate per unit length, v_{ph} is the phase velocity, ε_{eff} is the effective dielectric constant and c is the speed of light in vacuum.

$$C_{air} = \frac{4\varepsilon_o K(k)}{K(k')} \tag{3.25}$$

$$k = \frac{c}{b}\sqrt{\frac{b^2 - a^2}{c^2 - b^2}} \tag{3.26}$$

$$k' = \sqrt{1 - k^2} = \frac{a}{b}\sqrt{\frac{c^2 - b^2}{c^2 - a^2}} \tag{3.27}$$

where, K is complete elliptical integral of first kind, k and k' are variables depending on the geometry of the line.

$$C_{cpw} = \frac{2\varepsilon_o(\varepsilon_r - 1)K(k_1')}{K(k_1)} \tag{3.28}$$

$$k_1 = \frac{sinh\left(\frac{\pi c}{2h}\right)}{sinh\left(\frac{\pi b}{2h}\right)}\sqrt{\frac{sinh^2\left(\frac{\pi b}{2h}\right) - sinh^2\left(\frac{\pi a}{2h}\right)}{sinh^2\left(\frac{\pi c}{2h}\right) - sinh^2\left(\frac{\pi a}{2h}\right)}} \tag{3.29}$$

$$k_1' = \sqrt{1 - k_1^2} = \frac{sinh\left(\frac{\pi a}{2h}\right)}{sinh\left(\frac{\pi b}{2h}\right)}\sqrt{\frac{sinh^2\left(\frac{\pi c}{2h}\right) - sinh^2\left(\frac{\pi b}{2h}\right)}{sinh^2\left(\frac{\pi c}{2h}\right) - sinh^2\left(\frac{\pi a}{2h}\right)}} \tag{3.30}$$

Substituting equations (3.25) and (3.28) in (3.24)

$$\varepsilon_{eff} = 1 + \frac{0.5(\varepsilon_r - 1)K(k)K(k_1')}{K(k')K(k_1)} \tag{3.31}$$

Now Substituting equations (3.23) and (3.28) in (3.22)

$$Z_o = \frac{30\pi}{\sqrt{\varepsilon_{eff}}}\frac{K(k')}{K(k)} \tag{3.32}$$

The general rules for determining the dimensions of the width of the signal line (w) and slot gap width (s) are h (substrate thickness) $> w+2s$ which allows the characteristic impedance to be independent of variation of the substrate thickness and b/c <1/4 to ensure the finite ground effect is negligible. Dimension 's' is then established by the predetermined characteristic impedance of the transmission line, w, and permittivity of the substrate. In this thesis, 50 Ω CPW has been designed by using online CPW

dimension calculator [65] and then accurate dimension is obtained by simulating the CPW in Ansys HFSS^{TM}. A 50 Ω configuration is preferred as it provides minimum losses and maximum power handling. In order to avoid energy dissipation into the substrate, the CPW conductor thickness is kept at four skin depths, thus around 98 % of the current will flow within the layer. The skin depth for gold is 0.68 µm-0.83 µm for X-band (8-12 GHz). The opted CPW has the following specifications: $t = 5$ µm, $w = 90$ µm, $s = 55$ µm, $h = 525$ µm, $\varepsilon_r = 11.9$ (silicon).

3.3.2 Switch Lumped Electrical Model

This section presents the circuit model of a capacitive shunt switch. The well known 'T' model (Figure 3.9) [40, 61, 62] describes the RF behavior of a capacitive shunt switch. The capacitive switch is placed in the shunt configuration between the transmission line and ground. The metallic bridge is represented by lumped R_s, L_s, C, elements.

(a)   (b)
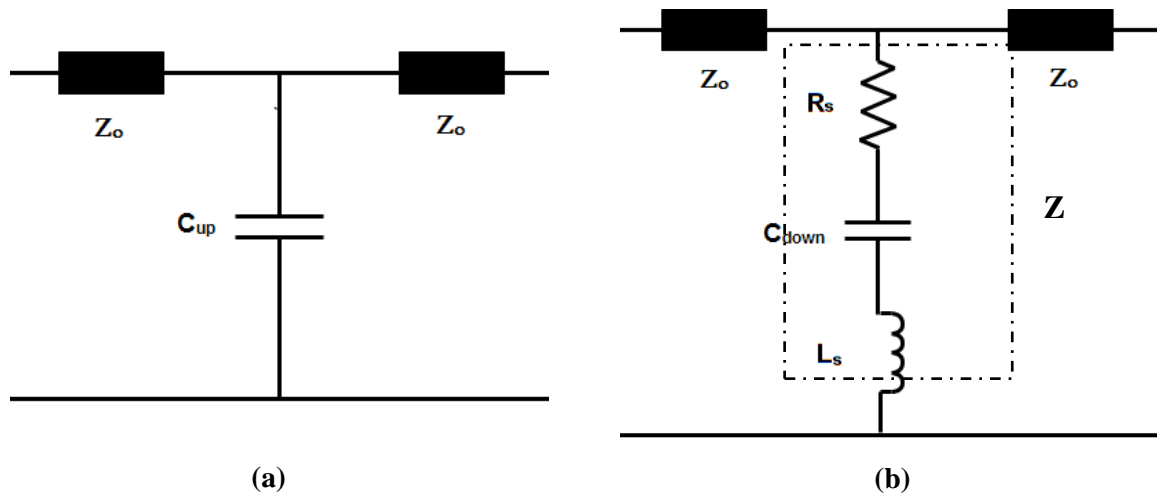
Figure 3.9: Electrical equivalent model of the shunt capacitive switch (a) Up-state (b) Down-state.

The dependence of R_s, L_s and C on the bridge geometry gives insight into the device RF response and is helpful for the optimization in the desired frequency range. The model is used to extract the switch parameters: capacitance in bridge up and down-state, resistance of the metallic bridge and inductance from the simulated S-parameters. For the beam in the down-state, capacitance is constituted by the bridge-dielectric-transmission line overlap area, while in up-state the air gap between the beam and transmission line area results in a very small capacitance. The finite resistance of the bridge material is represented by R_s. The inductance L_s is mainly dominated by the bridge portion above

the gap between CPW ground and bridge structure. The shunt switch total impedance is given by equation (3.33), where Z_s is the switch impedance [6].

$$Z_s = R_s + j\omega L_s - \frac{j}{\omega C} \tag{3.33}$$

$$f_o = \frac{1}{2\pi\sqrt{L_s C}} \tag{3.34}$$

The *LC* series resonance frequency of the switch is given by equation (3.34) and depending on the frequency range of the application the switch impedance can be approximated as:

$$Z_s = \begin{cases} \dfrac{j}{\omega C} \ for \ f \ll f_o \\ R_s \ for \ f = f_o \\ j\omega L_s \ for \ f \gg f_o \end{cases} \tag{3.35}$$

A. Scattering Parameters

The scattering parameters (S-parameters) determine the electrical performance of the switch. Switch can be modeled as a two port network with shunt connection and is characterized by measured or simulated S-parameters. The S_{11} represents the return loss in both states of the device, whereas S_{12} denotes the insertion loss in the up-state of the beam and isolation in the down position. The S-parameters of the shunt switch are given by equations (3.36) and (3.37) [66]. The specification of insertion and isolation are the important design parameters of the switch.

$$S_{11} = -20 \ log \left| \frac{-Z_o}{2Z_s + Z_o} \right| \tag{3.36}$$

$$S_{12} = -20 \ log \left| \frac{2Z_s}{2Z_s + Z_o} \right| \tag{3.37}$$

3.3.3 Capacitive Shunt Switch

This main focus of this section is to discuss the electromagnetic design aspect of the shunt capacitive device. The switch is designed for *X*-band applications with initial specifications of insertion loss $\leq$ 0.3 dB, isolation $\geq$ 20 dB and pull-in voltage $\leq$ 15 V.

A. Description of Device

In shunt configuration the input and output RF ports are physically connected to each other and therefore normally switch is ON. The switch is implemented on a 50 Ω CPW line. The device is implemented with a bridge structure. A uniform bridge structure requires higher pull-in voltage so four flexures attached to a wider beam have been chosen to reduce the pull-in voltage.
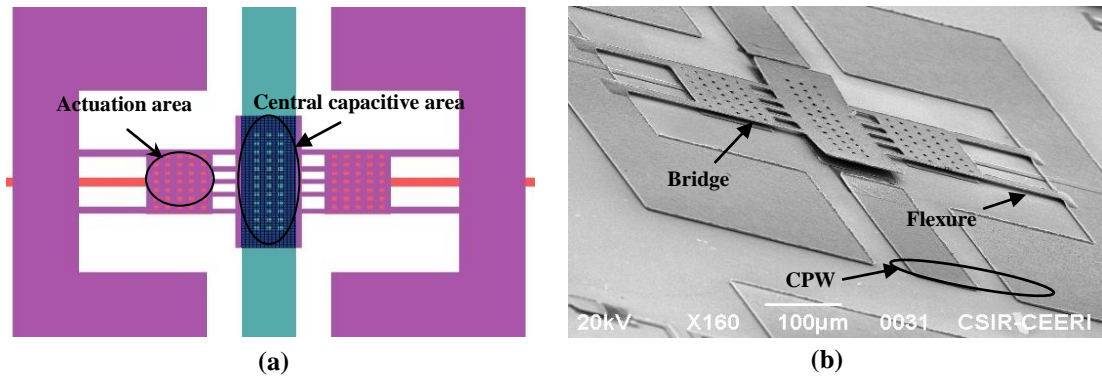
Figure 3.10: (a) Layout of the switch (b) SEM micrograph of the fabricated switch.

In the up-state of the switch there is a gap of 2 μm between switch and central conductor of CPW. The actuation electrodes are kept 0.7 μm down from the transmission line in order to alleviate the stiction problem. Figure 3.10 shows the layout of the switch, whereas Fig.31.0 (b) shows the SEM image of the fabricated device. The dimensions used in designing the device are given in Table 3.6.

B. Working of Switch

The device operates in two states. In the up-state of the bridge, the device is 'ON' as depicted in Fig. 3.11 (a). Switch shows the insertion loss during this state. The electrostatic actuation is used is bring the bridge in the down-state as shown in Fig. 3.11 (b). The device shows isolation characteristics during this state.
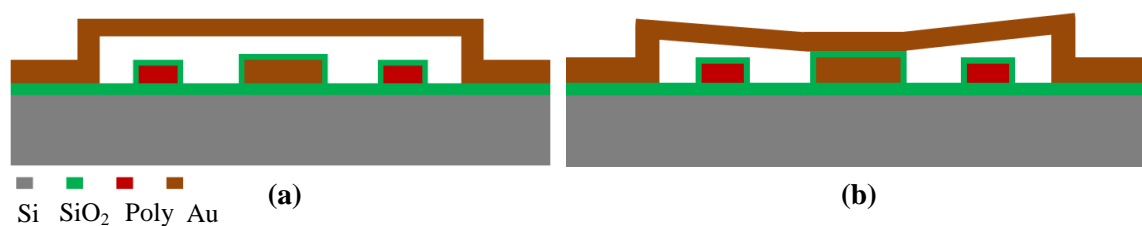
Figure 3.11: Cross-sectional view of the switch during (a) ON-state (b) OFF-state.

Table 3.6: Dimensions of the designed switch.

Dimension	Value
Length of flexures	115 µm
Width of flexures	15 µm
Thickness of flexures	2 µm
Silicon dioxide thickness (t_{ox})	0.1 µm
Electrostatic Gap (d)	2.7µm
Gap between bridge and transmission line (g)	2.0 µm
CPW	55/90/55 µm

C. RF Response

In order to investigate the RF performance of the device a 3-D structure was created and simulated in Ansys HFSS^{TM}. The substrate material used is silicon and a 1.3 µm thick SiO_2 layer is used as a buffer layer. The CPW and hanging structure, i.e. bridge are assumed to be of gold. Further, a thickness of 0.1 µm of SiO_2 has been placed over the central conductor of CPW. The capacitance in the up-state determines ON-state response (return loss and insertion loss) of the switch, whereas capacitance in down-state, resistance of the switch, and inductance of the switch determine the OFF-state response (isolation, return loss) of the switch [61, 62].

C.1. ON-state Response

C.1.1. Up-state Capacitance

In unactuated state, switch capacitance is comprised of the series combination of the capacitance due to air and the dielectric over the signal line. Thus, the total capacitance in up-state is given by:

$$C_{up} = \varepsilon_o \frac{A}{g + \frac{t_d}{\varepsilon_r}}$$

(3.38)

where A is the overlap area, g is the air gap between the dielectric layer and the movable beam, t_d is the dielectric thickness and ε_o is the free space permittivity, ε_r is the relative permittivity of the dielectric material. As typically air gap vary 2-5 μm and dielectric material thickness is of the order of 0.1 μm and relative permittivity lies in the range of 4-20 (SiO_2, Si_3N_4, HfO_2), C_{up} can be approximated by the expression given below:

$$C_{up} \approx \varepsilon_o \frac{A}{g} \tag{3.39}$$

Although, actual capacitance is higher than the value calculated from the equation (3.39). This is due the presence of fringing fields at the movable beam boundaries which give rise to fringing capacitance. The fringing field capacitance is a significant portion of the total capacitance in the up-state. The total capacitance in the unactuated state can be extracted from the equation (3.40) [62].

$$S_{11} = -20 \, log \left| \frac{-j\omega C_{up} Z_o}{2 + j\omega C_{up} Z_o} \right| \tag{3.40}$$
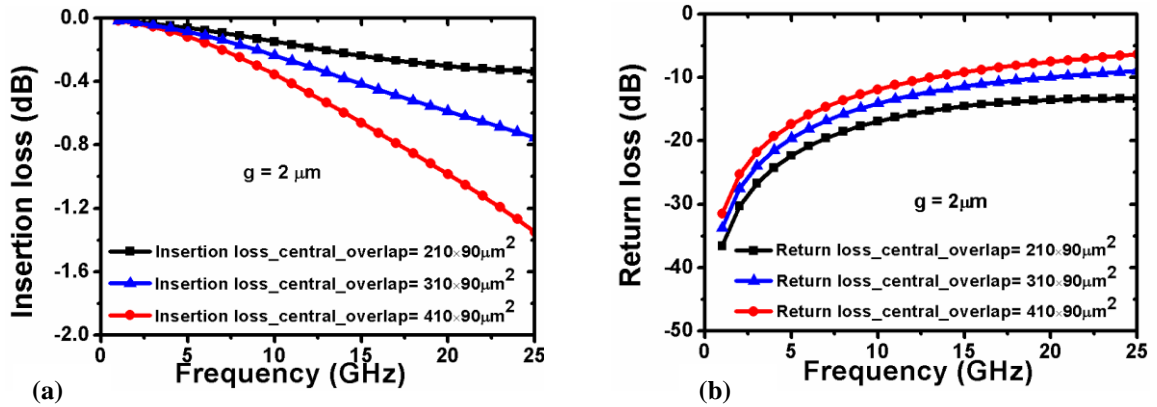
Figure 3.12: ON-state response of the switch with various overlap areas (a) Insertion loss (b) Return loss.

Figures 3.12 (a) and 3.12 (b) show the effect of change in the up-state capacitance on the insertion loss and return loss. Switches with the smaller C_{up} have the less insertion loss (Figure 3.12 (a)). This effect is more visual above the C-band frequencies. Switch with central overlap area of 410×90 μm^2 results in insertion loss of 0.36 dB, whereas with 310×90 μm^2 has 0.24 dB at 10 GHz. The return loss also improves by reducing the up-state capacitance as shown in Fig. 3.12 (b). Table 3.7 summaries the calculated and extracted capacitance in the up-state. Equation (3.40) has been used to extract the total up-state capacitance from the simulated return loss plot. From Fig. 3.13 (b), return loss

corresponding to 1 GHz has been substituted into equation (3.40) for extracting the capacitance in up-state [40, 62]. Table 3.7 shows that extracted up-state capacitance is higher than the calculated value using equation (3.39) as it includes the fringing field capacitance. The frequency at which extraction is performed is chosen such that it is less than the resonance frequency of the switch in the up-state. In the all capacitive devices same process and frequency have been used for extracting the up-state capacitance. The effect of decreasing the initial gap between the transmission line and bridge structure has also been studied. The insertion loss and return loss deteriorate at g = 1 μm as shown in Figs. 3.13 (a) and 3.13 (b) respectively.

Table 3.7: Up-state capacitance with various overlap areas.

Overlap area (μm^2)	$C_{up\_extracted}$ (fF)	$C_{up\_calculated}$ (fF)	$C_{fringing}$ (fF)
210×90	94.58	85.05	9.53
310×90	131.21	125.55	5.66
410×90	170.11	166.05	4.06

(a)   (b)
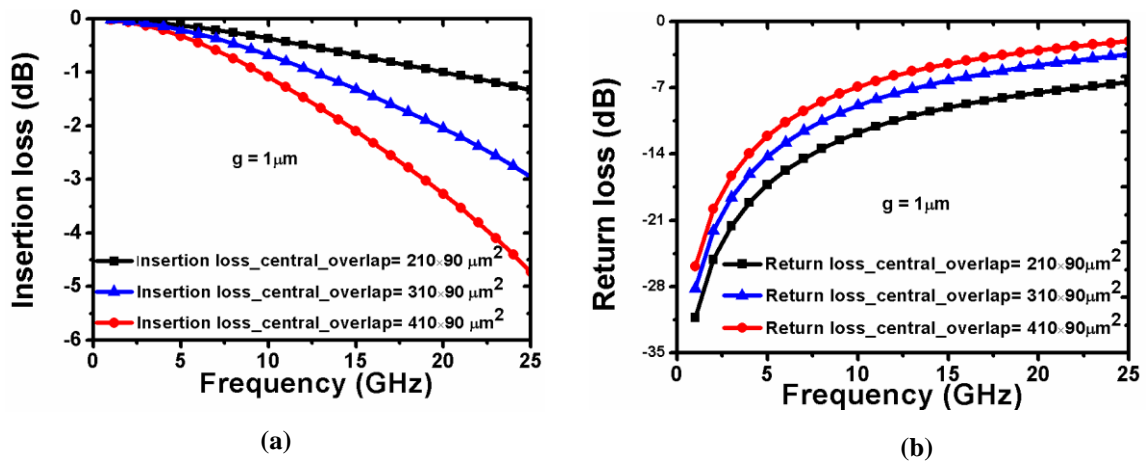
Figure 3.13: ON-state response with various overlap areas and low height (a) Insertion loss (b) Return loss.

The bridge structure has been designed with an array of holes. The holes facilitates in many respects, such as easy removal of the sacrificial layer under the bridge, improves the switching time by reducing the air damping, and also decrease the mass of the suspended structure. The fringing fields cover the holes if the dimensions are less than 3g-4g [40]. In the light of the above consideration and due to the fabrication constraint the hole dimensions are kept at 10 μm×10 μm for all the devices discussed in this thesis. For the capacitive shunt switch, RF response during unactuated state can be improved

either by decreasing the 'A' or increasing the 'g'. Any increment in 'g'' will increase the pull-in voltage. Alternatively, capacitance in the up-state could be reduced by decreasing 'A' value, but this will change the resonant frequency during OFF-state of the device. In section 3.4, we presented the floating capacitor based device to resolve the above issues and for enchaining the device performance.

C.2. OFF-state Response

C.2.1 Down-state Capacitance

In the OFF-state, switch forms a MIM (metal-insulator-metal) capacitor by connecting the bridge to the dielectric layer over the transmission line and can be represented by the equation (3.41) given below

$$C_d = \varepsilon_o \varepsilon_r \frac{A}{t_d} \tag{3.41}$$
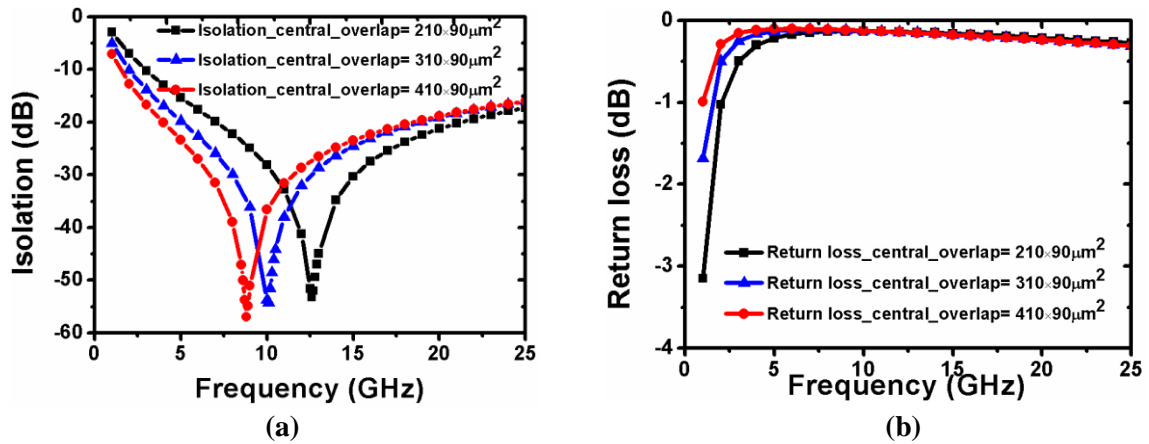
Figure 3.14: OFF-state response of the switch with various overlap areas (a) Isolation (b) Return loss.

The effect of the C_d on the isolation characteristics has been shown in the Fig. 3.14 (a). Switch with larger capacitance shows lower resonant frequency as per equation (3.34). Further, the isolation at the lower frequencies deteriorates with decrease in the down-state capacitance. For example, at 5 GHz with $C_d = 13.28$ pF, isolation is 23.35 dB as compared to the 19.76 dB with $C_d = 10.04$ pF as shown in Fig. 3.14 (a). Return loss during OFF-state for the switch has been shown in Fig. 3.14 (b), and is minimum at the

resonant frequency. The capacitance in the actuated state can be extracted from the equation (3.42) [62] at $f \ll f_o$.

$$S_{12} = -20 \, log \left| \frac{2}{2 + j\omega C_d Z_o} \right| \tag{3.42}$$

The values of C_d are extracted from the simulated isolation characteristics shown in Fig. 3.14 (a). The extracted values agree well with the calculated values as summarized in Table 3.8.

Table 3.8: Down-state capacitance with various overlap areas.

Overlap area (μm^2)	Silicon dioxide thickness (μm)	$C_{d\_extracted}$ (pF)	$C_{d\_calculated}$ (pF)
210×90	0.1	6.24	6.80
310×90	0.1	9.40	10.04
410×90	0.1	12.86	13.28

Based on the RF specifications selected in the starting and achieved through simulated results as shown in the Figs. 3.13 and 3.14, the switch with the central overlap area of $310 \times 90 \ \mu m^2$ has been chosen for *X*-band applications.

C.2.2. Switch Resistance

In Capacitive shunt switch the current passes to the bridge structure from the central conductor of the CPW. Thus, the total resistance of the switch can be expressed as given below

$$R_{ts} = R_{cpw} + R_s \quad \text{and} \quad R_s = \frac{\rho l}{4A} \tag{3.43}$$

where R_{ts} is the total resistance of the switch, R_{cpw} is the resistance due to the CPW line, R_s is the bridge resistance, l is the length of the bridge and A is the area of cross-section and ρ is the resistivity of the bridge material. At high frequency, we have to consider the skin depth phenomenon. If the current is assumed to be uniform to a skin depth or characteristic depth of penetration (δ_s) then the cross-sectional area of the bridge *(A)* is given by:

$$A = 2\delta_s(w_s + t_s) \tag{3.44}$$

Thus, R_s can be modified as

$$R_s = \frac{1}{8} \frac{\rho l}{\delta_s (w_s + t_s)} \tag{3.45}$$

$$\delta_s = \frac{1}{\sqrt{f \pi \mu \sigma}} \tag{3.46}$$

where f is the signal frequency, μ is the permeability of the medium surrounding the conductor, σ is the conductivity of the conductor. The bridge resistance has been extracted using the simulated isolation value corresponding to the resonant frequency. The isolation at the resonance can be expressed from equation (3.47) by putting the R_{ts} in place of Z_s in equation (3.37) [62].

$$S_{12} = -20 \, log \left| \frac{2R_{ts}}{2R_{ts} + Z_o} \right| \tag{3.47}$$

The extracted value of the resistance (0.05 Ω) is coming higher than the value calculated (0.01 Ω) from the equation (3.45) because of the contribution of CPW and bridge.

C.2.3. Bridge Inductance

The bridge structure of the capacitive shunt RF-MEMS switch shows a small inductance in series with the R_s and bridge capacitance as illustrated in the Fig. 3.9 (b). As resonant frequency is the function of the down-state capacitance and inductance (see equation (3.34)), the inductance plays a important role in the OFF-state of the device. This inductance can be calculated from equation (3.34) if the C_d value is known or can be extracted using the simulated isolation value at $f \gg f_o$. The isolation at this frequency can be expressed from equation (3.48) by putting the $j\omega L_s$ in place of Z_s in equation (3.37) [62]. The extracted value of inductance from equation (3.34) is 20.52 pH for the switch with central overlap area of 310×90 μm^2.

$$S_{12} = -20 \, log \left| \frac{2j\omega L_s}{Z_o + 2j\omega L_s} \right| \tag{3.48}$$

C.3. Switch Bandwidth

The switch bandwidth is calculated from the lower and upper operating frequencies with some acceptable maximum insertion loss and minimum isolation values. The lower bound frequency (f_l) is limited by the minimum isolation, whereas upper bound

frequency (f_u) is limited either by maximum insertion or minimum isolation. A broad bandwidth switch with low insertion loss and better isolation thus requires a high capacitance ratio. For bandwidth calculation, initial selected specifications i.e. maximum insertion loss of 0.3 dB and minimum isolation of 20 dB have been considered.
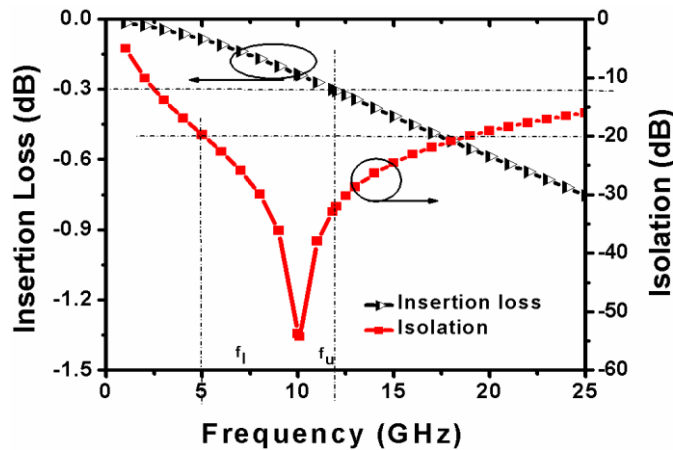
Figure 3.15: Bandwidth of the switch.

It is observed from Fig. 3.15 that device has f_l = 5 GHz and the upper operating frequency f_u (limited by maximum insertion loss) = 11.8 GHz. This results in a bandwidth of 6.8 GHz. As mentioned in the section 3.3.3.C.1.1, an alternate approach has been followed for improving the bandwidth of the device.

C.4. Capacitance Ratio

As concluded in the previous two sections, a low up-state capacitance is desired in the ON-state for good insertion loss and a high down-state capacitance in the OFF-state to achieve better isolation. Thus, the ratio of down-state capacitance to the up-state capacitance expresses the RF response and is one of the figures of merit. A high value is desirable for good RF response.

$$C_{ratio}\left(\frac{C_d}{C_{up}}\right) = \frac{\varepsilon_o\varepsilon_r\frac{A}{t_d}}{\varepsilon_o\frac{A}{g}} = \frac{\varepsilon_r g}{t_d} \tag{3.49}$$

From the equation (3.49) capacitance ratio can be improved either by decreasing the t_d or by increasing the g, ε_r. Decreasing the dielectric (SiO$_2$) thickness below 100 nm is constrained due to the pinhole formation, whereas increasing the initial gap is limited by

the pull-in voltage. The option of high-k dielectric material has been explored in the section 3.5 for to improve the capacitance ratio and thus the RF response. Further, unavoidable surface roughness of the dielectric layer and the bending of the hanging structure due to the residual stress will degrade the down-state capacitance [9]. Figure 3.16 shows the roughness over the dielectric surface. To resolve the above cited issues, all the forthcoming capacitive devices have been implemented by incorporating a floating metal layer over the dielectric.
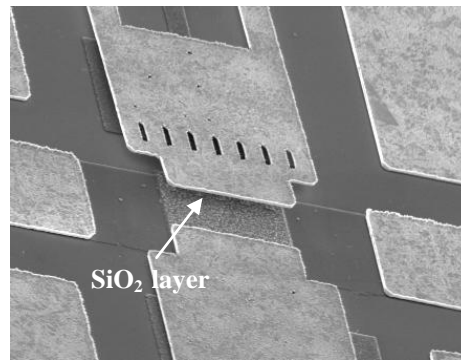
Figure 3.16: Top surface of the SiO_2 showing roughness.

D. Electromechanical Response of the Device

In mechanical response, spring constant of the bridge is determined by doing FEM simulation in Coventorware[(R)]. The hanging structure material is gold with Young's modulus of 80 GPa. An evenly distributed force of 11.88 µN has been applied to the part of the bridge, which is directly above the actuation electrodes and of equal area. This force corresponds to a maximum displacement of 2 µm at the center of the bridge.
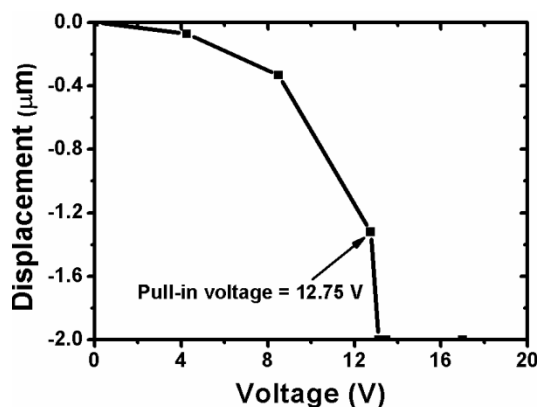
Figure 3.17: Pull-in voltage analysis.
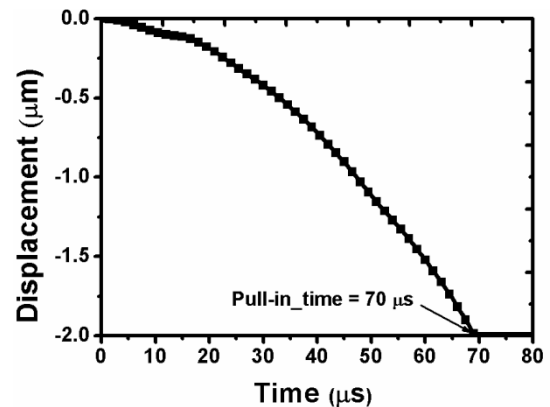
Figure 3.18: Pull-in time response.

The spring constant of 5.94 N/m was extracted from the relation $F_z = k_z z$. Under electromechanical simulation, the coupled electro-mechanics physics with trajectory as an analysis option was used for extracting the pull-in voltage. The actuation voltage is applied through the poly-Si electrodes which are placed 115 μm from the anchor location in the device. The switch has pull-in voltage of 12.75 V as shown in Fig. 3.17. Figure 3.18 shows the simulated pull-in time. The device has a pull-in time of 70 μs.

3.4 Improved Design for Capacitive Shunt Switch

In this section, a shunt capacitive switch has been designed for enhancing the RF and electromechanical performance. Figure 3.19 (a) shows the model of the designed switch. The switch has maximum isolation in the X-band. The device is based on the floating metal concept and has central overlap area of 90×50 μm^2. A SEM image of the fabricated device is shown in the Fig. 3.19 (b).

3.4.1 RF Response

RF response is the function of the ratio of up-state capacitance to the down-state capacitance and a high capacitance ratio is desirable as more down capacitance provides good isolation and less capacitance in up-state provides good insertion loss.
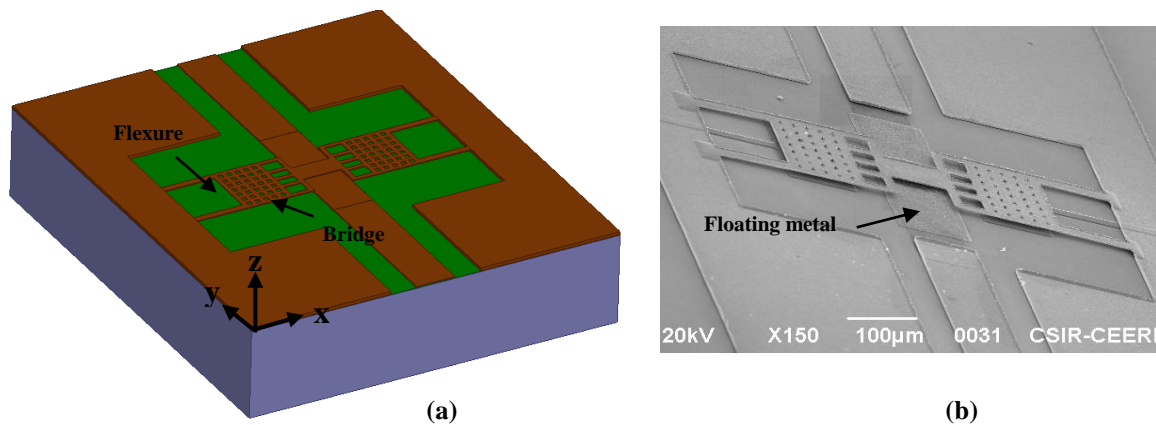
Figure 3.19: (a) Model of the switch (b) SEM micrograph of the fabricated device.

A. ON and OFF-state Response

The capacitance in the up-state of the switch is reduced by utilizing the floating metal layer [20]. The device with floating metal is having $A_{up\_float} = 90 \times 50$ μm^2, whereas conventional $A_{up\_con} = 310 \times 90$ μm^2. Thus, from equation (3.52) capacitance in the up-state of the improved device $(C_{up\_improved})$ is around 6 times less than the capacitance in

the up-state of the conventional switch (C_{up_Con}). The device shows the insertion loss $\approx$ 0.1 dB up to 25 GHz compared to 0.75 dB in case of conventional switch as observed from the Figs. 3.20 (a) and 3.12 (a).

$$C_{up\_improved} = \frac{\varepsilon_o}{g} \times 90 \times 50 \times 10^{-12} \tag{3.50}$$

$$C_{up\_con} = \frac{\varepsilon_o}{g} \times 310 \times 90 \times 10^{-12} \tag{3.51}$$

$$\frac{C_{up\_improved)}}{C_{up_{con}}} \approx \frac{1}{6} \tag{3.52}$$
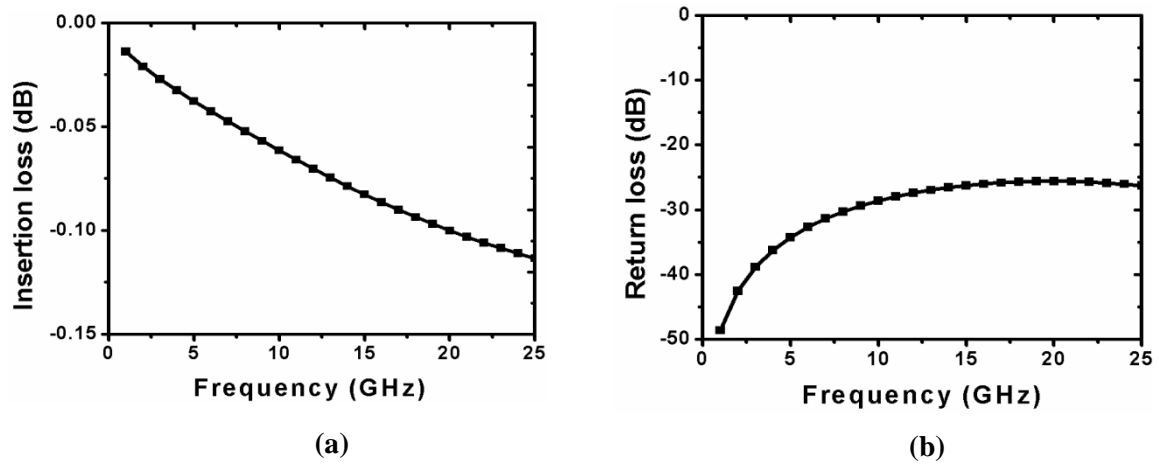
Figure 3.20: ON-state response of the switch (a) Insertion loss (b) Return loss.

Return loss is also improved from 33.73-8.96 dB to 48.65-26.28 dB over the frequency range 1-25 GHz as shown in the Figs. 3.20 (b) and 3.12 (b). Device has C_{up} (calculated) = 20.25 fF, whereas C_{up} (extracted) = 23.53 fF. In the OFF-state both devices have approximately same isolation and return loss characteristics as shown in Fig. 3.21. Switch has C_{down} (calculated) = 10.04 pF, whereas C_{down} (extracted) = 10.38 pF.

B. Bandwidth

For the proposed switch, both the lower bound frequency (f_l) isolation and upper bound frequency (f_u) are limited by minimum isolation. For bandwidth calculation an acceptable maximum insertion loss of 0.1 dB and minimum isolation of 20 dB has been chosen as compared to 0.3 dB in case of the switch based on conventional approach. It is observed from Fig. 3.22 that device has f_l = 4.80 GHz and the upper operating frequency f_u = 21.10 GHz. This results in a bandwidth of 16.30 GHz.
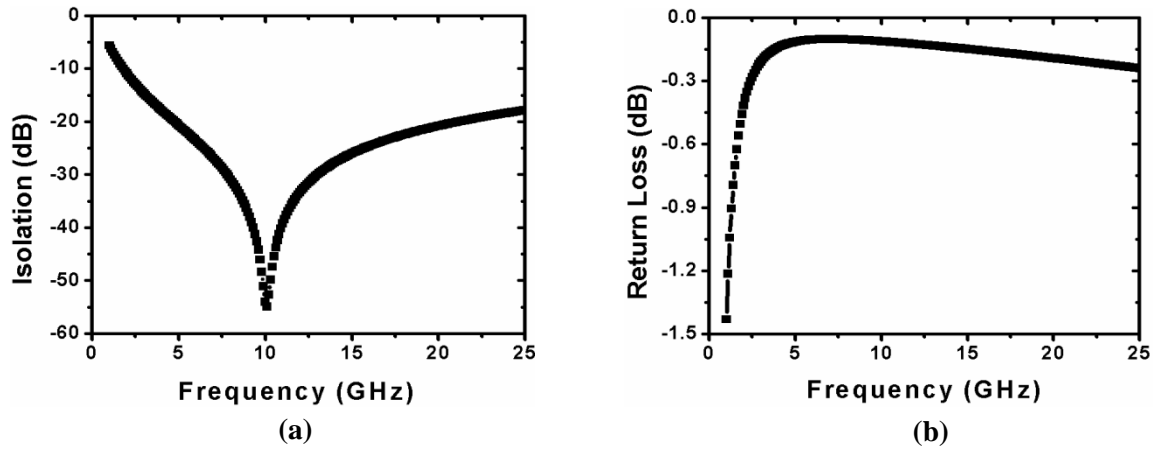
Figure 3.21: OFF-state response of the switch (a) Isolation (b) Return loss.
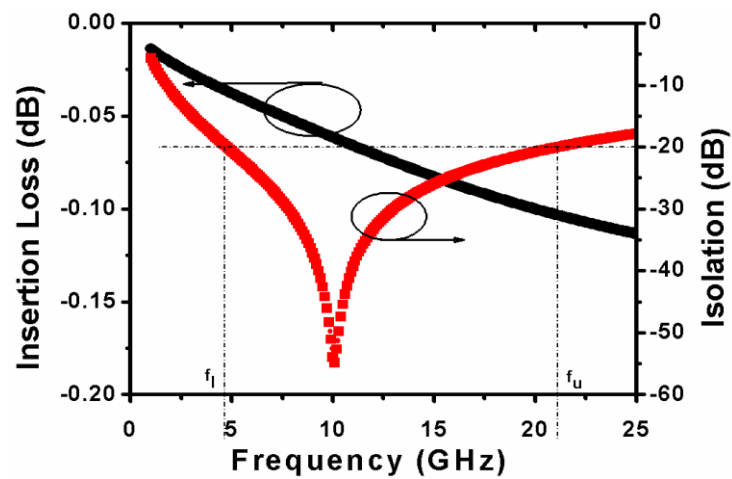
Figure 3.22: Bandwidth of the switch.

C. Self-actuation and Stiction due to RF Power

The shunt capacitive RF-MEMS switch can handle certain power (< 1W) in the on and OFF-state. If the input power is sufficient to provide a voltage higher or equal to pull-in voltage of the device through the central overlap area, then under this condition self-actuation of switch will occur without any dc bias voltage. The input power corresponding to self-actuation can be determined from equations (3.54) and (3.56) as follows [36]:

$$P_{in} = V_{RF}^2 / Z_0 \tag{3.53}$$

$$P_{in} = V_{eq}^2 / Z_0 \tag{3.54}$$

$$P_{S1} (V_{p1cpw}^2 / Z_0) = 2.67 \text{ W} \tag{3.55}$$

$$P_{S2} (V_{p2cpw}^2 / Z_0) = 0.63 \text{ W} \tag{3.56}$$

where P_{in} = input power, P_{S1}, P_{S2} = self-actuation power in float metal and conventional design respectively, Z_0 = 50 Ω, V_{RF} = r.m.s value of the RF signal, V_{eq} = equivalent dc voltage, V_{p1cpw} (Pull-in voltage due to central overlap area in float metal switch) = 11.56 V and V_{p2cpw} (Pull-in voltage due to central overlap area in conventional switch) = 5.6 V. FEM based simulation has been done through Coventorware® to determine the pull-in voltage as shown in Fig. 3.23. It can be seen that the float metal device can handle around four times more input power without self-actuation.
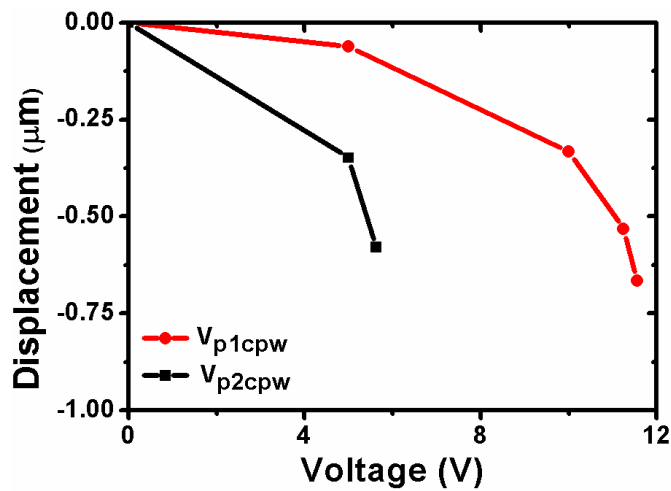
Figure 3.23: Pull-in voltage analysis under central overlap area for both switches.

In down-state, stiction can occur if RF power is sufficient to provide a pull-down force which is higher or equal to the spring restoring force. The power needed to hold the switch in down-state can be obtained from equations (3.57) and (3.58). The hold down power is dependent on frequency unlike the self-actuation power. Thus, lower and higher frequencies have been taken from switches bandwidth for obtaining the hold down power [36].

$$P_{h1} = 27A_{\_a}V_{p1}^{2}t_{ox}^{2} \left[1 + 9.28f^{2}C_{down}^{2} Z_{0}^{2} \right] / 8gA_{RF1} Z_{0} = 10.88 \text{ to } 204.88 \text{ W} \qquad (3.57)$$

$$P_{h2} = 27A_{\_a}V_{p2}^{2}t_{ox}^{2} \left[1 + 9.28f^{2}C_{down}^{2} Z_{0}^{2} \right] / 8gA_{RF2} Z_{0} = 2.06 \text{ to } 10.70 \text{ W} \qquad (3.58)$$

where P_{h1}, P_{h2} = hold down the power for float metal and conventional design respectively, A_{RF} = RF overlap area, $A_{\_a}$ = actuation area (110×150 μm²), and $V_{p1,2}$ (11.75V, 12.75V) pull-in voltage of the float metal switch and conventional switch respectively as shown in Fig. 3.24 (a). For proper functionality of switch input power must be less than the minimum of self-actuation power and hold down power. It is found that input power should be less than 0.63 W for the conventional switch and 2.67 W for

the float metal design. The input power is increased around four times in the float metal device. Another reason for sticition in down-state could be due to the electrostatic force, capillary force, hydrogen bonding, and Van der Waal forces. Float metal switch alleviates this problem as well, due to a reduction in the magnitude of the theses forces [67, 68] caused by central capacitive overlap area compared to the conventional device.

3.4.2 Electromechanical and Dynamic Response

In electromechanical response, pull-in voltage is the parameter of concern. Pull-in voltage is dependent on the spring constant of the bridge material, initial gap between electrode and movable structures and actuation area. Pull-in voltage of 12.75 V and 11.75 V has been obtained through FEM simulation in case of conventional and float metal switch respectively as shown in Fig. 3.24 (a).
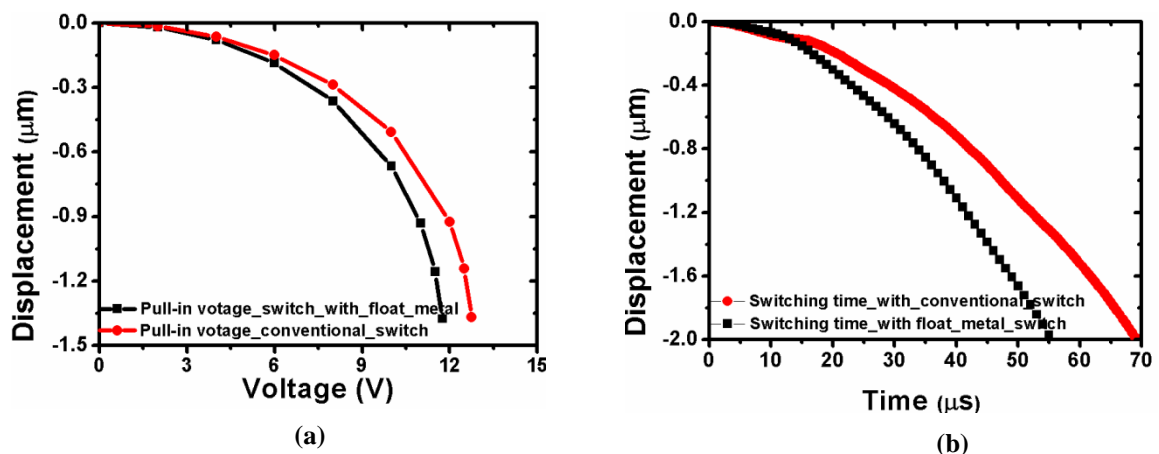
Figure 3.24 (a) Pull-in voltage analysis of both switches (b) Pull-in time of both switches.

FEM simulated pull-in time of both switches have been given in Fig. 3.24 (b). Float metal switch has less pull-in time as compared to conventional design due to decrease in mass through reduced central overlap area.

In summary, the switch with the conventional approach and using the float metal concept has been designed and investigated. The considerable improvement in insertion loss has been seen as compared to the conventional switch. OFF-state response is approximately same in both the devices. In float metal switch bandwidth is increased around 2.5 times than that of the conventional switch. Input power is increased around 4 times without self bias and hold down problem. The pull-in voltage and switching time has also reduced from 12.75 V to 11.75 V and 70 μs to 56.41 μs.

3.5 High-*k* Dielectric Material Based Switch

The shunt capacitive switches require higher down-state to up-state capacitance ratio in order to have good insertion loss and isolation. The large central overlap area, higher gap and materials with high dielectric constant can be used to achieve high C_{down}/C_{up} ratio. However, high insertion loss for the large central area and high pull-in voltage for higher gap puts the limit on the available options. Thus, a high-*k* dielectric option has been explored for shunt switch. In the proposed design, interdigitation of signal lines with actuation electrodes is considered [69, 70]. The compactness has been achieved further by incorporating *HfO₂* a high-*k* dielectric material in place of traditionally used *SiO₂*. Figure 3.25 shows the model of the switch. Switch is anchored on the ground plane of CPW. In OFF-state of switch there is a gap of 2 µm between switch and central conductor of CPW. The dimensions used in designing the device are given in Table 3.9.
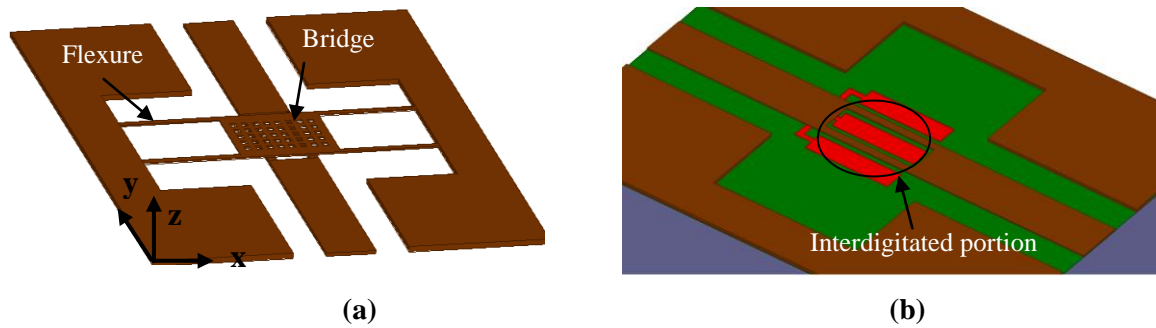
Figure 3.25: Capacitive switch (a) 3-D view (b) Interdigitated portion.

3.5.1 Electromechanical Response

The spring constant for a flexure with guided end is given by the equation (3.14) [60], where k_z = spring constant in the *z* direction, *E* (80 GPa) = Young's Modulus of the beam, *W* (10 µm) = width of flexure, *t* (1.5 µm) = thickness of flexure, *L* (150 µm) = length of flexure. As there are four such flexures in parallel so the equivalent spring constant of the structure is $K_z = 4k_z = 3.20$ N/m. Figure 3.26 shows the simulated result of pull-in voltage for the switch at *d* = 2.65 µm, 1.65 µm respectively.

Table 3.9: Dimensions of the designed switch.

Dimension	Value
Length of flexures (L)	150 μm
Width of flexures (W)	10 μm
Thickness of flexures	1.5 μm
HfO_2 thickness (t_{ox})	50 nm
Electrostatic Gap (d)	2.65 μm
Gap between bridge and transmission line (g)	2.0 μm
Central overlap area for switch	140×30 μm^2
Actuation area ($A_{\_a}$)	140×100 μm^2
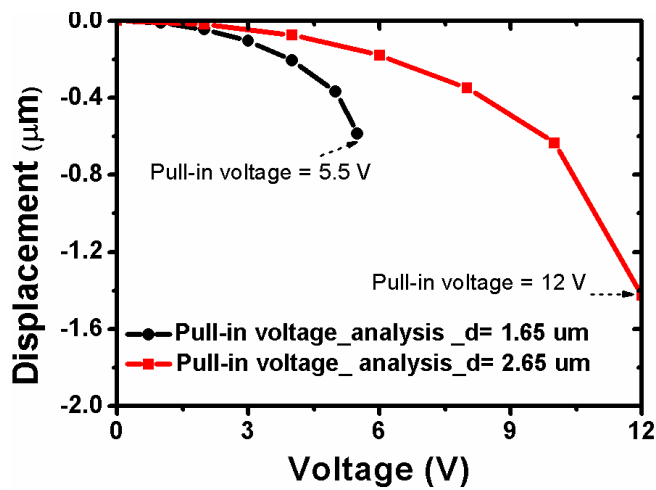
Figure 3.26: Pull-in voltage of the switch
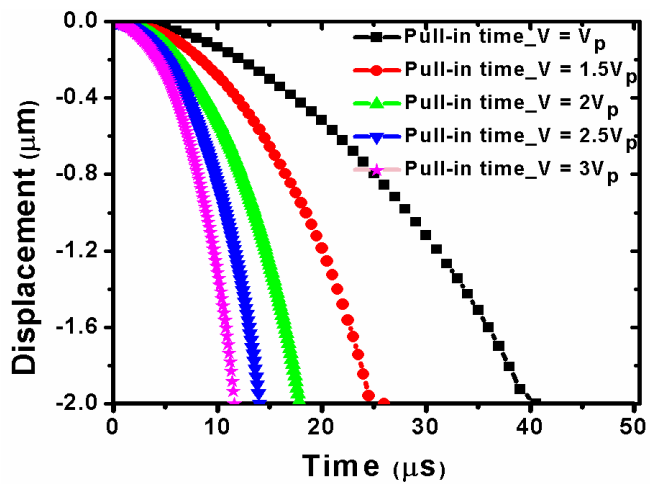
Figure 3.27: Switching time response of switch.

Figure 3.27 shows the switching time response for the switch. It is observed that bridge spends the majority of time in reaching the d/3 distance. Increasing the electrostatic force during this phase can decrease the switching time. This can be done by applying V/V_p ≥ 1, where V = supply voltage as shown in the Fig. 3.27.

3.5.2 RF Response

RF-MEMS capacitive switches use mostly SiO_2 as a dielectric material. However low dielectric constant requires larger overlap area for the same frequency band operation as compared to high-k dielectric material. High-k materials that can replace SiO_2 are Si_3N_4, Ta_2O_5, BST, strontium titanate oxide but HfO_2 ($\varepsilon_r = 20$) can be good alternate. It can be deposited up to 45 nm and has dielectric strength higher than 10 MV/cm. It also shows better resistance to dielectric charging and compatible with IC technology [71].

A. ON-state Response

Figure 3.28 shows the ON-state response of the switch. Device shows the insertion loss of 0.053-0.077 dB and 25.94-22.74 dB of return loss in X-band shown in the Figs. 3.28 (a) and 3.28 (b) respecitvely. It is observed that even at $g = 1$ μm, ON-state response is not affected much because of the reduced central overlap area due to high-k dielectric.

(a)

(b)
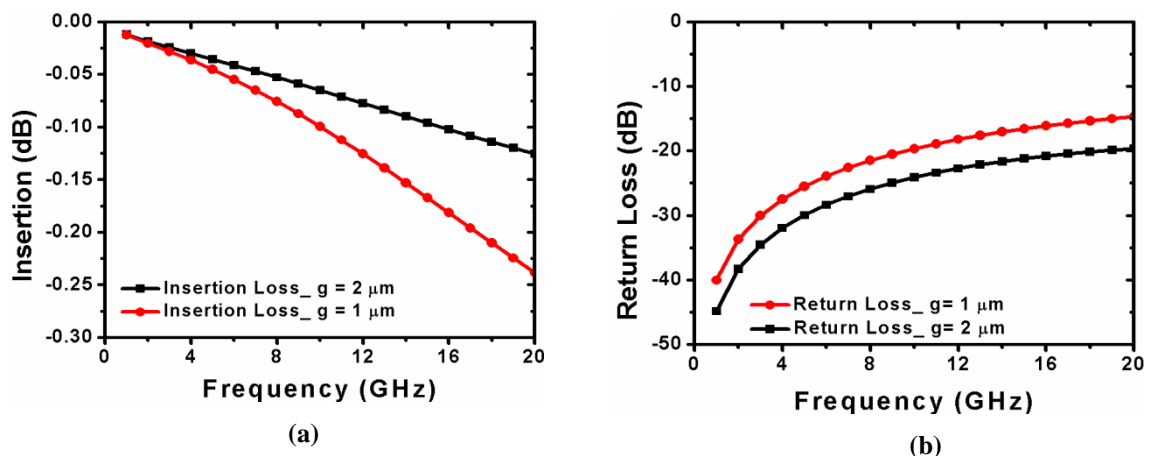
Figure 3.28: ON-state response of switch (a) Insertion loss (b) Return loss.

B. OFF-state Response

Figure 3.29 shows the OFF-state response of the switch. Device shows the isolation of 39.03-34.02 dB in X-band as shown in the Fig. 3.29 (a) with the optimum value of 52.72

dB at 9 GHz. Figure 3.29 (b) shows the return loss response of the switch during this state.

(a)　　　　　　　　　　　　　　　　　(b)
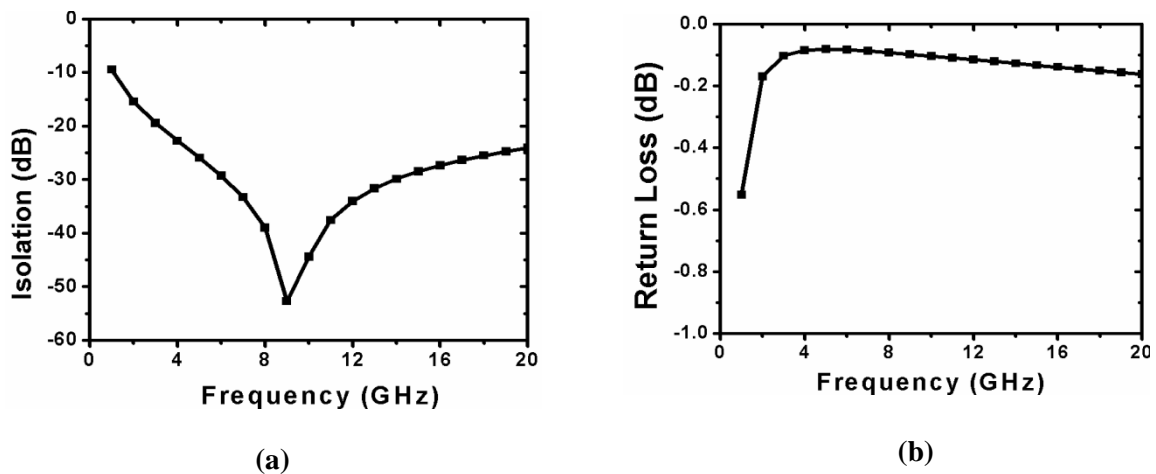
Figure 3.29: OFF-state response of switch (a) Isolation (b) Return loss.

In summary, a shunt capacitive RF-MEMS switch with *HfO₂* has been investigated. It is observed that switch shows significant improvement in RF and electromechanical performances with higher compactness as compared to the *SiO₂* based switch discussed in section 3.3. Further the switches with the same dimensions and masks having different dielectric materials can be tuned to different frequency bands. The designed switch can be a good alternate for the future wireless trans-receivers as compared to the conventional RF-MEMS switches.

3.6 Conclusion

The improved closed form expressions for pull-in time by incorporating the gap dependency of the electrostatic force has been derived and validated through 3-D FEM simulation. The results obtained from new expression differ only by 5 % compared to 3-D FEM simulated values. It is also observed that material with high value of E/ρ provide high switching speed. Further, a capacitive switch based on the conventional approach has been designed and investigated. The switch response has been compared with a device based on a floating metal concept. The considerable improvement in ON-state response, bandwidth and input power has been achieved as compared to the conventional switch. The OFF-state response is same for both the devices. Further, a compact switch with high-*k* dielectric material (*HfO₂*) has been designed and investigated. Significant improvement in RF, electromechanical performance with higher compactness has been

obtained as compared to the switch with SiO_2. The designed switches can be a good alternate for the wireless trans-receivers as compared to the conventional RF-MEMS switches.

Chapter - 4

Reconfigurable Multi-band Switches

4.1 Introduction

Switches discussed in chapter-3 doesn't have reconfigurable feature and thus are not compatible with multi-band wireless systems. To address this issue, this chapter presents the switches which can be used in the reconfigurable RF front-end and hence significantly reduce the number of components, hardware complexity, and cost of the system. Reconfigurable switches are based on a novel approach. This approach provides flexibility of changing the down-state inductance value and therefore the isolation optimum value can be tuned to the different frequency bands. The non-uniform cantilever structures are used for switch implementation. Further, symmetric and asymmetric structures are used on either side of the transmission line. The asymmetric structure based capacitive device has been combined with the ohmic switch in order to make a broadband device with the capability of shifting the OFF-state optimum value to the different bands.

4.2 Interdigitated Multi-band Capacitive Switch

4.2.1 Description of Switch

This section presents a novel capacitive shunt RF-MEMS switch. In the proposed design, as shown in the Fig. 4.1 broadside bridge structure is joined with two cantilevers on either side has been used to implement the switch. Thus, down-state inductance value can be changed by actuating either left, right or both cantilevers to the down-state along with the movable bridge structure. This control over the down-state inductance value can't be achieved with the conventional capacitive switches [16, 20, 49, 68, 72-76].
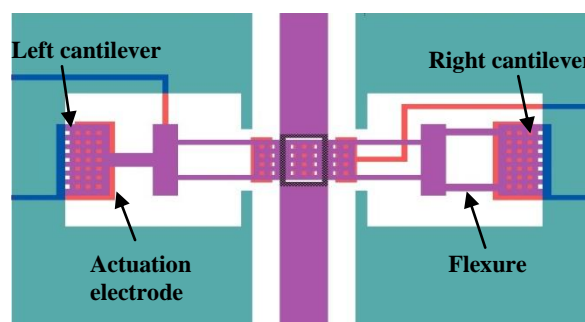
Figure 4.1: Layout of the Switch.

This also brings the multi-band functionality as the optimum isolation can be shifted in the different frequency bands. In order to improve the ON-state response, the capacitance in the up-state has been reduced through a small capacitor in series with the central capacitor. This is the novel way of reducing the up-state capacitance. Further, actuation electrodes are interdigitated with the central conductor of CPW in order to reduce the area occupied by the switch [70, 77]. Device dimensions are listed in Table 4.1.

Table 4.1: Dimensions of the designed switch.

Dimension	Value
Length of bridge flexures	145 μm
Length of left and right cantilever flexures	95 μm
Thickness of all flexures	1.5 μm
Width of bridge flexure	10 μm
Width of left cantilever flexure	30 μm
Width of right cantilever flexure	15 μm
Central overlap area	310×10 μm^2
Overlap area between ground and left, right cantilever	160×15 μm^2

4.2.2 Working of Switch

The conventional capacitive switch operates in one of the two states. With up-state of the bridge, the device is in the ON-state, whereas down-state corresponds to OFF-state. The switch has only one resonant frequency. The device discussed in this section operates in four states. Figure 4.2 (a) shows the ON-state as all beams are in the up position.
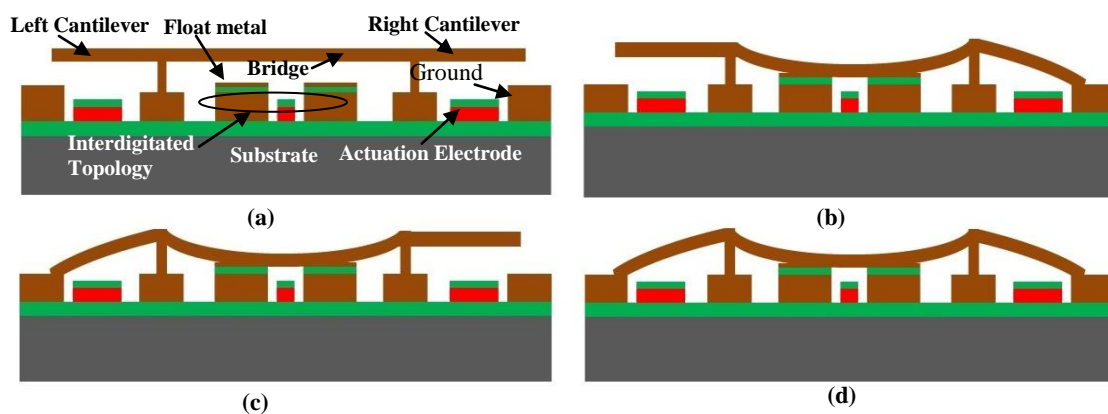
Figure 4.2: Cross-sectional view for switch working (a) ON-state (b-d) OFF-state.

The signal flows from input port to the output port. OFF-state can be achieved by actuating the bridge structure down either with left, right or both cantilevers as shown in Figs.4 (b)-(d). The asymmetric structures of cantilever provide three resonant frequencies in the down-state.

4.2.3 RF Response

A. ON-state Response

In the ON-state, the switch can be modeled as a capacitor in shunt with the transmission line. RF response during this state can be improved by decreasing the up-state capacitance. The presented device forms two small additional capacitors as compared to the conventional approach based switch. These additional capacitors are connected in parallel, whereas their combination is connected in series with the central capacitor. This reduces the overall capacitance of the switch. Switch shows insertion loss of 0.02 dB to 0.11 dB and return loss of 53.04 to 23.67 dB over the frequency range from 1 GHz to 25 GHz as shown in Fig. 4.3.
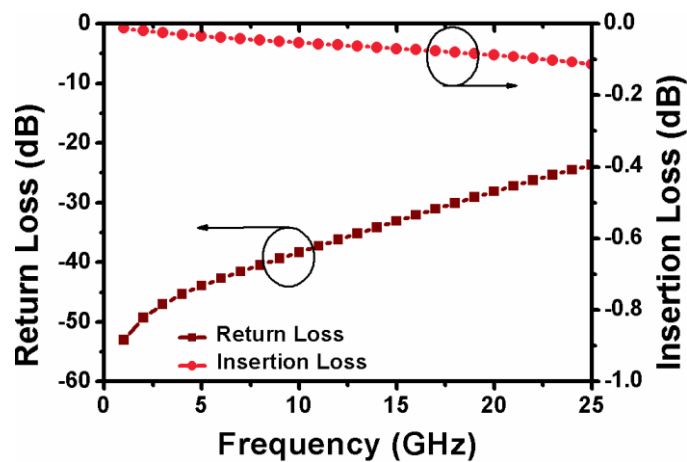
Figure 4.3: ON-state response of the switch.

B. OFF-state Response

Switch shows isolation when either of the cantilever is in down-state along with bridge structure. The asymmetric structure on either side of transmission line shifts the isolation peaks to the different frequency bands. Figure 4.4 shows the isolation characteristics of the device when the bridge is in the down position along with both cantilevers. Isolation peak of 40.7 dB has been observed at 21.4 GHz. As resonant frequency is the function of

the capacitance and inductance, pulling down the left cantilever with the bridge structure shifts the isolation peak to the *X*-band. A peak value of 34.71 dB has been observed at 10.4 GHz as shown in Fig. 4.4. As the right cantilever is having less inductance than the left, switching it down with bridge shifts the isolation peak to a higher frequency as compared to the left cantilever case. Isolation peak of 34.33 dB has been observed at 11 GHz.
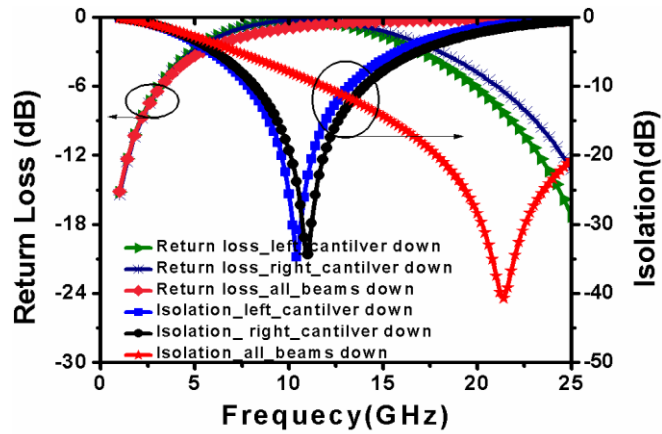
Figure 4.4: OFF-state response of the switch.

C. Lumped Parameter Extraction

From Fig. 4.3, return loss of 53.04 dB at 1 GHz has been substituted into equation (3.40) for calculating the capacitance in up-state [40].
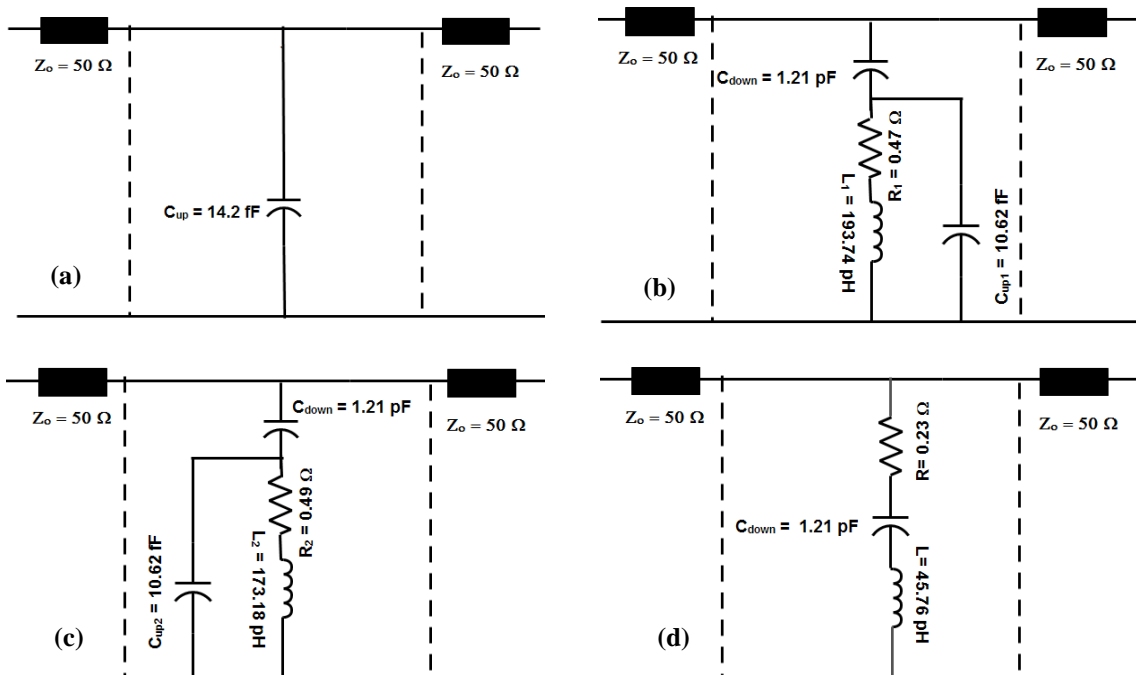
Figure 4.5: Electrical lumped model of the switch (a) Up-state (b-d) Down-state.

From Table 4.2, it can be observed that extracted up-state capacitance is higher than the calculated value as it includes the fringing field capacitance. C_{down} can be extracted at a frequency $f << f_o$ from the S_{12} plot when the switch is in the actuated state. From Fig. 4.4, substituting a value of 0.15 dB at 1 GHz into the equation (3.42) provides a down-state capacitance of 1.21 pF.

Table 4.2: Extracted values of switch parameters.

Parameters	Value
C_{up} (calculated)	8.33 fF
C_{up} (extracted)	14.20 fF
C_{down} (calculated)	1.10 pF
C_{down} (extracted)	1.21 pF
C_{ratio} (calculated)	132
C_{ratio} (extracted)	85
R (extracted_all beams down)	0.23 Ω
R_1 (extracted_ left cantilever down)	0.47 Ω
R_2 (extracted_ right cantilever down)	0.49 Ω
L (all beams down)	45.76 pH
L_1 (left cantilever down)	193.74 pH
L_2 (right cantilever down)	173.18 pH

For inductance calculation, equation (3.34) has been used. Inductance of 193.74 pH, 173.18 pH and 45.76 pH has been obtained at 10.4 GHz, 11 GHz and 21.4 GHz respectively. The switch electrical model has been given in Fig. 4.5 (a)-(d), where $Z_o =$ characteristic impedance of input and output CPW line, C_{up1}, $C_{up2} =$ capacitance between the ground and left and right cantilevers respectively [40, 61]. Resistances of 0.23 Ω, 0.49 Ω, and 0.47 Ω is extracted at three resonate frequencies, i.e. 21.4 GHz, 11.0 GHz, and 10.4 GHz respectively, using equation (3.47).

D. Switch Bandwidth

It is observed from Fig. 4.6 that upper operating frequency of the switch is limited by insertion loss. The switch has f_L = 17.8 GHz and f_U = 23 GHz. This results in a bandwidth of 5.2 GHz in K-band. Figure 4.7 (a) shows the bandwidth for right cantilever down case, having f_L = 10.1 GHz and f_U = 11.8 GHz. In case of left cantilever, f_L = 9.6 GHz and f_U = 11.2 GHz as shown in Fig. 4.7 (b). The Device has a bandwidth of 2.2 GHz in X-band.
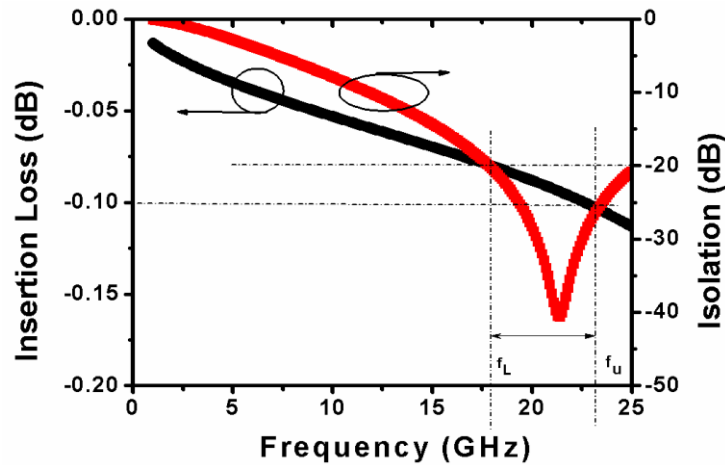
Figure 4.6: Bandwidth of switch with all beams to the down-state.

(a)   (b)
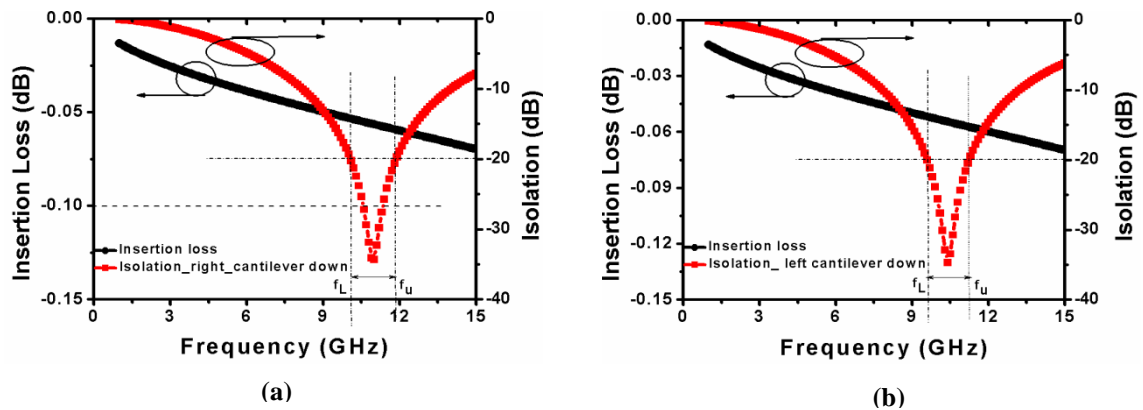
Figure 4.7: Bandwidth of switch with bridge to the down-state with (a) Right cantilever (b) Left cantilever.

Figure 4.8 shows the simulated pull-in analysis for the designed switch. The bridge structure has a pull-in voltage of 12.25 V, whereas left and right cantilevers have 7.5 V. The same pull-in voltage has been obtained for either cantilever because of the identical spring constant. The analytical formula for calculating the spring constant for a non-uniform cantilever has been derived the next section. Under dynamic response, FEM

simulated switching time has been given in Fig. 4.9. Bridge shows a pull-in time of 34.40 µs on the other hand, both cantilevers have 57 µs.
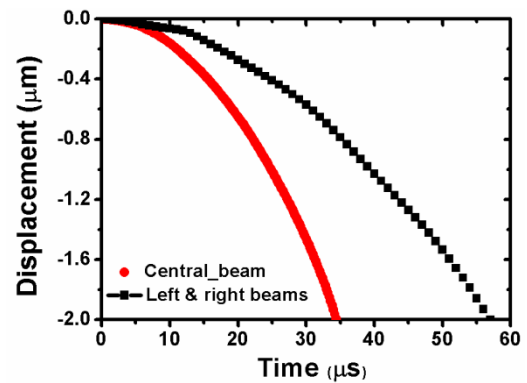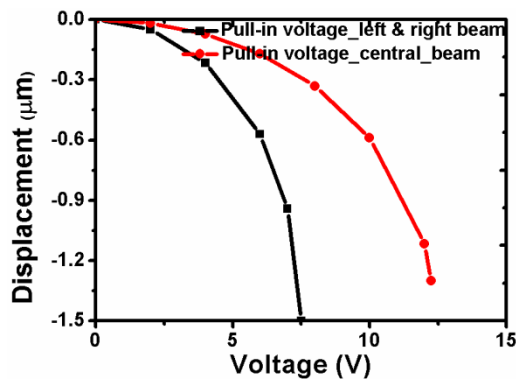
Figure 4.8: Pull-in voltage analysis of the switch.   Figure 4.9: Switching time of the switch.

In summary, a new type of capacitive shunt RF-MEMS switch has been designed and investigated. The switch structure provides variable inductance in the actuated state and thus can operate in the *X* and *K* bands.

4.3 Cantilever Based Multi-band Capacitive Switch

4.3.1 Description of Switch

MEMS switches are generally implemented with either bridge type or cantilever type of structures. The cantilever type structures are mostly not used for the implementation of the capacitive shunt switch. This is imputable to the fact of higher inductance associated with the cantilever based structure as compared to a bridge realized by joining two cantilevers on either side of the transmission line. Thus, for achieving the isolation peak at some desire frequency down-state capacitance contribution is less. On the other hand, cantilever structure based switches have low spring constant and hence low pull-in voltage. Further, the switch will also have less pull-in and release time as compared to the same stiffness bridge based device due the less mass in the cantilever based switch. This work presents a novel design which takes the advantages of both types of structures. The switch is implemented with cantilever on either side of the transmission line. A number of structures have been reported in the literature for the capacitive switches having good RF performance in a single band, moderate pull-in voltage, but lags in multi-band functionality [16, 20, 49, 68, 72-76].

In the proposed design, down-state inductance value is changed by actuating either or both cantilevers to the down-state. This control over the down-state inductance value can't be achieved with the conventional capacitive switches. This also brings the multi-band functionality as the optimum isolation can be shifted in the different bands. Further, In order to improve the ON-state response, the capacitance in the up-state has been reduced by using a float metal layer over the dielectric layer. This has been achieved without affecting the down-state response. Float metal also makes the down-state behavior predictable in terms of resonant frequency. The device has low pull-in voltage as the switch is implemented with cantilever type of structure on either side of the transmission line. In the up-state, free end of the cantilever has an overlap area of 150×10 μm^2 with the floating metal layer. The width of the overlap is limited by the fabrication constraint i.e. resolution of the lithography. As the cantilevers are in parallel, the total overlap area will be 150×20 μm^2. Figure 4.10 shows the model of the switch. Device dimensions are listed in Table 4.3.
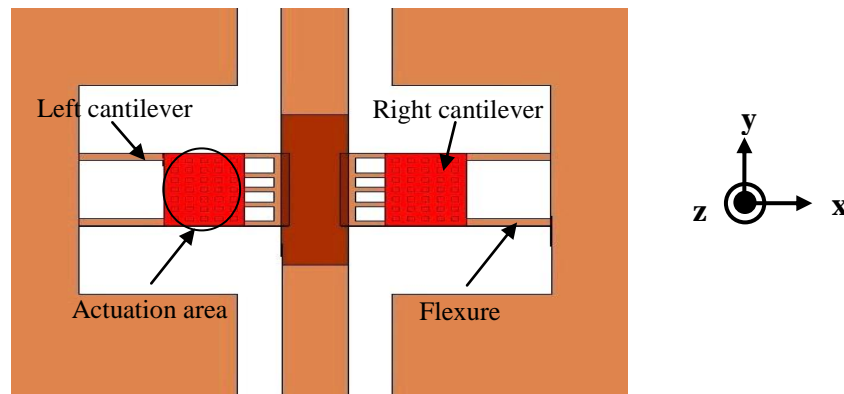
Figure 4.10: Model of the Switch.

Table 4.3: Dimensions of the designed switch.

Dimension	Value
Length of cantilever flexures	115 μm
Width of cantilever flexures	15 μm
Thickness of all flexures	2 μm
Electrostatic Gap (d)	2.7 μm
Gap between transmission line and bridge (g)	2.0 μm
Overlap area between cantilever and transmission line	150×10 μm^2
Actuation Electrode area (A_a)	110×150 μm^2

4.3.2 Working of Switch

The proposed switch has four different physical states (three different electrical states). With both cantilevers in the up position, the signal flows from the input port to the output port and the device is in the ON-state as shown in Fig. 4.11 (a). OFF-state can be achieved by actuating the either or both cantilevers to down-state as shown in Figs. 4.11 (b)-(d). The device shows two resonant frequencies in the OFF-state.
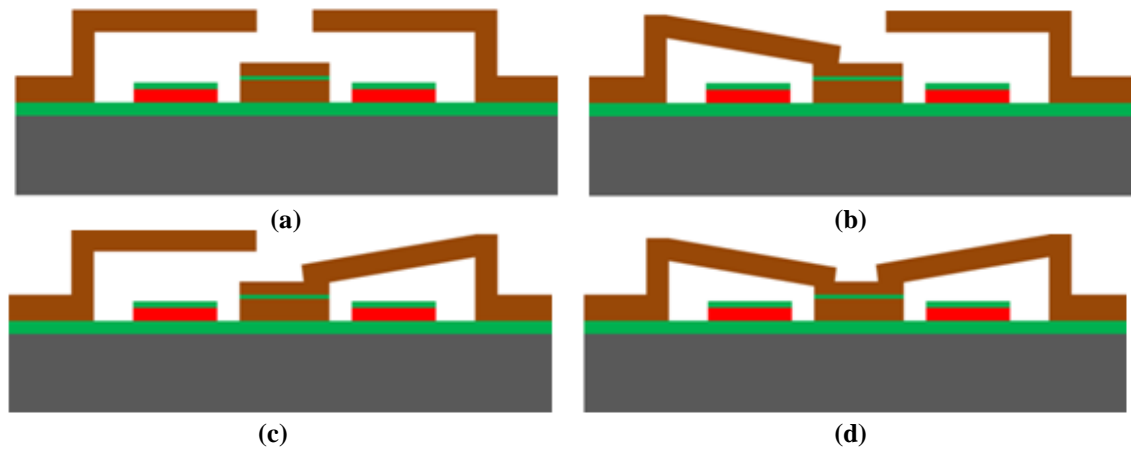
Figure 4.11: Cross-sectional view for the working of proposed switch (a) ON-state (b-d) OFF-state.

4.3.3. RF Response

A. ON-state Response

The proposed switch shows insertion loss of 0.01-0.10 dB in the frequency range 1 GHz to 25 GHz as shown in Fig. 4.12 (a). Return loss response is shown in the Fig. 4.12 (b).
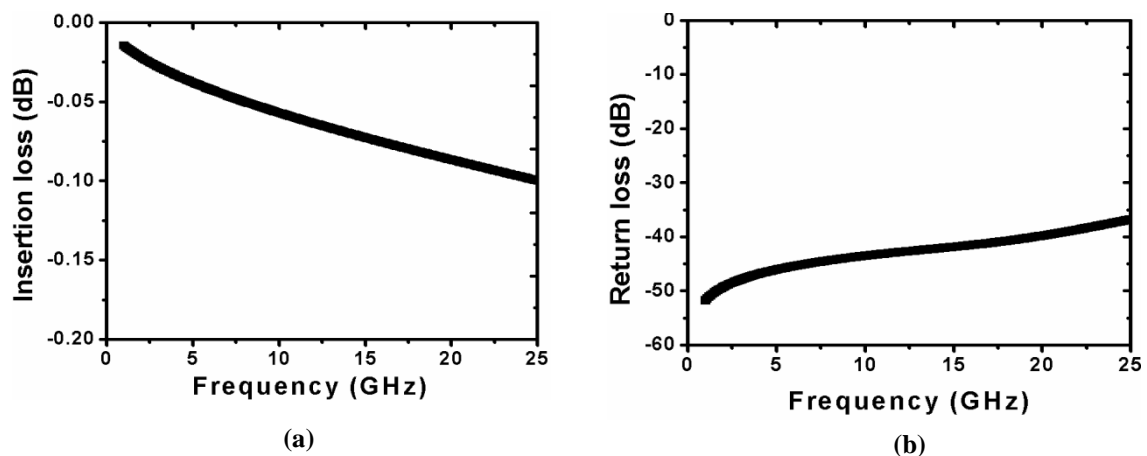
Figure 4.12: ON-state response of the switches (a) Insertion loss (b) Return loss.

B. OFF-state Response

In OFF-state isolation optimum value has been tuned to C and X bands through cantilever structures by changing the down-state inductance. The propose device has optimum isolation 54.56 dB at 9.8 GHz when both cantilevers are electrostatically actuated to the down-state as shown in Fig. 4.13 (a). As resonant frequency is the function of the down-state capacitance and inductance, pulling down the either cantilever shift the optimum isolation to C-band. A maximum isolation of 48.80 dB at 4.5 GHz. The resonant frequency has been decreased due to the increase in the down-state inductance value. Further, the higher inductance value is also responsible for the narrow OFF-state response. As the identical cantilevers are used, the OFF-state response will be same in case of either cantilever actuated to the down-state. The Return loss during OFF-state has been shown in Fig. 4.13 (b), and is minimum at the resonant frequency.
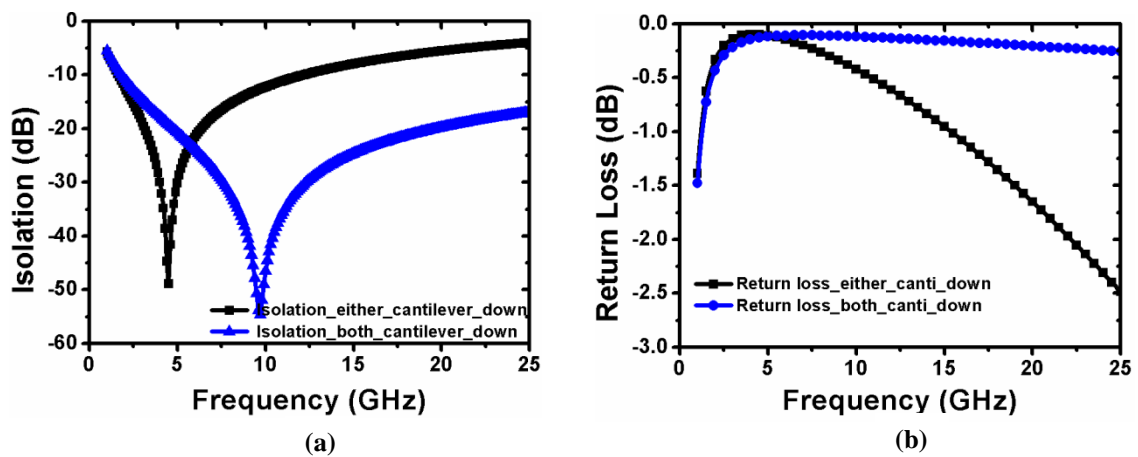
Figure 4.13: OFF-state response (a) Isolation (b) Return loss.

4.3.4. Electromechanical Response

A. Spring Constant Modeling

This section presents the analytical model for calculating the spring constant for non-uniform cantilever type of structure. The side view of the proposed cantilever has been shown in the Fig. 4.14. The total Length of the cantilever is L' and 'a' is the length from the anchor to the start location of the actuation electrode and 'L' is the extended till the end of the actuation electrode. The cantilever is designed such that it is wide above the actuation electrode position. This has been done in order to provide the higher actuation force with lower spring constant value. Cantilever is of width 'w' from the anchor point to the location where actuation electrode starts thereafter width is '$w*y$', where y is a

constant and is kept *y>1* for reducing the pull-in voltage. The beam thickness is '*t*' and a distributed force '*q*' is acting per unit length on the wider portion. The spring constant is derived using the Euler-Bernoulli theory [55].
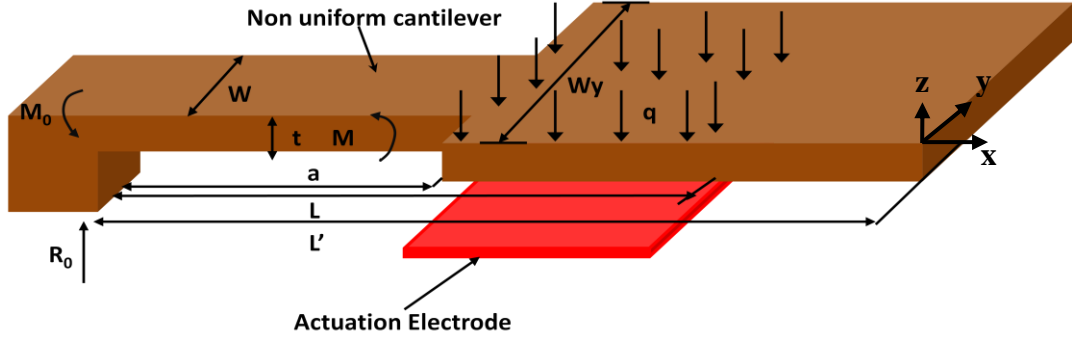
Figure 4.14: Side view of the non-uniform cantilever with force moment diagram.

The moment M_o working at the anchor of the cantilever is given by

$$M_o = q(L - a)\left[a + \frac{L - a}{2}\right]$$

(4.1)

The reaction force acting at the anchor of the cantilever is given by

$$R_o = q(L - a)$$

(4.2)

The equation of moment working in the region $0 \leq x \leq a$

$$M = q(L - a)x - \frac{q(L^2 - a^2)}{2}$$

(4.3)

Inserting the equation (4.3) into the moment-curvature relation [55], we get

$$EIv'' = q(L - a)x - \frac{q(L^2 - a^2)}{2}$$

(4.4)

where E = modulus of elasticity, $I = wt^3/12$ = moment of inertia and v = deflection.

$$v' = \frac{1}{EI}\left[\frac{q(L - a)x^2}{2} - \frac{q(L^2 - a^2)x}{2}\right] + C_1$$

(4.5)

Using the boundary condition at $x = 0$, $v' = 0$, gives $C_1 = 0$ and hence

$$v' = \frac{1}{EI}\left[\frac{q(L-a)x^2}{2} - \frac{q(L^2-a^2)x}{2}\right] \tag{4.6}$$

Integrating the above equation w.r.t 'x' again, we get

$$v = \frac{1}{EI}\left[\frac{q(L-a)x^3}{6} - \frac{q(L^2-a^2)x^2}{4}\right] + C_2 \tag{4.7}$$

Using the boundary condition at $x = 0$, $v = 0$, gives $C_2 = 0$ and hence

$$v = \frac{1}{EI}\left[\frac{q(L-a)x^3}{6} - \frac{q(L^2-a^2)x^2}{4}\right] \tag{4.8}$$

The equation of moment working in the region $a \leq x \leq L$

$$M = q(L-a)x - \frac{q(L^2-a^2)}{2} - \frac{q}{2}(x-a)^2 \tag{4.9}$$

Inserting equation (4.9) into the moment-curvature relation, we get

$$EIyv'' = q(L-a)x - \frac{q(L^2-a^2)}{2} - \frac{q}{2}(x-a)^2 \tag{4.10}$$

$$v'' = \frac{1}{EIy}\left[qLx - \frac{qL^2}{2} - \frac{qx^2}{2}\right] \tag{4.11}$$

By integrating equation (4.11), we get

$$v' = \frac{1}{EIy}\left[\frac{qLx^2}{2} - \frac{qL^2x}{2} - \frac{qx^3}{6}\right] + C_3 \tag{4.12}$$

Using the continuity of the slope at $x = a$ and simplifying we get

$$C_3 = \frac{qaL(a-L)\left(1-\frac{1}{y}\right)}{2EI} + \frac{qa^3}{6EIy} \tag{4.13}$$

By integrating equation (4.12) again, we get

$$v = \frac{1}{EIy}\left[\frac{qLx^3}{6} - \frac{qL^2x^2}{4} - \frac{qx^4}{24}\right] + C_3x + C_4 \tag{4.14}$$

Using the continuity of the deflection at $x = a$ and simplifying we get

$$C_4 = \frac{qa^2 L(3L - 4a)}{12EI}\left(1 - \frac{1}{y}\right) + \frac{qa^4}{12EI}\left(1 + \frac{1}{2y}\right) - \frac{qa^4}{6EIy} \tag{4.15}$$

For section $L \leq x \leq L'$

$$E(Iz)v'' = 0 \tag{4.16}$$

By integrating the equation (4.16), we get

$$E(Iz)v' = C_5 \tag{4.17}$$

By integrating the equation (4.16) again, we get

$$E(Iz)v = C_5 x + C_6 \tag{4.18}$$

From equations (4.17) and (4.18)

$$v' = \frac{C_5}{EIz} \tag{4.19}$$

$$v = \frac{C_5}{EIz}x + \frac{C_6}{EIz} \tag{4.20}$$

Putting $x = L'$ in equation (4.20)

$$v_{L'} = \frac{C_5 L' + C_6}{EIz} \tag{4.21}$$

and at $x = L$ in equation (4.20)

$$v_L = \frac{C_5 L + C_6}{EIz} \tag{4.22}$$

or

$$C_6 = v_L EIz - C_5 L \tag{4.23}$$

Putting the value of C_6 in equation (4.21)

$$v_{L'} = \frac{C_5 L' + v_L EIz - C_5 L}{EIz} \tag{4.24}$$

Simplifying the equation (4.24), we get

$$v_{L'} = \frac{C_5(L' - L)}{EIz} + v_L \tag{4.25}$$

From equation (4.17) at $x = L$

$$EIzv'_L = C_5 \tag{4.26}$$

From equation (4.12) after putting C_3 value and at $x = L$, we get

$$v'_L = \frac{-qL^3}{6EIy} + \frac{qaL(a - L)\left(1 - \frac{1}{y}\right)}{2EI} + \frac{qa^3}{6EIy} \tag{4.27}$$

Substituting the v'_L value into the equation (4.26), we get

$$C_5 = z\left[\frac{q(a^3 - L^3)}{6y} + \frac{qaL(a - L)\left(1 - \frac{1}{y}\right)}{2}\right] \tag{4.28}$$

From equation (4.14) after substituting the value of C_3 and C_4 and at $x = L$

$$v_L = \frac{-q}{8EIy}(L - a)^2(L + a)^2 - \frac{q}{12EI}(L - a)a^2(a + 3L) \dots \tag{4.29}$$
$$- \frac{qaL}{2EI}(L - a)^2\left(1 - \frac{1}{y}\right)$$

Putting the values of v_L and C_5 in equation (4.25), we get

$$v_{L'} = [\frac{(L^2 - a^2)^2}{8y} - \frac{(L' - L)}{6y}(a^3 - L^3) + \frac{aL}{2}(1 - 1/y)\{(L - a)^2 \dots \tag{4.30}$$
$$+ (L - a)(L' - L)\} + \frac{a}{12}(L - a)(a + 3L)]$$

Now

$$k = \frac{-q(L - a)}{v_{L'}} \tag{4.31}$$

Thus

$$k = \frac{24EIy}{3(L - a)(L + a)^2 + 4(L' - L)(a^2 + L^2 + aL) + 12\,aL\,(y - 1)(L' - a) + 2a^2y(a + 3L)} \tag{4.32}$$

If there are two such beams from the anchor location, then the above expression can be modified as given below

$$k = \frac{48EIy}{6(L-a)(L+a)^2 + 8\,(L'-L)(a^2+L^2+aL) + 12\,aL\,(y-2)(L'-a) + 2a^2y(a+3L)} \quad (4.33)$$

By putting the values of all the unknown in the equation (4.33) i.e., $L' = 285$ μm, $L = 225$ μm, $a = 115$ μm, $E = 80$ GPa and $y = 10$, gives $k = 0.51$ N/m. The result obtained from the analytical equation (4.33) has also been compared with the FEM simulated value. For FEM simulation, an evenly distributed force of 0.96 μN has been applied to the part of the cantilever, which is directly above the actuation electrodes and of equal area. This corresponds to a maximum displacement of 2 μm at the tip of the cantilever. The spring constant of 0.48 N/m was extracted from the relation K (spring constant) $= F$ (force)/ Z (maximum displacement), which closely matches with the value calculated from the equation (4.33).

B. Pull-in Voltage

Under electromechanical simulation, the actuation voltage is applied through the poly-*Si* electrodes which are placed 115 μm from the anchor location. The cantilevers have pull-in voltage of 6 V as shown in Fig. 4.15, which agrees within 25 % with the calculated pull-in voltage of 4.48 V. The perforations in the hanging structure accounts for the difference between the two values. Further, the cantilevers have been designed to achieve equal pull-in voltage.
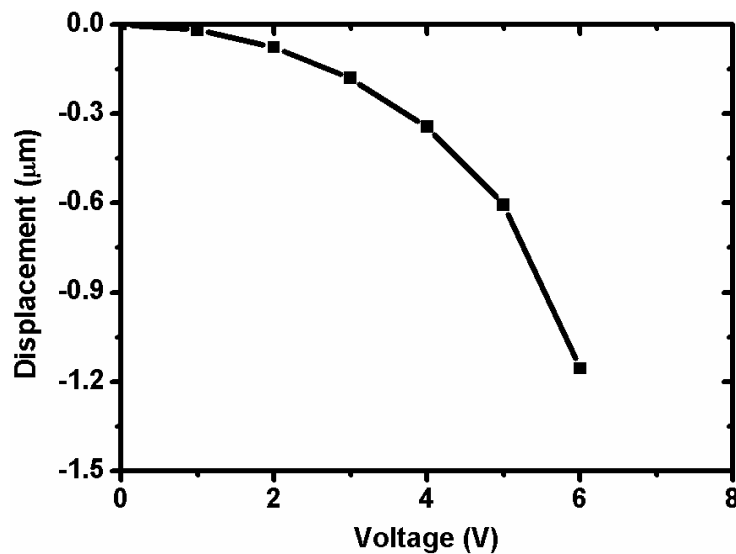
Figure 4.15: Pull-in voltage analysis of the switch.

B.1. Effect of Residual Stress on Pull-in Voltage

In MEMS technology, thin film movable structures can deform as a result of residual stress. The stress in thin films can be divided into two types: extrinsic, such as stresses arising from the mismatch in thermal expansion coefficients and intrinsic such as stresses from the nucleation and growth of film deposition. In the first order approximation, general uniaxial residual stress in a thin film can be given by the equation (4.34) [78], where z = coordinate across the thickness (h) with origin chosen at the film's mid plane, σ_0 = mean stress, σ_1 = gradient stress, and σ_{total}= superposition of mean and gradient stress.

$$\sigma_{total} = \sigma_0 + \sigma_1 \left(\frac{z}{\frac{h}{2}} \right) \tag{4.34}$$

When a cantilever is released by removing the sacrificial layer, hanging structure becomes free to deform out-of-plane in the form of bending up or down after the relief from gradient stress that existed in the thin film. The mean stress also causes out-of-plane deformation in the form of tilt or rotation of the structure due to the in-plane deformation of the portion of the cantilever which is still bonded with the substrate. From the previously reported literatures, mean stress was found to vary between 0 MPa to 150 MPa, whereas stress gradient was by order of 4 MPa/μm for electroplated gold [79-82]. Stress is tensile in nature. The tilt and bending of the beam structure and their effect on the pull-in voltage has been simulated through Coventorware[(R)] for the range of stress given above. The deformed shape of the cantilever with different mean stress is shown in Fig. 4.16 (a).
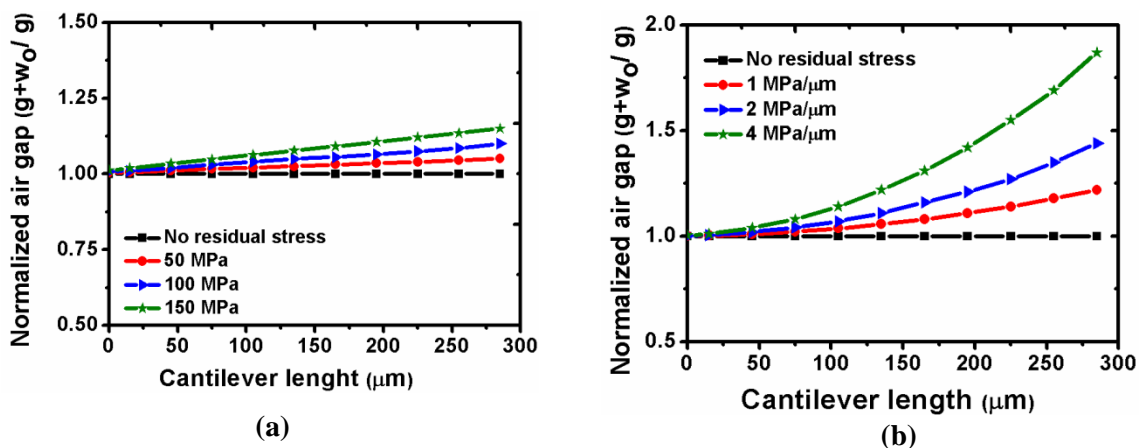
Figure 4.16: Deformed shape of cantilever due to (a) Mean stress (b) Gradient Stress.

(a)   (b)
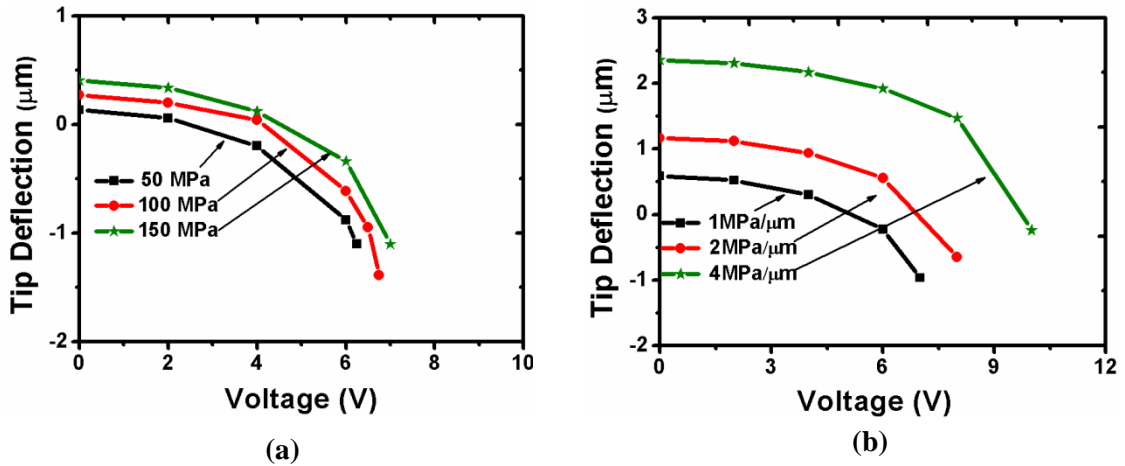
Figure4.17: Pull-in analysis (voltage applied at the actuation pad vs. tip deflection) when the cantilever is subjected to (a) Mean stress (b) Gradient stress.

A cantilever with a more mean stress has a larger normalized air gap, where w_o is the deformation along the length of the cantilever. The cantilever is tilted in $+z$ direction due the tensile mean stress alone. The maximum tip deflection has been increased from 0.2 μm to 0.41 μm as stress is changed from 50 MPa to 150 MPa.

Figure 4.16 (b) shows out of plane deflection of cantilever due the stress gradient acting alone. The cantilever has curled up in +z direction. The maximum tip deflection has been increased from 0.59 μm to 2.35 μm as stress is changed from 1MPa/μm to 4 MPa/μm. Figure 4.17 (a) shows the simulated results for cantilever tip deflection as a function of applied voltage subjected to the mean stress. The Pull-in voltage has been increased from 6 V to 8 V as the residual stress value is changed from 0 MPa to 150 MPa, whereas pull-in voltage of 10 V has been observed at a stress gradient of 4MPa/μm as shown in Fig. 4.17 (b).

Figure 4.18: Deformed shape of cantilever subjected to mean and gradient stress.

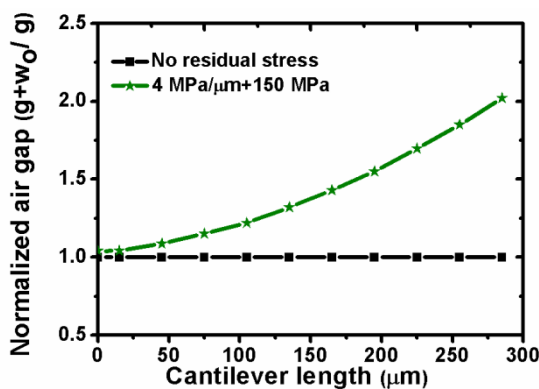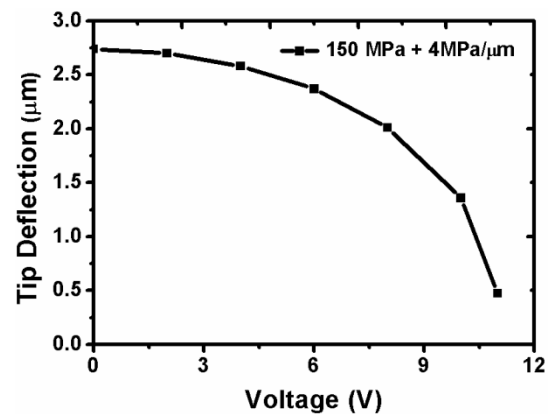Figure 4.19: Pull-in analysis of the cantilever subjected to mean and gradient stress.

In practice, deformations of a cantilever based structure subjected to mean and gradient stress, have both curling and tilt related deformation. Considering the mean stress of 150 MPa and a gradient of 4 MPa/μm deformation in the beam has been simulated for this extreme case as shown in Fig. 4.18. Further, a pull-in voltage of 11 V has been obtained for this case as shown in the Fig. 4.19.

In summary, a new type of capacitive shunt RF-MEMS switch has been investigated. In OFF-state, isolation peaks have been shifted in C and X bands by actuating either or both cantilevers to the down-state. Further, considerable reduction in pull-in voltage has been obtained as compared to the bridge based structures. Device also shows considerable improvement in the ON-state response as compared to the conventional switch presented in this thesis.

4.4 Asymmetric Structure Based Capacitive Switch

This section presents a capacitive shunt RF-MEMS switch, where asymmetric structure has been used on either side of the transmission line to implement the device. This novel structure is used to inductively tune the isolation in C, X and K bands. Figure 4.20 (a) shows the model of the designed switch and SEM micrograph of the fabricated device is shown in the Fig. 4.20 (b). The switch design parameters are listed in Table 4.4. The device can operate in four different states. With both cantilever in the up position, the switch is ON and shows insertion loss. OFF-state can be achieved by pulling down the left, right or both cantilever in the down position through electrostatic actuation. As the left cantilever is having less inductance than the right cantilever, switching it down shift the isolation peak to a higher frequency. With all beams are in down position inductance becomes even less and shifts the isolation peak to a much higher frequency.

(a)   (b)
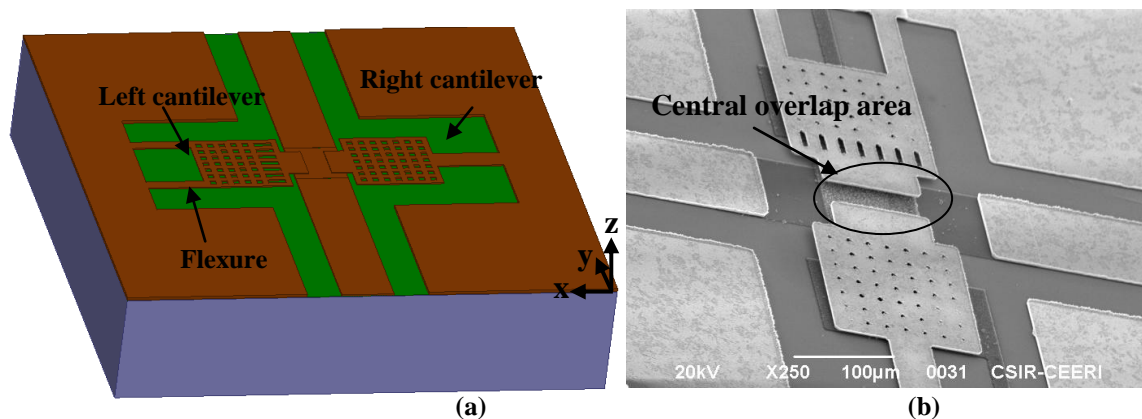
Figure 4.20: (a) Model of the switch (b) SEM micrograph of the fabricated switch.

Table 4.4: Dimensions of the designed switch.

Dimension	Value
Length of left cantilever flexures	100 μm
Width of left cantilever flexures	15 μm
Length right cantilever flexure	115 μm
Width of right cantilever flexure	30 μm
Thickness of all flexures	1.5 μm
Overlap area between cantilevers and transmission line ($A_{up\_pro)}$	70×50 μm^2

4.4.1 RF Response

A. ON-state Response

Device shows insertion loss of 0.01 dB-0.10 dB has been observed in the frequency range from 1 GHz to 25 GHz as shown in Fig. 4.21. The device shows return loss of 55.16 dB-26.36 dB in the frequency range from 1 GHz to 25 GHz as shown in Fig. 4.22.
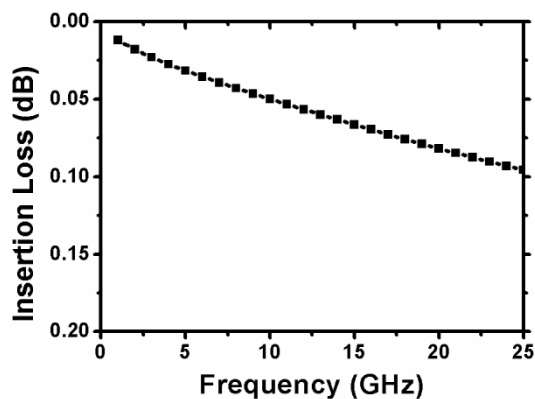
Figure 4.21: Insertion loss of switch.   Figure 4.22: Return loss of the switch.
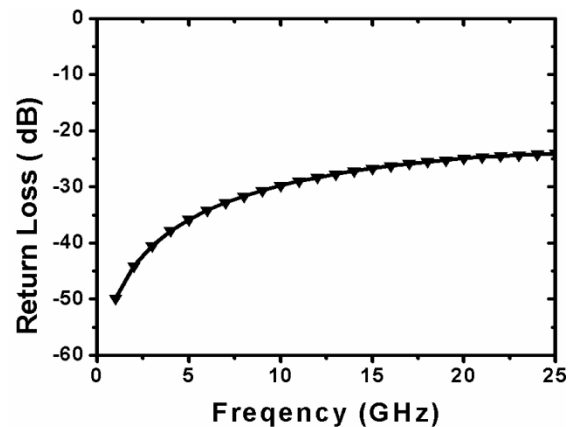
B. OFF-state Response

In addition to reducing the up-state capacitance float metal concept also allows to make asymmetric structures on either side of the transmission line and thus isolation peaks can be tuned to different bands. Figure 4.23 shows the isolation characteristics the device. A peak value of 42.72 dB, 43.98 dB has been observed at 7.3 GHz, 8.7 GHz when right

and left cantilevers are electrostatically actuated in the down-state respectively. As resonant frequency is the function of the capacitance and inductance, pulling down the both cantilevers shift the isolation peak in *K*-band. A peak value of 47.50 dB has been obtained at 16 GHz.
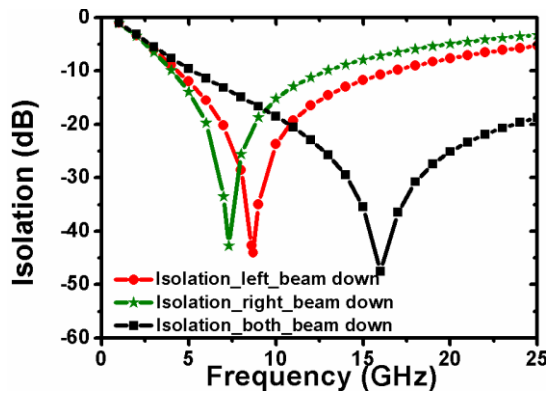
Figure 4.23: Isolation of the switch.   Figure 4.24: Return loss of the switch.
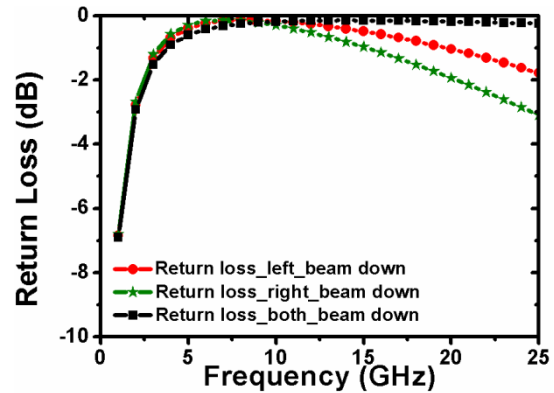
Return loss during OFF-state for the device has been shown in Fig. 4.24. Return loss is minimum when isolation peak value is observed. In electromechanical response, pull-in voltage is determined by doing FEM simulation. The left cantilever has pull-in voltage of 3.25 V, whereas right cantilever has a 4 V as shown in Fig. 4.25.
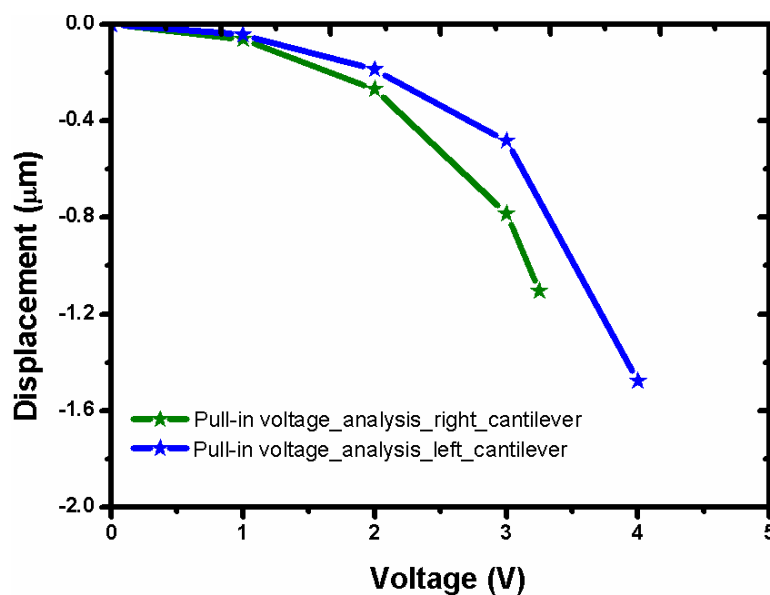
Figure 4.25: Pull-in voltage analysis of the switch.

The asymmetric structure based capacitive shunt RF-MEMS switch has been proposed and investigated. The insertion loss has been improved by utilizing the float metal concept. Isolation peaks have been shifted in different bands by varying the down-state inductance through asymmetric structures.

4.5 Series Metal-to-Metal Contact Switch

Series MEMS switches are based on the same principle as the simple mechanical moving switch. The beam moves mechanically when actuated to close the switch. Switch is implemented through a bridge type of structure.
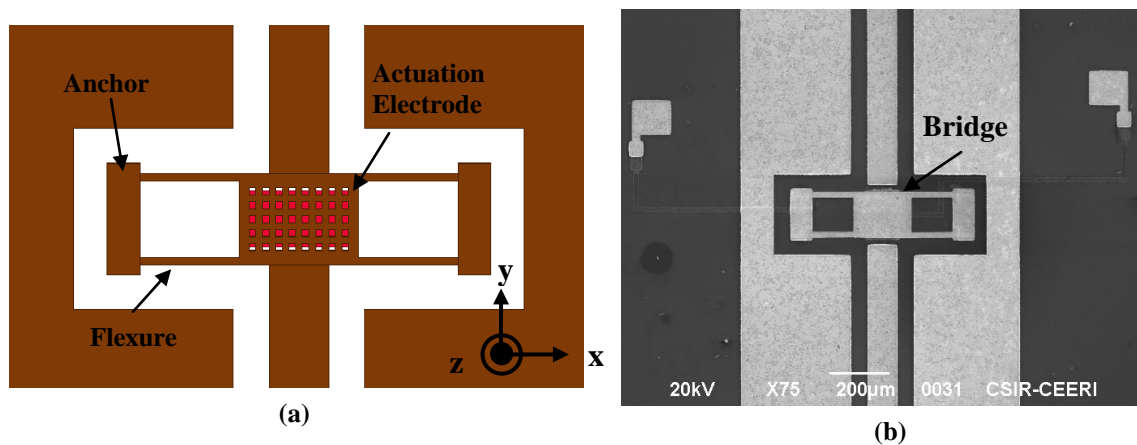
Figure 4.26: (a) Series ohmic RF-MEMS switch (b) SEM micrograph of the fabricated device.

Table 4.5: Dimensions of the designed switch.

Dimension	Value
Length of bridge flexures	150 µm
Width of bridge flexures	10 µm
Thickness of all flexures	1.5 µm
Overlap area between bridge and transmission line	$90 \times 15 \mu m^2$
Central beam area	$180 \times 130 \ \mu m^2$

A uniform bridge structure requires more pull-in voltage so a non-uniform structure has been used to implement the device. Figure 4.26 (a) shows the layout of the switch, whereas Fig. 4.26 (b) shows the SEM image of the fabricated switch. Broadside series ohmic switch of gold material is based on a 50 Ω CPW. As it is a series ohmic switch the

input and output RF ports are physically isolated from each other. The switch is therefore normally in the OFF-state. Switch is anchored in between the ground planes of CPW. The actuation electrode is placed below the central wider beam of bridge structure to reduce the pull-in voltage. In OFF-state of switch there is a gap of 2 μm between switch and central conductor of CPW. The switch design parameters are listed in Table 4.5.

4.5.1 Electromechanical Design

In mechanical design important parameter is the spring constant of the movable structure. The bridge structure here is modeled as four cantilevers with guided ends. The spring constant for a guided end cantilever [54, 60] is given by the equation (4.35).

$$k = \frac{EWt^3}{L^3} \tag{4.35}$$

where k = spring constant in the z direction, E (80 GPa) = Young's modulus of the beam, W (10 μm) = width of guided beam, t (1.5μm) = thickness of guided beam, L (150 μm) = length of guided beam. The equivalent spring constant of the structure with four beams is K = 3.2 N/m.

Under static electromechanical response, Pull-in voltage has been calculated from the equation (3.6), where $A = 180 \times 80$ μm^2, V = applied voltage and d = 2.7 μm, 2.2 μm and 1.7 μm. Figure 4.27 shows the simulated result of the pull-in voltage for the switch.
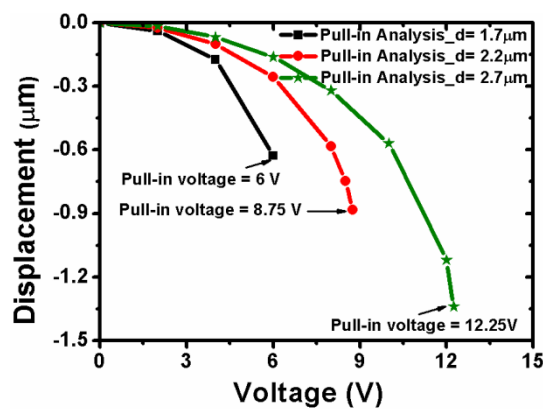
Figure 4.27: Pull-in voltage analysis.
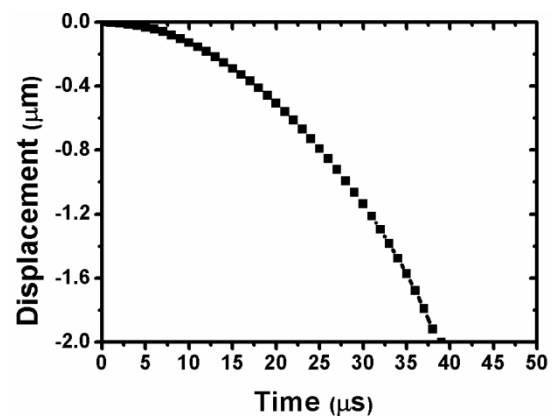
Figure 4.28: Pull-in time analysis.

Pull-in voltages calculated from the analytical expression are 12 V, 8.8 V and 5.9 V at $d = 2.7$ μm, 2.2 μm and 1.7 μm respectively. In dynamic response, FEM simulated pull-in time analysis has been shown in Fig. 4.28. Switch has pull-in time of 39 μs.

4.5.2 RF Response

A. ON-state Response

ON-state S-parameters of the switch i.e. insertion loss and return loss are plotted in Fig. 4.29. Insertion loss of 0.01-0.05 dB has been observed in the frequency range of 1 GHz to 15 GHz as shown in Fig. 4.29 (a). Device shows return loss of 48.02-28.32 dB in the frequency range of 1 GHz to 15 GHz as shown in Fig. 4.29 (b).

(a)

(b)
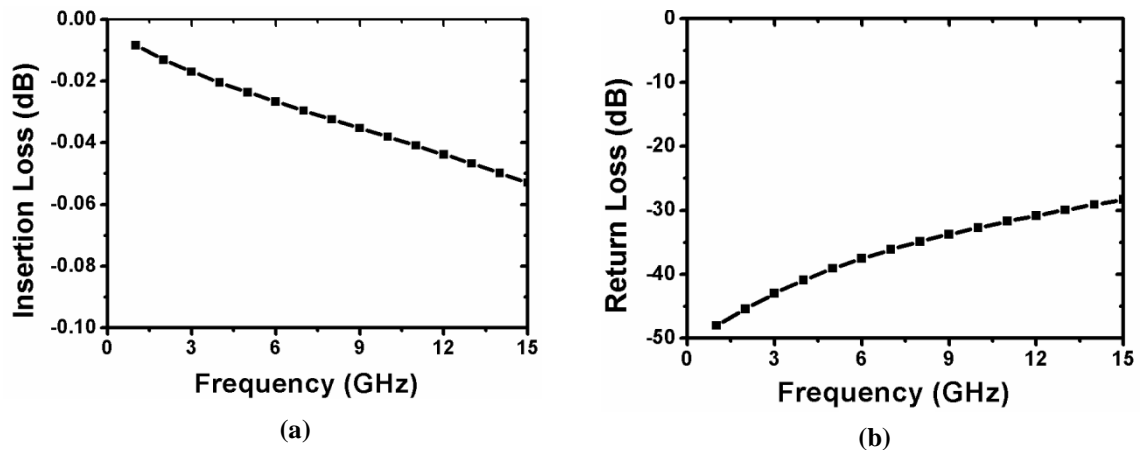
Figure 4.29: ON-state response of the switch (a) Insertion loss (b) Return loss.

(a)

(b)
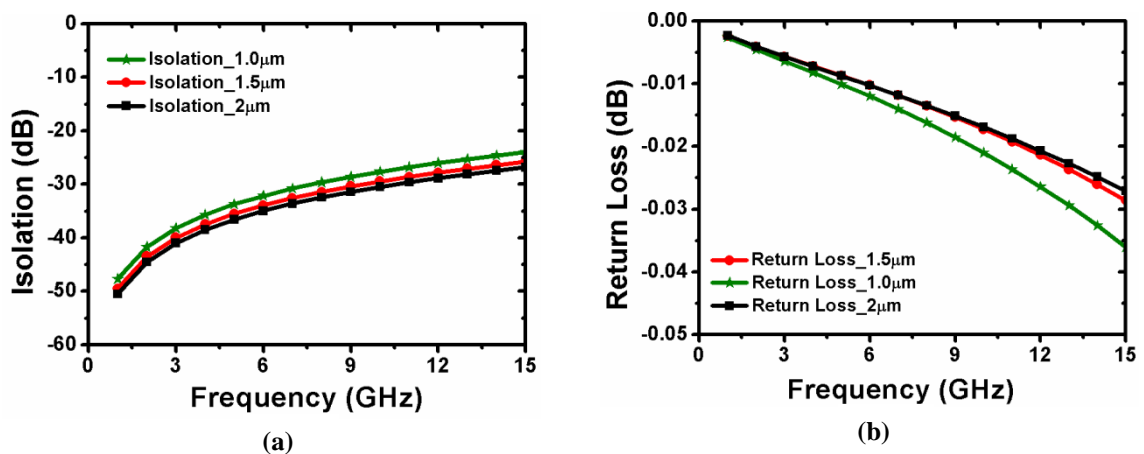
Fig. 4.30 OFF-state response of the switch (a) Isolation (b) Return loss.

B. OFF-state Response

In OFF-state isolation and return loss are plotted in Fig. 4.30. Isolation of 50.52-26.82 dB has been observed in the frequency range of 1 GHz to 15 GHz at $g = 2$ μm as shown in Fig. 4.30 (a). Further, as 'g' is decreased from 2 μm to 1 μm device isolation becomes poor. This has happened due to increase in the up-state capacitance value. Switch return loss response has been shown in the Fig. 4.30 (b).

4.6 Series-Shunt Switch

This section presents a series combination of metal-to-metal contact and capacitive RF-MEMS switches for multi-band wireless applications [83]. However, this approach has poor ON-state response because of the combined effect of two switches. We have presented an improved design for the series-shunt device. The insertion loss and isolation characteristics have been improved through a novel asymmetric structure based capacitive RF-MEMS switch [84].
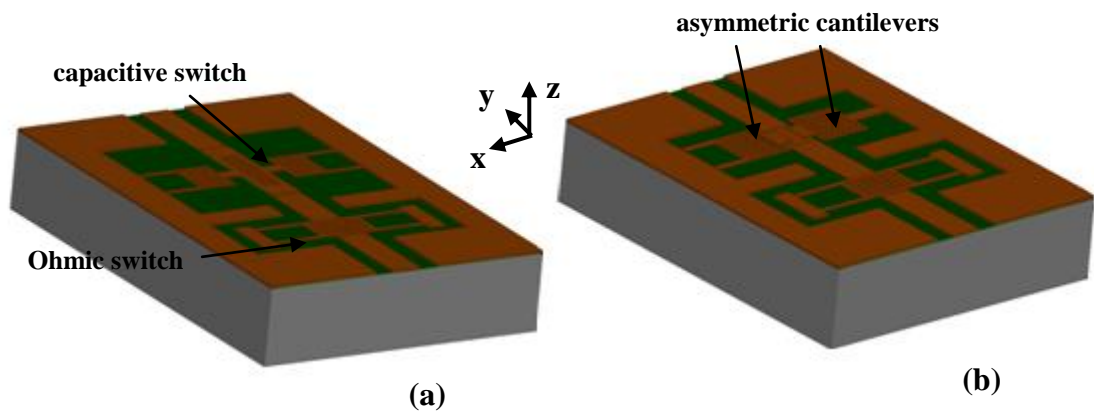
Figure 4.31: Series-shunt switch (a) Conventional (b) Proposed.

A shunt switch with conventional approach is also being designed for comparing the performance. Figure 4.31 shows the model of the device with the proposed and conventional approach. The switches are based on a 50 Ω CPW line. The overlap area between the free end of cantilevers and central conductor of CPW form two capacitors in the up-state. In order to realize the multi-band functionality, inductance value has been kept different on either side cantilevers through asymmetric structures. The switch provides high isolation when the series switch is in the up-state and the shunt switch is in the down-state. The switch provides low return loss when the series switch is in the

down-state and the shunt switch is in the up-state. The fabrication processes for the two switches are compatible.

4.6.1 Working of Device

The configuration based on series ohmic switch cascaded with a conventional capacitive switch can work in three different states. With ohmic switch in the down-state and capacitive in the up-state corresponds to the ON-state. The device shows isolation in the unactuated position. The optimum isolation in the OFF-state is shifted to the C-band by actuating the capacitive switch to the down-state. The device with the novel asymmetric structure based capacitive switch has two additional OFF-states as compared to the conventional design. The extra states are due to the cantilever based structure on the either side of the transmission line.

4.6.2 RF Response

A. ON-state Response

Figures 4.32 and 4.33 show the ON-state response of both devices. The considerable improvement has been achieved in insertion loss and return loss characteristics as compared to the device with conventional approach based capacitive switch. This is due to the reduced capacitance value in the up-state of the cantilever based capacitive switch.

$$C_{up\_con} = \frac{\varepsilon_o A_{up\_con}}{g} = 149.85 \, fF \tag{4.36}$$

$$C_{up\_net\_pro} = C_{up\_Pro\_L} \, || \, C_{up\_Pro\_R} = 15.75 \, fF \tag{4.37}$$

$$\frac{C_{up\_net\_Pro}}{C_{up\_con}} \approx \frac{1}{10} \tag{4.38}$$

Equations (4.36) and (4.37) show the overall up-state capacitance value of the conventional approach based and proposed switch respectively. Equation (4.38) shows that $C_{up\_net\_Pro}$ is around 10 times less than the $C_{up\_Con.}$ The insertion loss has also been improved as the transmission line length has been reduced by 225 μm in case of asymmetric design. Further, this reduction leads to about 17.5 % device area as compared to the conventional device. Insertion loss of 0.01-0.35 dB and 0.01-1.64 dB have been observed in the case of proposed and conventional devices respectively for the

frequency range from dc to 30 GHz as shown in Fig. 4.32. Return loss is below 13.96 dB and 6.14 dB for the novel device and conventional design respectively up to 30 GHz as shown in Fig. 4.33.
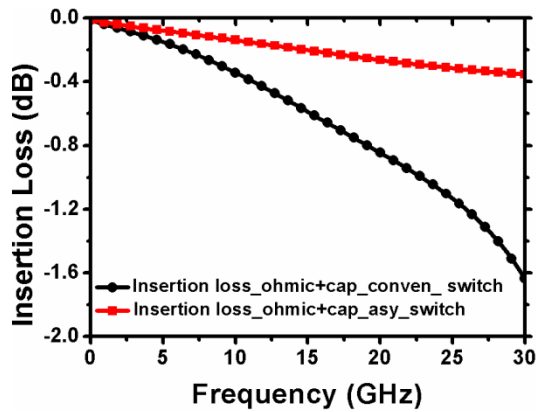
Figure 4.32: Insertion loss of the both devices. Figure 4.33: Return loss of the both devices.
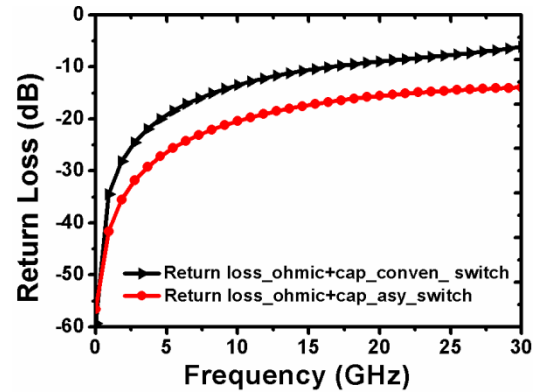
B. OFF-state Response

Figure 4.34 shows the isolation characteristics of both devices. Isolation peaks of 76.01, 76.99 dB have been observed at 8.0, 6.9 GHz when left and right cantilever actuated to the down-state respectively.

(a) (b)
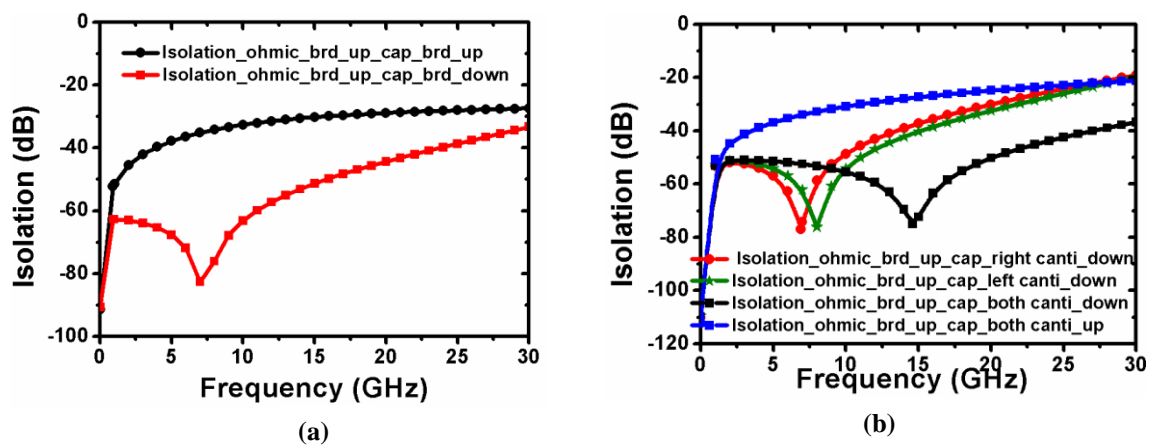
Figure 4.34: Isolation of the series-shunt switch (a) With conventional capacitive switch (b) With asymmetric capacitive switch.

As resonant frequency is the function of the capacitance and inductance, pulling down the both cantilevers shift the isolation peak in *K*-band. A peak value of 74.98 dB has been observed at 14.6 GHz, whereas conventional device has peak only at 7.3 GHz.

C. Switch Bandwidth

The series-shunt device bandwidth can be calculated from the upper operating frequency. The upper frequency (f_U) is limited by the maximum insertion loss or by minimum isolation. For bandwidth calculation an acceptable maximum insertion loss of 0.4 dB and minimum isolation of 30 dB has been chosen.
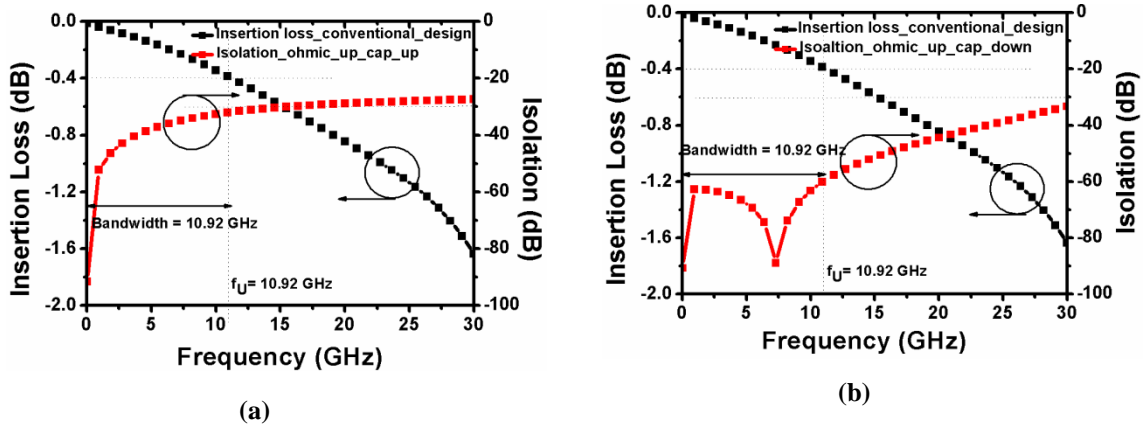
Figure 4.35: Bandwidth of the device (a) Switches are in unactuated state (b) Ohmic device in up-state and capacitive device in down-state.
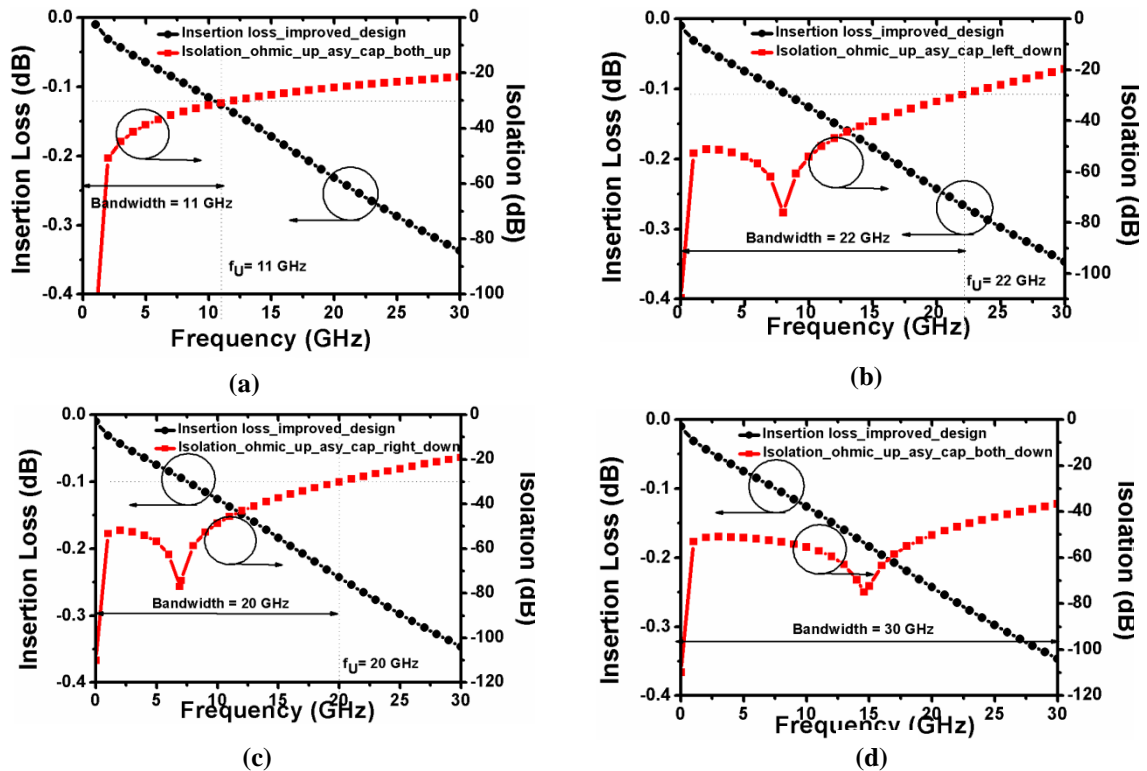
Figure 4.36: Bandwidth of the device (a) Switches are in unactuated state (b) Ohmic switch in up-state and asymmetric capacitive (left cantilever to the down-state) (c) Ohmic switch in up-state and asymmetric capacitive (right cantilever to down-state) (d) Ohmic switch in up-state and asymmetric capacitive (both cantilevers to down-state).

It is observed from the Figs. 4.35 (a) and (b) that upper operating frequency is limited by insertion loss. The device with the conventional capacitive switch can operate from dc to 10.92 GHz. Figure 4.36 (a) shows the bandwidth of the proposed device when both switches are in their unactuated state. The device has the upper cut-off frequency of 11 GHz. In case of ohmic switch is in up-state and left cantilever is actuated to down-state, the device has a bandwidth of 22 GHz as shown in Fig. 4.36 (b). With right cantilever to the down-state, device can work till 20 GHz as shown in Fig. 4.36 (c). Finally, with both cantilevers to the down-state, the device can operate till 30 GHz as shown in Fig. 4.36 (d). Thus, the proposed device has around 3 times more bandwidth as compared to the conventional design. Figure 4.37 shows the simulated pull-in voltage of the conventional capacitive switch, asymmetric capacitive and the ohmic switch.
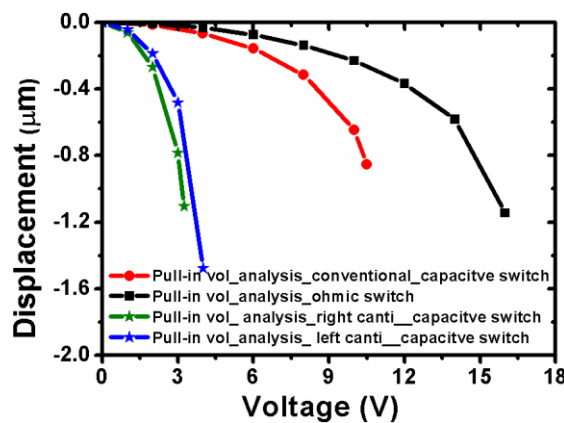
Figure 4.37: Pull-in voltage analysis of the switches.

The series-shunt switch using a new type of capacitive shunt RF-MEMS switch has been designed and investigated. Significant improvement in insertion loss has been observed as compared to conventional approach. The resonant peaks during OFF-state response are tuned to a different frequency band for achieving frequency reconfigurability. Further, a reduction of about 60 % in the pull-in voltage of capacitive switch and 17.5 % in device area have also been observed. The device can be used in the frequency range from dc to 30 GHz.

4.7 Comparison and Conclusion

Table 4.6 gives a comparison of the switches presented in the chapters 3 and 4 with the literature work. All the switches are designed for *X*-band applications. The devices discussed in [16, 74, 76] have a high insertion loss, whereas in [68] has higher pull-in

voltage. In case of switches discussed in this thesis, the device designed in section 3.3 have high insertion loss and moderate pull-in voltage.

Table 4.6: Comparison of published SPST RF-MEMS Switches with the thesis work.

S.No	RF-MEMS Capacitive Shunt Switch	Frequency (GHz)	Isolation Optimum Value (dB)	Insertion Loss (dB)	Pull-in Voltage (V)	Multi-band Reconfigurablity
1	Ref. [16]	10	35	0.25	9.5	No
2	Ref. [74]	10	35	0.2	-	No
3	Ref. [68]	9.5	43	≈ 0.08	20	No
4	Ref. [76]	11	47	0.45	20	No
5.	Switch [section 3.3]	10.1	54.24	0.2	12.75	No
6.	Switch [section 3.4]	10.1	54.90	0.05	11.75	No
7.	Switch [section 3.5]	9	52.72	0.06 @ g = 2 µm 0.09 @ g= 1 µm	12 @ g = 2 µm 5.5 @ g= 1 µm	No
8.	Switch [section 4.2]	10.4 11 21.4	34.71 34.33 40.67	0.05 0.06 0.09	Bridge = 12.25, Cantilever = 7.5	Yes
9.	Switch [section 4.3]	9.7 4.5	54.56 48.80	0.05 0.03	6	Yes
10.	Switch [section 4.4]	8.7 7.3 16	43.98 42.72 47.50	0.05 0.04 0.07	4 3.25	Yes

In section 3.4, the device ON-state response has been improved , but pull-in voltage was still at higher side (11.75 V). In contrast, for high-*k* dielectric based design, the pull-in voltage has been reduced up to 5.5 V by reducing the initial gap between transmission line and hanging structure. But, none of the switches discussed so far have the multi-band reconfigurablity. In section 4.2, a novel approach has been presented for tuning the isolation optimum value to different frequency bands. Switch design involves both i.e. bridge and cantilever structures with moderate to low pull-in voltage. The proposed device shows the narrow isolation response as higher inductance was involved in the design. For improving the isolation response and reducing the pull-in voltage with multi-band reconfigurablity feature, two designs based on non-uniform cantilever structures have been designed and investigated in section 4.3 and 4.4. The designs utilize the structural changes of switch (from bridge to cantilever) for reduction of spring constant, which results in decrease of pull-in volatge.

Chapter - 5

Realization of RF-MEMS SPDT Switches

5.1 Introduction

Chapters 3 and 4 discussed the various structures for RF-MEMS technology based SPST switches. The SPST is the key component of the RF-MEMS technology and serving as building block for the more complex sub-systems. This chapter uses MEMS switches to implement a SPDT device for wireless systems. The SPDT consists of two shunt capacitive RF-MEMS switches. This chapter also discusses multi-band reconfigurable SPDT based on shunt capacitive switch.

5.2 SPDT Design

5.2.1 Introduction and Working Principle

As the name suggests, SPDT route signals from one input to two output paths selectively. SPDT is used at various places in a wireless communication system such as selecting receive or transmit channels in T/R modules, routing the RF signals through various filter banks for wideband coverage, switchable antennas and for achieving the redundant character for secured space applications [26, 27, 85, 86]. Figure 5.1 shows the simplified circuit model to demonstrate the working principle of the SPDT device. All the transmission lines are of 50 Ω. The shunt capacitive contact switches have been used on the either branch of the output ports. As the capacitive switches present the RF virtual short circuit on the central conductor of CPW at the operating frequency in the down-state, the transmission lines of the output ports branches have an electrical length of $\lambda_{g/4}$. This has been done in order to transfer the RF virtual short circuit to a virtual open circuit to the T-junction and to transfer the RF signal from one of the output ports selectively [87, 88].

In this thesis, SPDT has been designed using two different types of capacitive switches. The first design is based on the conventional capacitive switch, whereas second design uses a cantilever structure based capacitive switch.
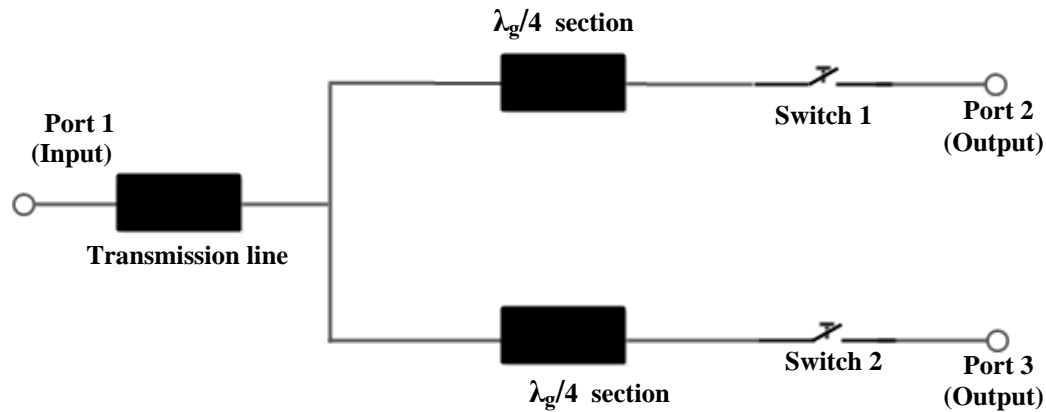
Figure 5.1: Simplified representation of the SPDT device.

5.2.2 SPDT Based on Conventional Capacitive Switch

Figure 5.2 shows the design of SPDT for *X*-band applications. The SPDT consists of a T-junction with a switch at each of the output arms. The MEMS switch utilized in the SPDT device is based on the non-uniform bridge. This device has already been discussed in the section 3.3. The switch is placed a distance of 2953μm from the T-junction which corresponds to $\lambda_{g/4}$ at 10 GHz. For the SPDT working, the switch corresponding to output port 1 is assumed in the down-state or the actuated state, whereas switch in the output port 2 is in the up-state. This assumption has been followed throughout the study in order to avoid confliction.
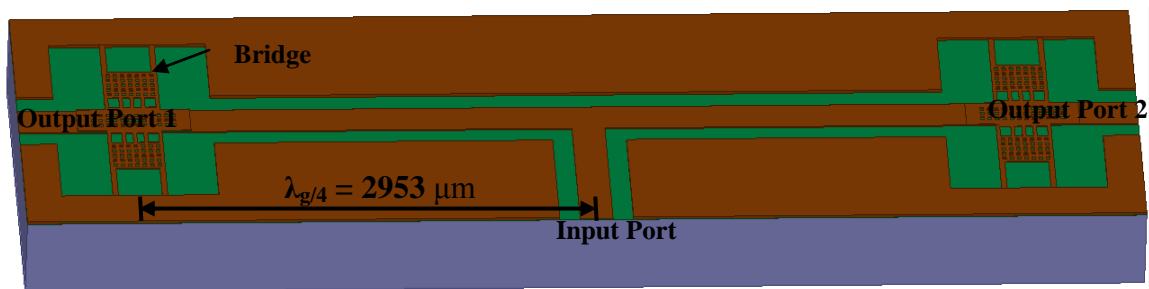
Figure 5.2: SPDT based on conventional capacitive switch.

A. RF Response

The simulated RF response of the SPDT has been shown in the Figs. 5.3-5.5. SPDT shows the insertion loss better than 0.5 dB in the frequency range from 10.4 GHz to 12.3 GHz as shown in the Fig. 5.3.
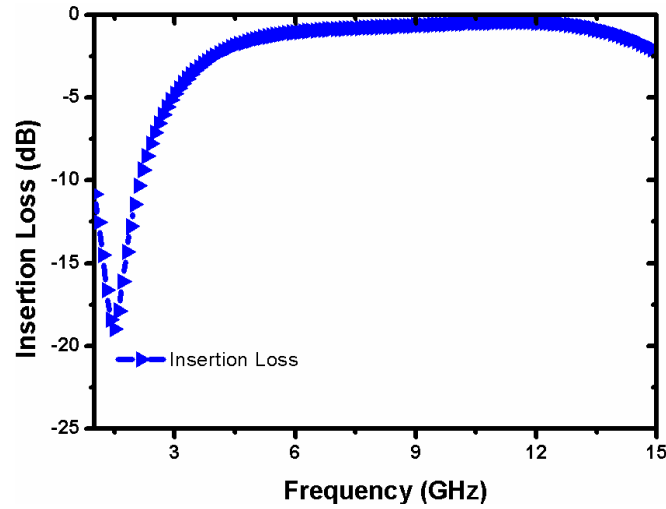
Figure 5.3: Insertion loss of *X*-band SPDT.
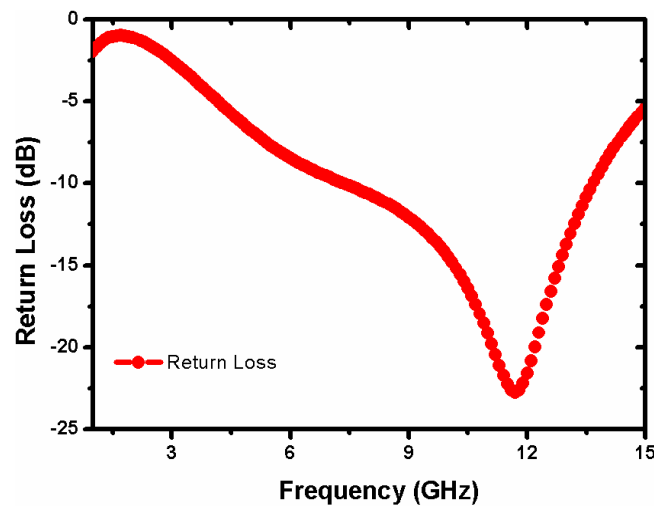
Figure 5.4: Return loss of *X*-band SPDT.

The plot in the Fig. 5.4 shows the return loss response of the SPDT. Return loss is better than 15 dB in the 10.2 GHz to 12.8 GHz. Further, Isolation is better than 20 dB in the frequency range from 4.1 GHz to 15 GHz as depicted in the Fig. 5.5.

B. Bandwidth

The SPDT bandwidth is calculated from the lower (f_L) and upper (f_U) operating frequencies with some acceptable maximum insertion loss, minimum isolation and return loss values. For bandwidth calculation an acceptable maximum insertion loss of 0.5 dB, minimum isolation of 20 dB and 15 dB of return loss has been chosen. The SPDT has f_L = 10.4 GHz and f_U = 12.3 GHz. The lower bound and upper bound frequencies are limited by the maximum insertion loss.
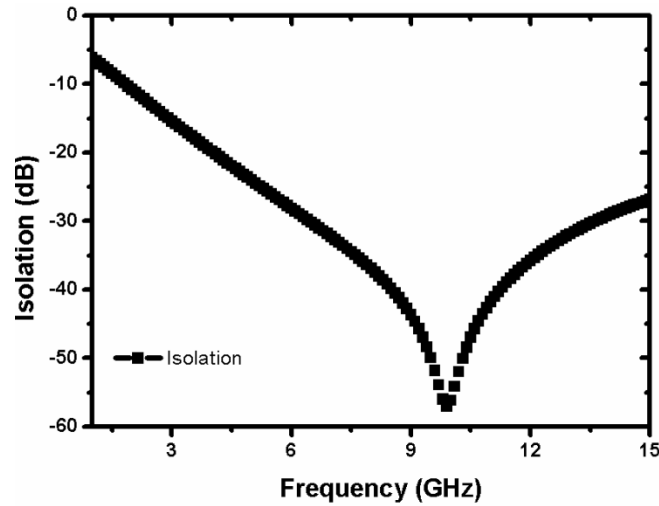
Figure 5.5: Isolation of *X*-band SPDT.
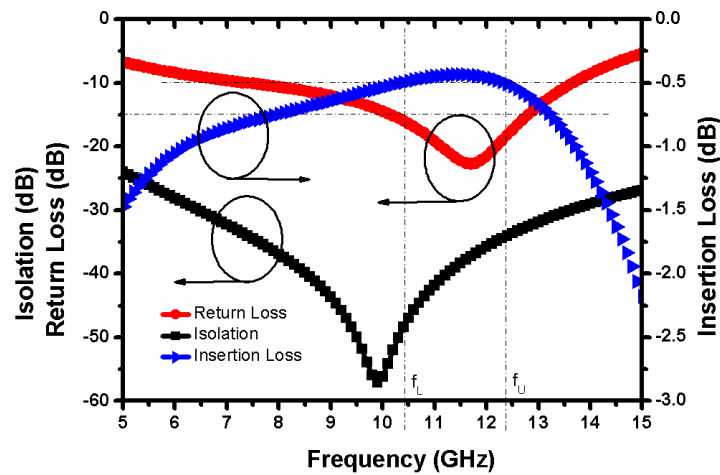
Figure 5.6: Bandwidth of the SPDT.

5.2.3 SPDT Implementation Using Cantilever Based Shunt Capacitive Switch

For improving the ON-state RF response, bridge based capacitive switch has been replaced with the cantilever based capacitive switch. Figure 5.7 shows the design of the SPDT device using cantilever based switches at each of the output arms. The device response has already been covered in the chapter 4. The switches are placed a distance of 2953 μm as in case of bridge structure based design from the T-junction which corresponds to $\lambda_{g/4}$ at 10 GHz.
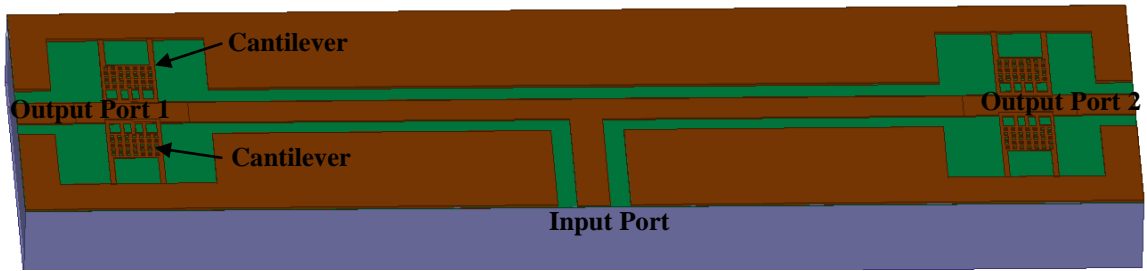
Figure 5.7: Design of SPDT using cantilever based switch.

A. RF Response

The insertion loss ≤ 0.5 dB has been observed in the frequency range from 7.9 GHz to 12.3 GHz as shown in the Fig. 5.8. Figure 5.9 shows the return loss response of the SPDT. Return loss is better than 15 dB in the frequency range of 8 GHz to 12.5 GHz. Further, Isolation is better than 20 dB in the frequency range from 4 GHz to 15 GHz as depicted in the Fig. 5.10.
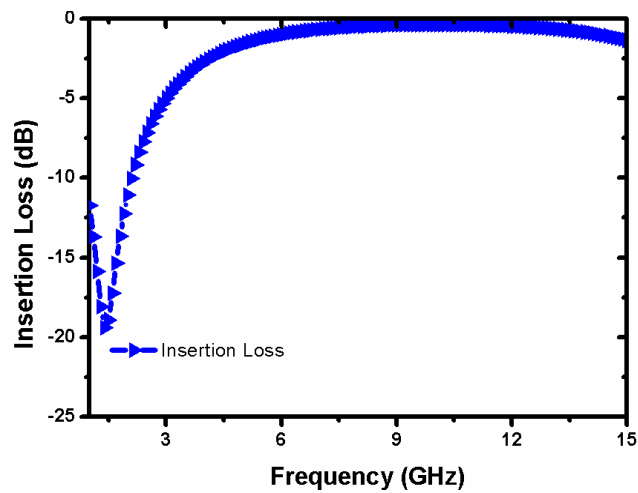
Figure 5.8: Insertion loss of SPDT.
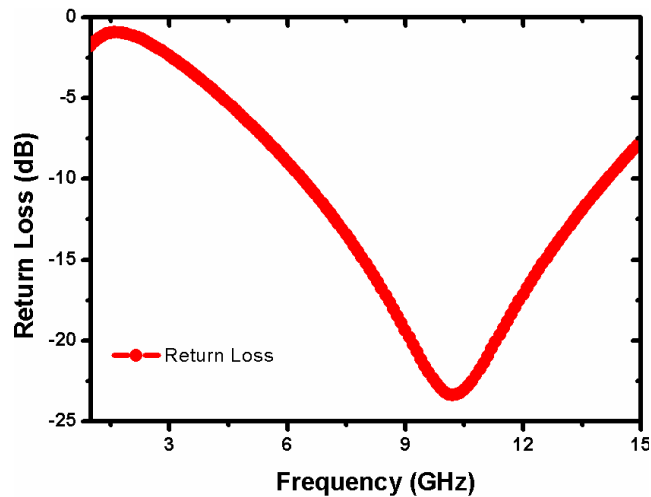
Figure 5.9: Return loss of SPDT.
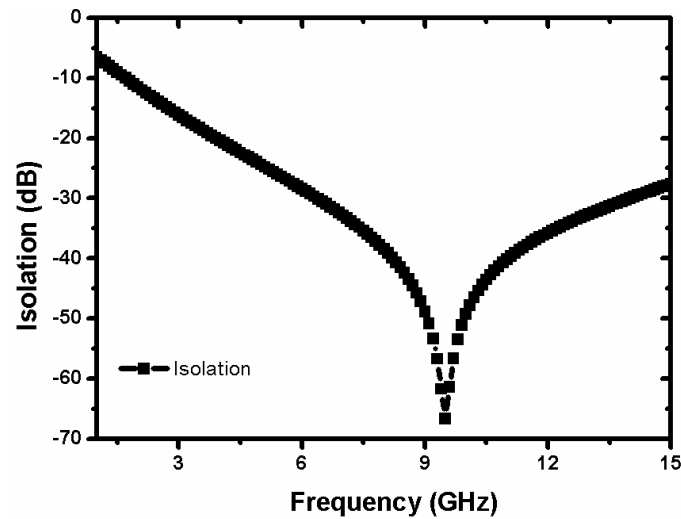
Figure 5.10: Isolation of SPDT.

B. SPDT Bandwidth

The SPDT has f_L = 8 GHz and f_U = 12.3 GHz, which results in a bandwidth of 4.3 GHz in the X-band as shown in the Fig. 5.11. Thus, bandwidth is almost doubled in the cantilever based SPDT as compared to the conventional bridge based device. The lower bound frequency is limited by return loss, whereas upper bound frequency is limited by the maximum insertion loss.
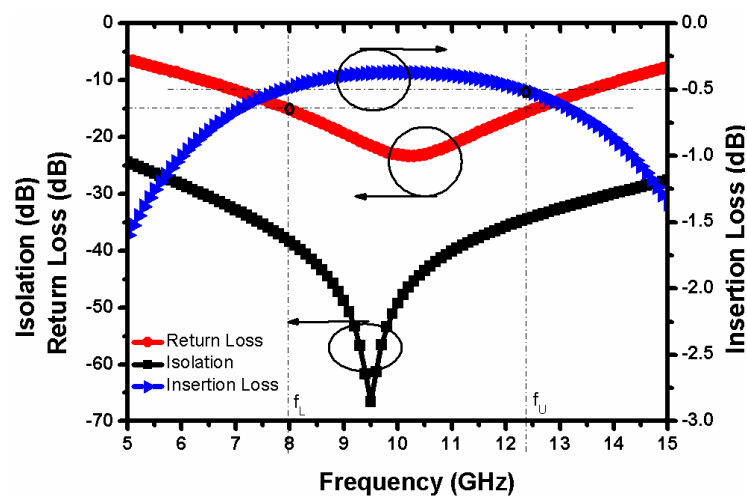
Figure 5.11: Bandwidth of SPDT.

C. Effect of Air-Bridge on SPDT Design

The air-bridges are disposed in the vicinity of the CPW T-junction so as to avoid the propagation of the undesired modes and to reduce the length of the line as result of change the propagation velocity of the signal as shown in Fig. 5.12 [64, 89].
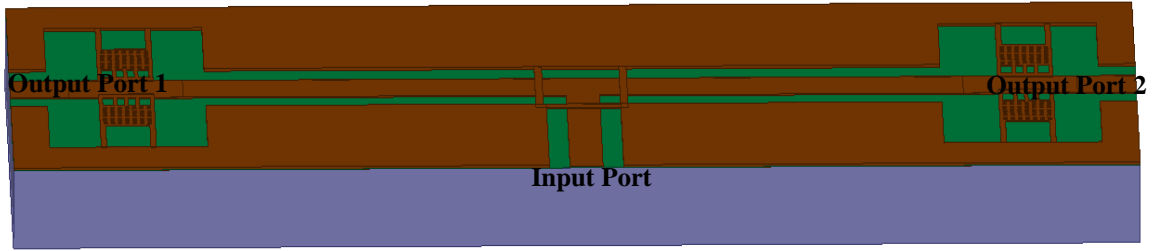
Figure 5.12: Model of SPDT using cantilever based switch with air-bridge.
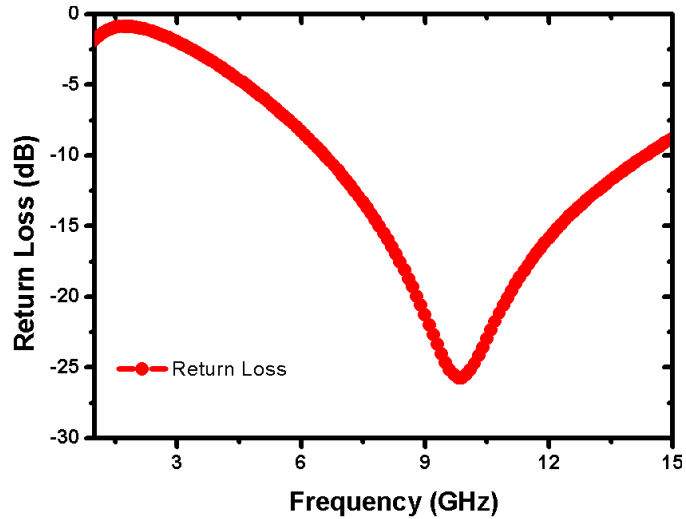
Figure 5.13: Return loss of SPDT with air-bridge.

The width of the air-bridge is set to 20 μm so as to avoid the actuation with the power that will pass through the central conductor. The SPDT with air-bridges is around 11 % more compact in size as compared to the SPDT without air-bridges.
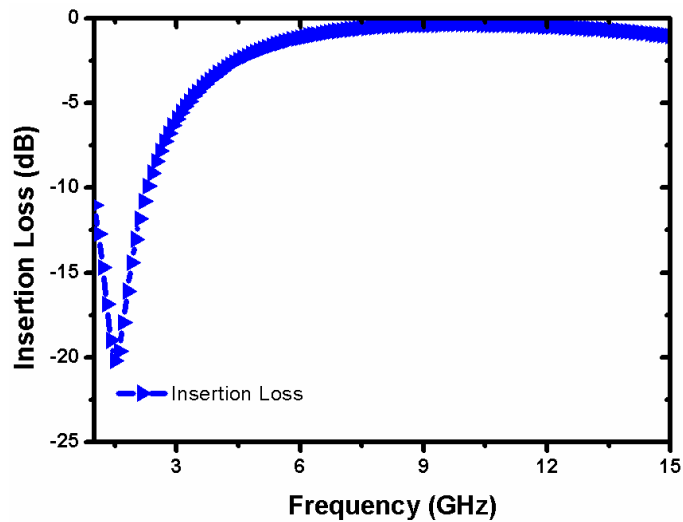
Figure 5.14: Insertion loss of SPDT with air-bridge.
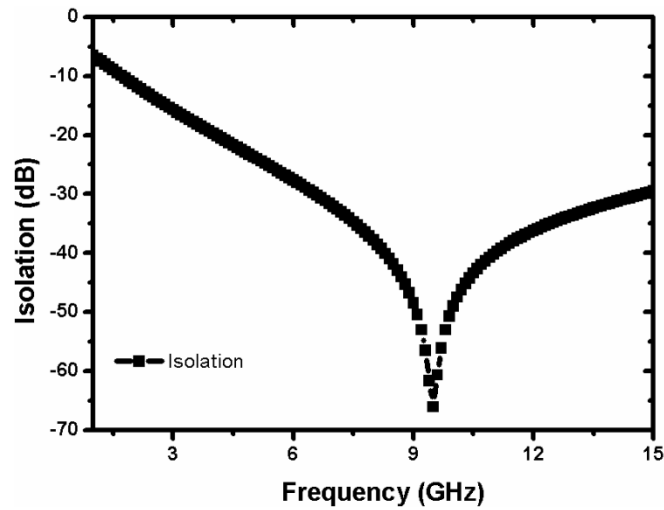
Figure 5.15: Isolation of SPDT with air-bridge.
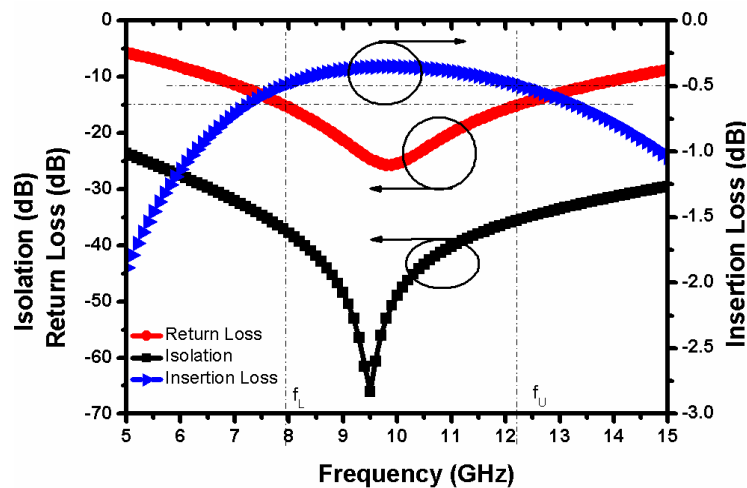
Figure 5.16: Bandwidth of SPDT with air-bridge.

A maximum input matching of 25.71 dB is achieved at 9.8 GHz and is less than 15 dB in the frequency range from 7.9 GHz to 12.2 GHz as shown in the Fig. 5.13 and the insertion loss is less than 0.5 dB in the same range (Fig. 5.14). However, both SPDT have the same bandwidth of 4.3 GHz in the *X*-band as shown in the Figs. 5.11 and 5.16.

5.2.4 Reconfigurable Multi-band SPDT

In this section, a reconfigurable multi-band SPDT has been designed and investigated. Figure 5.17 shows the model of SPDT switching device that can work in four different frequency bands i.e. *S, C, K$_u$* and *K*. The switches are placed a distance of 6260 μm from the T-junction which corresponds to $\lambda_{g/4}$ at 4.5 GHz with air-bridges. SPDT has two different operational states. In state 1, either cantilever of the device corresponding to the output port 1 is switched to the down-state, whereas switch in the output port 2 is in the

up-state. In this state, SPDT can work at the *S* and *C* bands. In state 2, both cantilevers of the device corresponding to the output port 1 is switched to the down-state, whereas switch in the output port 2 is in the up-state. In this state, SPDT can work at the K_u and K bands.
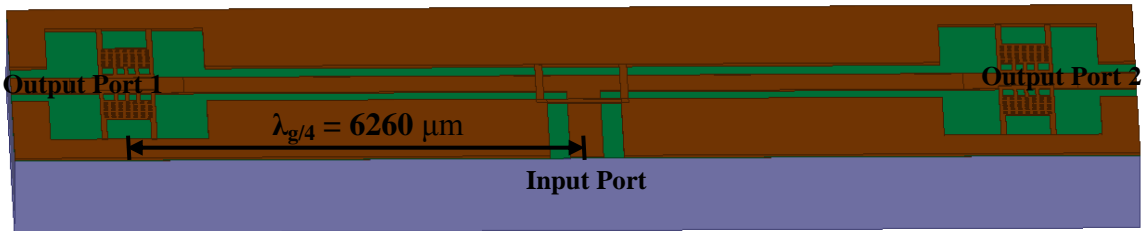
Figure 5.17: Model of reconfigurable multi-band SPDT.

A. RF Response

In state 1, SPDT is designed to work at 4.5 GHz. The SPDT has insertion loss, return loss and isolation of 0.49 dB, 21.74 dB and 51.73 dB respectively at 4.5 GHz.
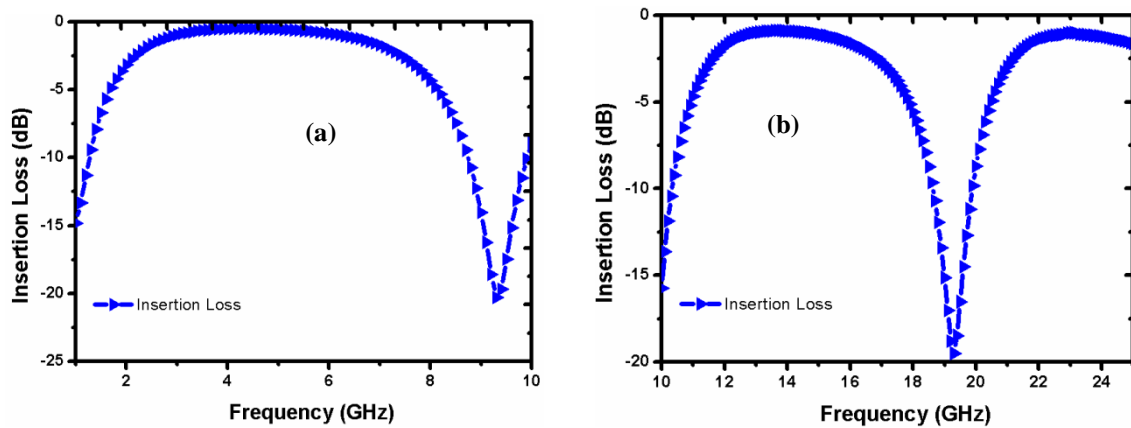
Figure 5.18: Insertion loss of SPDT (a) With either cantilever to the down-state (b) With both cantilevers to the down-state.
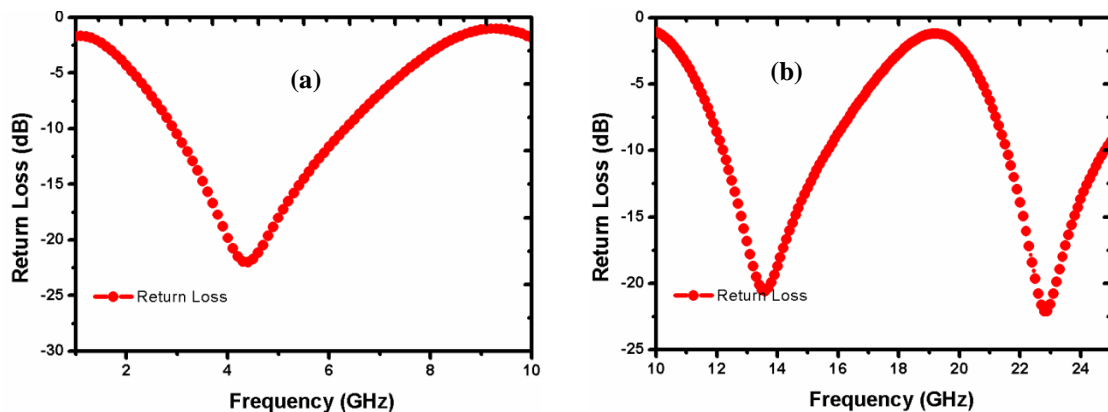
Figure 5.19: Return loss of SPDT (a) With either cantilever to the down-state (b) With both cantilevers to the down-state.

Furthermore, the insertion loss is less than 1 dB at 3-6.2 GHz as shown in the Fig. 5.18 (a). Figure 5.18 (b) shows the insertion loss response for state 2. The insertion loss ≤ 1 dB is observed at 12.9-14.6 GHz and 22.9 to 23.2 GHz. The return loss is better than 15 dB at 3.6-5.4 GHz for state 1 and for state 2 at 12.9-14.5 GHz, 22.2-23.7 GHz as shown in the Figs. 5.19 (a) and (b) respectively. The isolation is better than 20 dB at 2.7-7.4 GHz and 10-25 GHz as depicted in the Figs. 5.20 (a) and (b) respectively.
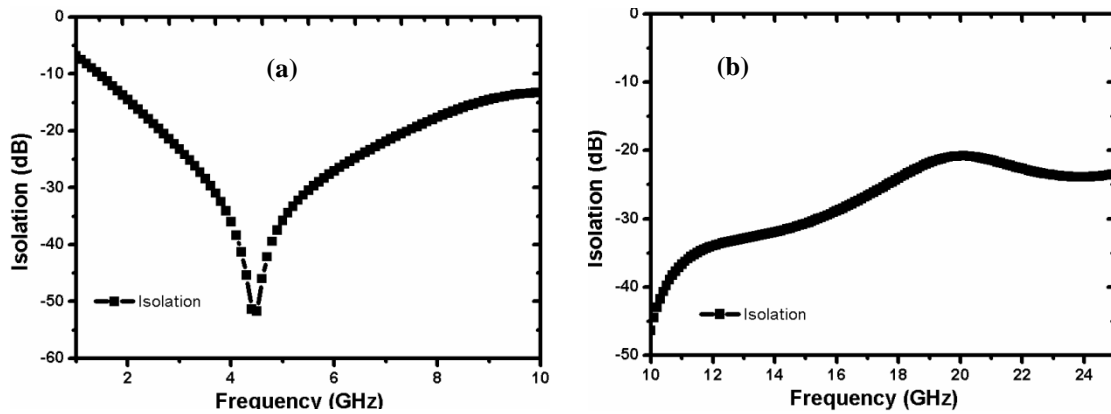
Figure 5.20: Isolation of SPDT (a) With either cantilever to the down-state (b) With both cantilevers to the down-state.

B. Bandwidth

For bandwidth calculation maximum insertion loss of 1 dB, minimum isolation of 20 dB and 15 dB of return loss has been chosen. Under state1, the SPDT has $f_L = 3.6$ GHz and $f_U = 5.4$ GHz and thus the bandwidth of 1.8 GHz in S and C bands. The lower bound and upper bound frequencies are limited by the minimum return loss as shown in the Fig. 5.21 (a).
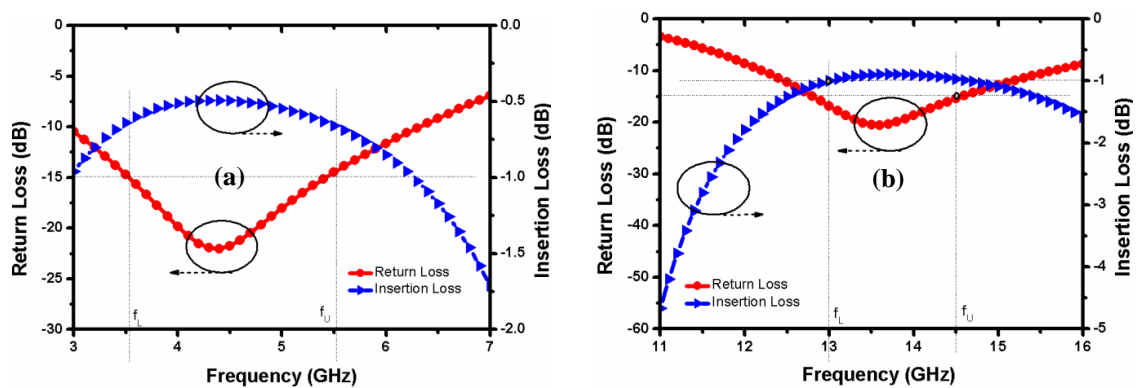
Figure 5.21: Bandwidth of SPDT (a) With either cantilever to the down-state (b) With both cantilevers to the down-state.
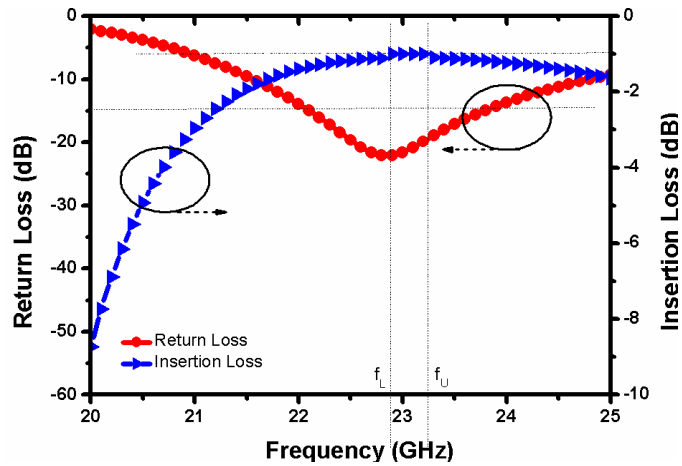
Figure 5.22: Bandwidth of SPDT with both cantilevers to the down-state.

Under state 2, the SPDT can work in K_u and K bands. In K_u-band, the SPDT has $f_L = 12.9$ GHz and $f_U = 14.5$ GHz and in K-band $f_L = 22.9$ GHz and $f_U = 23.2$ GHz as shown in Fig. 5.21 (b) and Fig. 5.22 respectively.

5.3 Conclusion

SPDT has been designed using two different types of capacitive switches. The considerable improvement in the ON-state response has been seen for the SPDT implemented using cantilever structure based switch as compared to conventional capacitive switch based SPDT. The bandwidth is also increased around 2 times. Further, compactness can be achieved in the SPDT structure with the incorporation of air-bridges in the design. A reconfigurable multi-band SPDT has also been designed and investigated. The SPDT can work in four different bands i.e. S, C, K_u and K.

Chapter - 6

Fabrication and Measurements

6.1 Introduction

This chapter discusses in detail the process flow for the fabrication of RF-MEMS switches. The process flow is based on the steps followed by the CSIR-CEERI, SEM Lab, Pilani for switches fabrication [9, 16]. The fabrication steps and materials for the RF-MEMS switches are compatible with the standard IC technology. Under measurements section, thickness, gap and mechanical resonant frequency have been measured for the switch based on asymmetric cantilever structure.

6.2 Fabrication Steps for RF-MEMS Switches

The process flow for the switches fabrication consists of seven mask levels as given below:

- Thermal oxidation for isolation layer.

- Polysilicon deposition and doping.

- First level lithography to define actuation electrodes in the photoresist and polysilicon patterning using reactive ion etching.

- PECVD silicon oxide deposition.

- Second level lithography to open contact holes in silicon oxide and its patterning using reactive ion etching.

- Sputter deposition of multi-metal layer stack i.e. *Ti/TiN/Al:1%Si/Ti/TiN* forms the underpass area of the switch.

- 3rd level lithography and wet etching to define underpass area.

- PECVD silicon dioxide deposition to define the dielectric layer for central overlap area.

- 4th level lithography to open via holes in oxide and reactive ion etching for oxide patterning.

- 5th level lithography to define the mould for floating metal layer.

- Sputter deposition of *Cr-Au* and lift off of the floating metal layer.

- 6th level lithography to define spacer or sacrificial layer.

- Sputter deposition of seed layer for electroplating.

- 7th lithography to define the mould for electroplating of the suspended bridge using photoresist.

- Au electroplating (1.5 μm thick).

- Seed layer etching (wet chemical etching of *Au-Cr*).

- Release of suspended beam by plasma ashing.

The major process steps described above have been shown through the schematic representation in Fig. 6.1 and described in detail as follows:

- In the present work, all switches are fabricated on a low loss, 2", 5 kΩ-cm, p-type, *Si* <100> wafer. A buffer layer of 1μm of *SiO₂* has been grown using thermal oxidation as shown in the Fig. 6.1 (a).

- In the next step, a polysilicon layer of 0.6 μm is obtained using the low pressure chemical vapor deposition process (Figure 6.1 (b)). Since undoped polysilicon has low electrical conductivity, polysilicon deposition is followed by phosphorus doping to obtain the sheet resistivity of 240 $\Omega/\square$. The first lithography at this stage defines the actuation electrodes and dc bias lines for the switches. The polysilicon dry etching is followed by the resist removal by plasma ashing.

- A layer of 0.3 μm thick *SiO₂* is deposited by pyrolytic oxidation of tetraethylorthosilane (TEOS) using LPCVD. This layer is required in order to prevent the electrical short between the metal bridge and actuation electrodes. The electrical properties of TEOS oxide such as fixed charges and impurities have a strong impact on the reliability of the devices. The presence of impurities and fixed charges coupled with high electric fields across the oxide layer may result in a drift in the pull-in voltage during the subsequent actuation cycles or total device failure.

- The contact holes opened in TEOS, by the second lithography connect the polysilicon actuation electrodes to multi metal pads which are finally connected to the broad and thick gold pads used for probing the devices (Figure 6.1 (c)). Reactive ion etching technique is used to open the contact holes in SiO_2 layer followed by photoresist removal. The next step is to realize the multilayer underpass which joins the two portions of the CPW central conductor under the hanging structure.

- The multi-layer stacks start with the sputter deposition of Ti (30 nm) and TiN (50 nm, reactive sputtering). The layers act as adhesion promoter and diffusion barrier. In the next step, layers of $Al1\%Si$ (450 nm) followed by Ti (30 nm), are deposited by sputtering at room temperature. Finally a smooth capping layer of TiN (80 nm) is sputter deposited. The next lithography step followed by metal dry etch defines the underpass lines and the diffusion barrier (TiN) on the polysilicon contacts (Figure 6.1 (d)).

- The insulation layer on the multilayer metal underpass is provided by the LPCVD low temperature oxide (LTO, 0.1μm). Via holes which connect Al in the multilayer to the gold CPW central conductor are subsequently defined by lithography and dry etching (Figure 6.1 (e)). A sufficient over-etch time is incorporated into the process in order to ensure the removal of TiN barrier layer and exposure of the Al underneath.

- At this stage, the process for devices has an additional layer of metal on top of the LTO, which corresponds to the capacitance area of the shunt switches. Another lithography and etching step is required to define the floating metal area (Figure 6.1 (f)). For conventional shunt switches this step is not required.

- The sacrificial layer used for the construction of the suspended metal structure is defined in this step using thick positive (3 μm) photoresist (Figure 6.1 (g)). As a seed layer for electrochemical Au-deposition, a 10/150 nm thick Cr/Au layer is deposited by PVD.
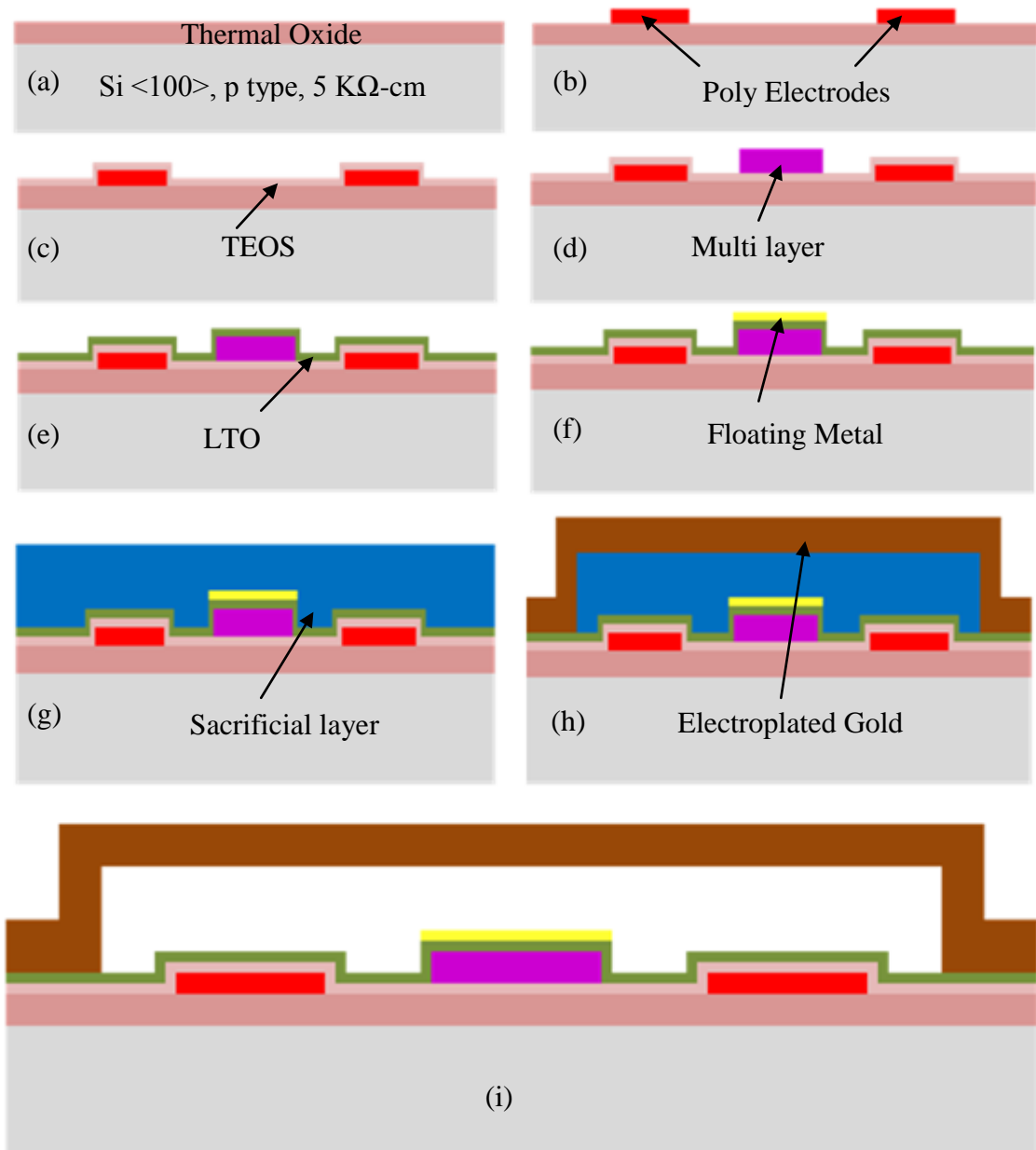
Figure 6.1: Schematic of the major fabrication process flow steps for Capacitive Switch.

- The gold movable structure is realized using electroplating process. The switch is electroplated up to a thickness of 1.5 μm. The bridge is defined on a 4 μm thick photoresist. At this stage, the 3 μm thick spacer layer is already exists. Though the required bridge thickness is only 1.5 μm, thicker resist is used to achieve better step coverage over the spacer area. After the wet removal of the electroplating mask and the seed layers, the CPW lines and anchor posts for the movable structure are defined. Finally, the movable structures are released by ashing of the spacer resist with a plasma ashing process. The dry etch release is

preferred in order to avoid the sticking of the structures to the wafer surface. The whole process consists of about 120-130 steps.

6.3 Measurements

A fabricated capacitive shunt switch based on the asymmetric cantilever structure has been tested for physical and mechanical parameters. The switch layout and SEM image are shown in Fig. 6.2. Figure 6.3 shows the details of the multimetal underpass and floating metal layer.

6.3.1 Thickness and Gap Height Measurements Using 3-D Optical Profiler

Under physical parameters, the thickness of the transmission line and the gap between the hanging structure and the transmission line has been measured. Transmission line thickness and the gap between cantilever and transmission are measured through 3-D optical profiler [90]. Figure 6.4 shows the height difference between the underpass and transmission line. As, the point corresponding to $x = 344.3$ μm, has multimetal stack underneath the transmission line, the resulting thickness of the line is approximately 2.5 μm. Figure 6.5 indicates the gap height of 2.7 μm between the transmission line and cantilever tip. The 3-D optical profiler image of the capacitive switch is shown in Fig. 6.6. The cantilevers show out-of-plane buckling due to the residual stress presents in the micro structure.
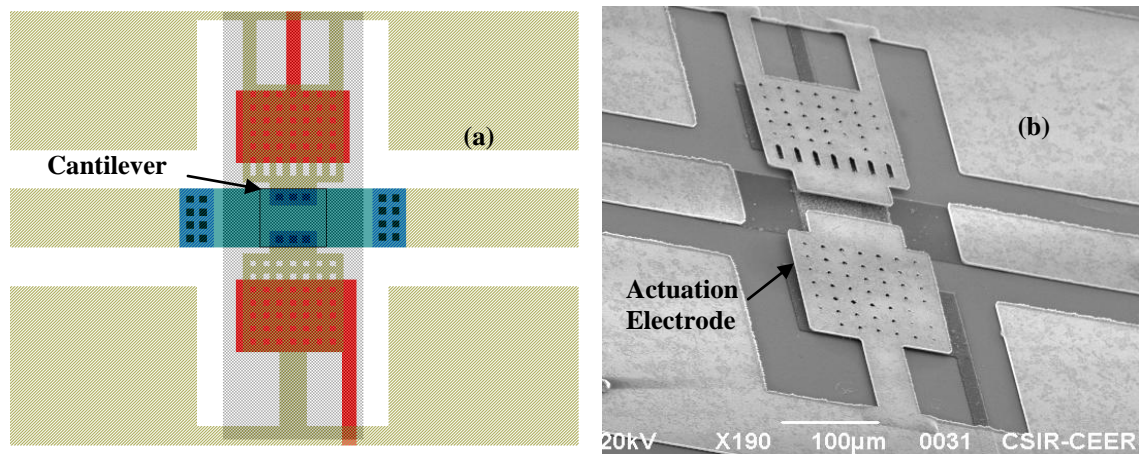
Figure 6.2: Capacitive shunt switch fabricated using CSIR-CEERI technology (a) Complete layout (b) SEM micrograph of fabricated switch.
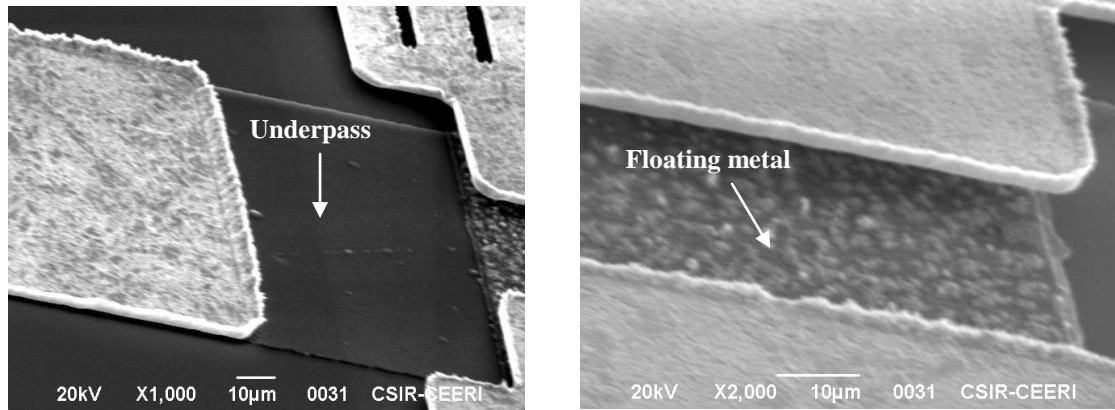
Figure 6.3: (a) Detailed view of the underpass (b) Floating metal.
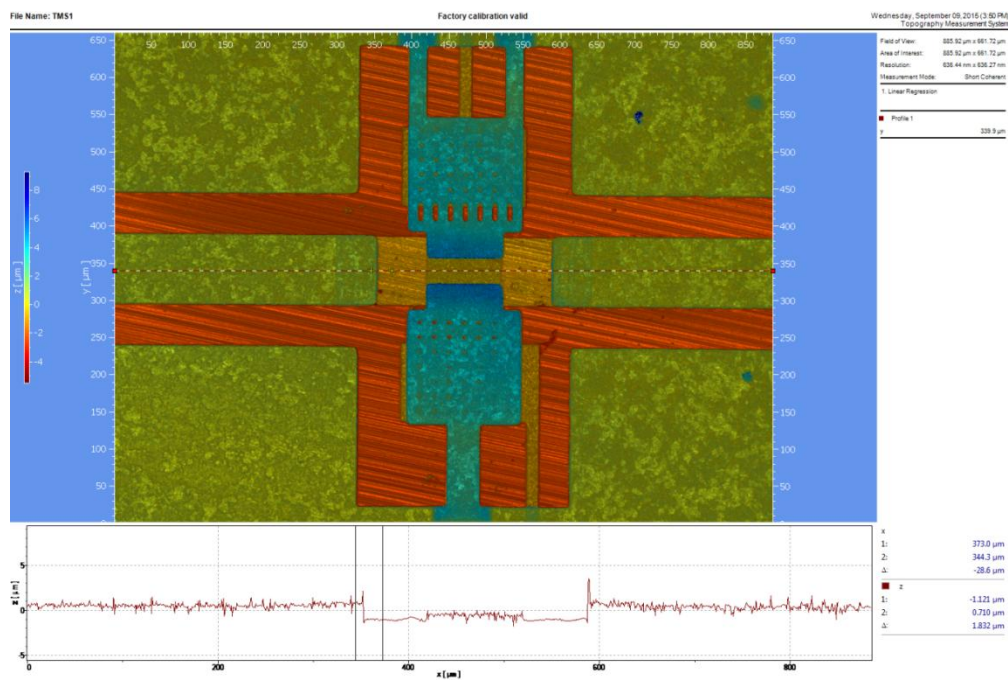
Figure 6.4: 2-D profile and line scan along the transmission line indicating the thickness of approximately 2.5 μm.

6.3.2 Mechanical Resonance Frequency Measurement

The RF-MEMS devices are inherently slow as compared to their solid-state counterparts. The pull-in time depends on angular resonant frequency, pull-in voltage (V_p) and supply voltage (V) as illustrated by equation (6.1). Equation (6.1) gives the improved expression for the pull-in time (t_p), where we have incorporated the gap dependency of the electrostatic force. The expression has been derived in the chapter 3. The release time (t_p) also depends on the angular resonant frequency as given in equation (6.2).
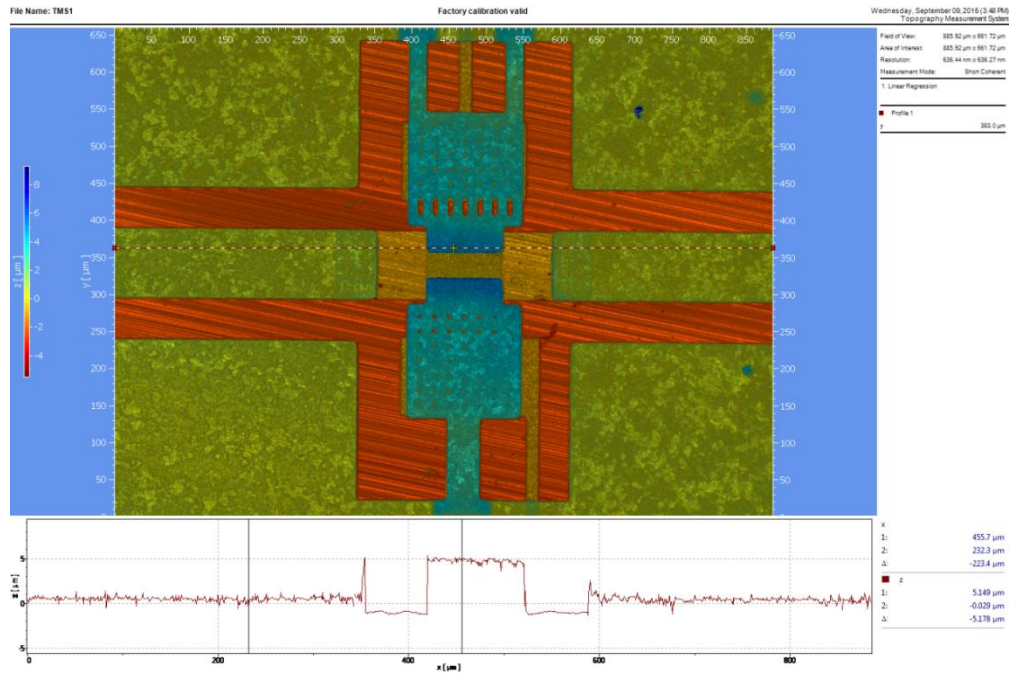
Figure 6.5: Optical 2-D profile of switch and line scan along the transmission line including cantilever indicating a gap height of approximately 2.7 μm.
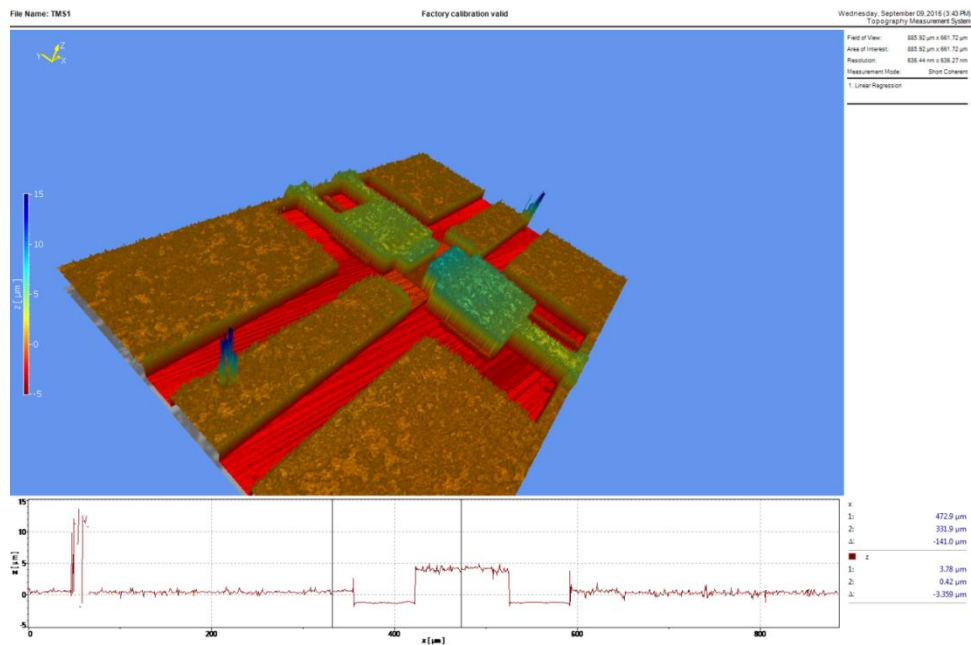
Figure 6.6: 3-D profile Optical profile of Switch.

The mechanical resonance frequency has been measured through Polytec Micro System Analyzer (MSA) 500 also called Laser Doppler Vibrometer (LDV) [91].

$$t_p = \left[2.88 \frac{V_p}{\omega_0 V} + 0.608 \frac{V_p^3}{\omega_0 V^3} + 0.29 \frac{V_p^5}{\omega_o V^5} + 0.17 \frac{V_p^7}{\omega_o V^7} + 0.11 \frac{V_p^9}{\omega_o V^9} \dots \right.$$
$$\left. + 0.07 \frac{V_p^{11}}{\omega_o V^{11}} \right]$$

(6.1)

$$\text{Release time } (t_r) = \frac{\pi}{2\omega_o}$$

(6.2)

The cantilever with single flexure has been used for measuring the mechanical resonance frequency as other side cantilever ground plane has been shorted to the actuation electrode due to the poor quality of deposited SiO_2.
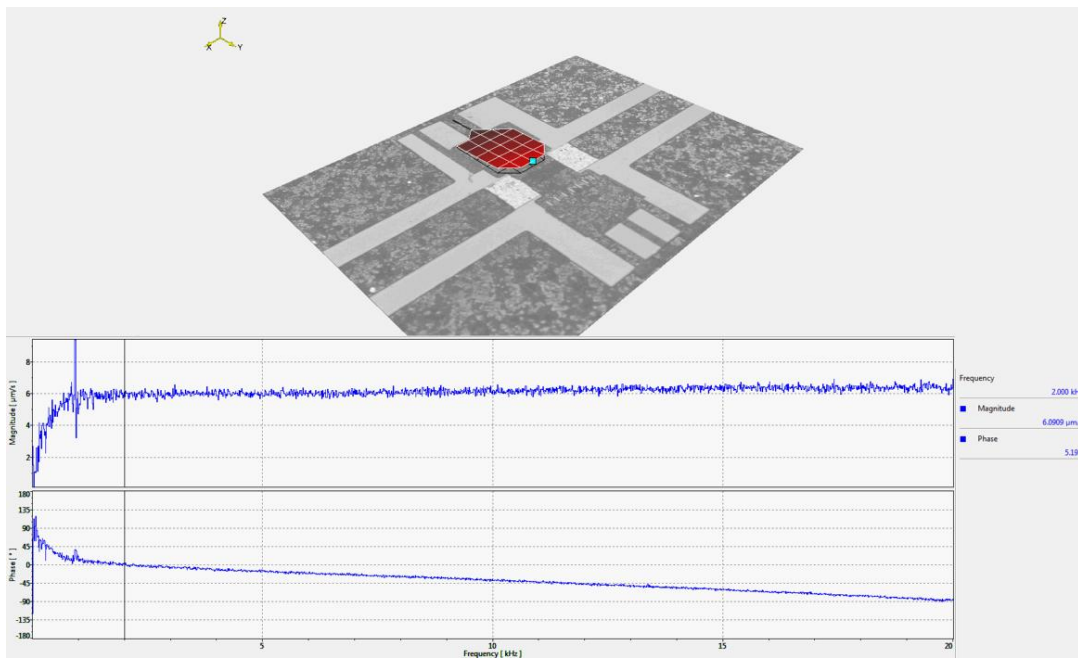
Figure 6.7: Measured mechanical resonant frequency of the cantilever.

Figure 6.7 shows the resonance frequency of the first mode. The first harmonic occurs at 2 kHz. The measured value of resonant frequency has been substituted in the equations (6.1) and (6.2) for calculating the pull-in time and release time. The left cantilever has a pull-in time of 33.44 ms at $V = V_p$, and release time of 12.50 ms.

C-V measurements provide the measure of pull-in voltage and capacitance of the switch in up-state and down-state. The capacitive switch exhibits low capacitance when the hanging structure is not actuated a large capacitance once the device is pulled down onto the transmission line by voltage application. The cantilever and transmission line had a

short circuit while doing C-V measurement due to the electrical breakdown of SiO_2 as shown in the Fig. 6.8 and thus C-V measurement had not been done.
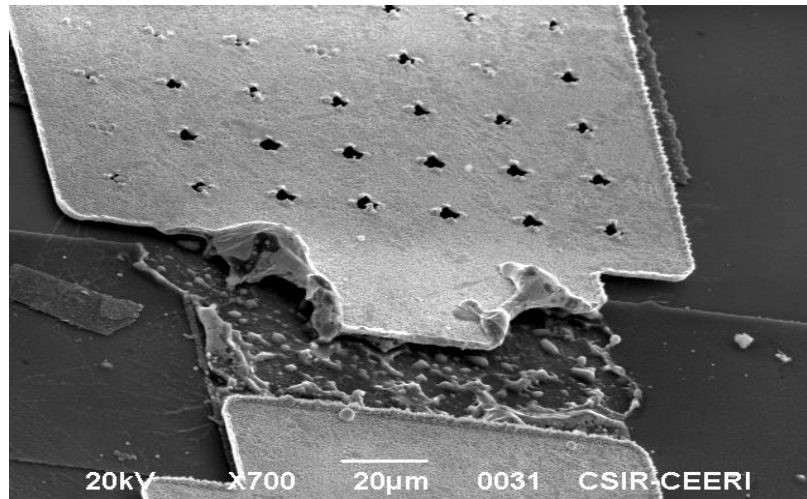
Figure 6.8: Short circuit due to the electrical breakdown of oxide under $C\text{-}V$ characteristics.

6.4 Conclusion

The switch fabrication process consisting of seven mask levels has been discussed briefly. It is observed that the quality of SiO_2 deposited is very critical as it can lead to the overall failure of the device. Under measurement section, physical parameters such gap between the transmission line and cantilevers, thickness of the transmission line have been measured through the 3D optical profile. The actual gap obtained is higher than the set value due to the residual stress. This results in higher pull-in voltage. Switch shows the mechanical resonant frequency of 2 kHz, which results in a pull-in time of 33.44 ms at $V = V_p$ and release time of 12.50 ms. The pull-in time can be decreased further by increasing the supply voltage beyond the pull-in voltage.

Chapter - 7

Conclusion and Future work

7.1 Conclusion

RF-MEMS has been identified as the most significant enabling technology in developing miniaturized telecommunication systems. RF-MEMS switches are the key components in the MEMS based architectures. From the design perspective, RF-MEMS switch requires a multidisciplinary approach. In mechanical domain, switches are implemented in the form of structures either fixed at one end or both ends and free to move in the perpendicular direction. In order to achieve low equivalent spring constant for the switches, various shapes of non-uniform cantilevers and bridges based structures have been investigated. A closed form analytical expression based on the 1-D model is derived to calculate the spring constant for the straight beam flexures based cantilevers type structure. The analytically calculated and simulated values agree within 10 %. In electromechanical domain, pull-in voltage and switching time have been investigated. A case study has also been explored through a common structure used for RF-MEMS switches. The switching time dependency on perforations in bridge, the ratio of the applied voltage to the pull-in voltage and materials with Young moduli and density varying in the range of $70 \leq E \leq 200$ and $2.7 \leq \rho \leq 19.3$ have been studied. The force balance equations of the 1-D model incorporating the gap dependency of electrostatic force have been used for the deriving the improved expression for the pull-in time. Further, the expression is also derived when the beam is stopped by transmission line before it touches the actuator, generally done to avoid stiction and enhance the reliability It is observed that material with high value of E/ρ should be used for movable structures to reduce the switching time. The results obtained through derived closed form expression differ less than 5 % to the 3-D FEM simulations, whereas the previous model's results vary from 10 % to 25 % when applied voltage is swept from V_p to $2V_p$.

In electrical domain, switch behavior is determined using the commercial available software. This approach lags in building the physical insight of the device and makes it necessary to build and study the behavior of the device through its lumped model. Thus, the electrical behavior of the capacitive shunt switches is discussed in terms of the

lumped *'R', 'L', 'C'* model. The devices are implemented in CPW configuration. A brief discussion on CPW provides a closed form analytical expression to synthesize CPW dimensions. In this thesis, various configurations have been designed and lumped electrical model parameters are extracted for capacitive shunt RF-MEMS switches. Their design approach and important outcomes are briefly concluded in the next few paragraphs.

For device based on the conventional approach, the switch is implemented with a non-uniform bridge structure with central overlap area of 310×90 μm^2 in order to have maximum isolation in *X*-band with insertion loss (< 0.3 dB) and pull-in voltage (< 15 V). In the improved version, considerable improvement in insertion loss has been seen as compared to the conventional switch. OFF-state response is approximately same for both the devices. Bandwidth is also increased around 2.5 times than that of the conventional switch, whereas input power is increased around 4 times without self bias and hold down problems. The pull-in voltage and switching time have also been reduced from 12.75 V to 11.75 V and 69.62 μs to 56.41 μs. The effect of using a high-*k* dielectric material (*HfO$_2$*) on the performance of shunt switches has also been explored. A compact device has been designed by interdigitizing the signal line with the actuation electrodes. Compactness has been further gained as high-*k* dielectric material requires less central overlap area compared to the low-*k* dielectric material for same frequency band operation. Significant improvement in the RF and electro-mechanical response has been achieved as compared to the conventional capacitive switch with *SiO$_2$*. Further switches with the same dimensions and masks having different dielectric material can be tuned to different frequency bands.

This thesis also presents novel multi-band reconfigurable shunt switches, where isolation optimum value has been tuned to the different frequency bands. A bridge structure anchored in between ground planes and attached to two cantilevers on either side has been used to implement the switch structure. This structure is used to inductively tune the isolation peaks in *X* and *K* bands which is not possible with conventional approach. The designed switch shows an insertion loss of 0.01 dB to 0.11 dB over the frequency range from 1 to 25 GHz. Isolation of 34.71, 34.33, and 40.7 dB has been observed at 10.4 GHz, 11 GHz and 21.4 GHz when the bridge is electrostatically actuated with either left, right or both cantilevers in the down-state respectively. The bridge structure shows a

pull-in voltage of 12.25 V and switching time of 34.40 μs, whereas the left and right cantilevers have 7.5 V and 57 μs.

For reducing the pull-in voltage and size of the switch a cantilever based design with symmetric and asymmetric structures on either side of the transmission line have been used to implement the device. With symmetric structure isolation optimum value has been tuned to C, X bands, whereas with asymmetric structures isolation optimum value has been tuned to C, X and K bands. We also worked on a combination of metal-to-metal contact switch and capacitive switch designed for wideband applications. For performance improvement asymmetric cantilever based capacitive shunt switch is used and the response has been compared with the conventional shunt device. The proposed design shows the insertion loss better than 0.35 dB and return loss below 13.96 dB up to 30 GHz as compared to 1.64 dB insertion loss and 6.14 dB of return loss with conventional switch. Isolation peaks of 75.33, 71.58 and 72.98 dB have been observed at 8.2, 7.3 and 15.5 GHz when left, right or both cantilevers are electrostatically actuated in the down-state respectively, whereas conventional switch has peak only at 7.0 GHz. As an application, cantilever based capacitive switch has used to implement the multiple throw switching device and response has been compared to the conventional approach based SPDT. Significant improvement has been observed in RF performance for SPDT implemented using cantilever based capacitive switch.

In summary, this thesis has demonstrated the design and fabrication feasibility of the multi-band reconfigurable capacitive shunt RF-MEMS switches with low actuation voltage ranging from 3 V to 12 V with the acceptable RF response (insertion loss < 0.1 dB, isolation > 20 dB) in the frequency range from 5-25 GHz. An ohmic switch has also been designed for dc to C-band application. The fabrication process is based on surface micro-machining with standard IC fabrication steps. Switch design concept has been validated using commercial simulation tools. Capacitive devices are combined with ohmic switch in order to implement the wideband switch. SPDT is also implemented with capacitive devices. Further, these switches are very likely to find use as MEMS varactors, tunable MEMS filters and phase shifters.

7.2 Future Work

RF-MEMS switch design involves optimization of various interdependent parameters. The change in one parameter typically leads to both favorable and unfavorable effects, therefore trade-offs between the design parameters are necessary. In order to achieve the most desirable performances, switch dimensions can be optimized using the various optimization techniques. MEMS switches are very sensitive to humidity and contaminations and therefore, must be packaged using hermetic seals in a dry environment. The fabrication process also needs more efforts to improve the overall yield. However, general understanding and accessibility of design tools based on multi-domain approach have been improved over the last few years. Some future works that can be explored are as follows:

- Reliability studies of RF-MEMS switches under different temperatures and mechanical shocks.

- Multilayer approach to compensate residual stress related deformation may be incorporated in the design of cantilever based switches.

- Study and implementation of different packaging methodologies for RF-MEMS switches.

- Fabrication of high-k dielectric based (HfO_2) based capacitive switches.

- Design of switch matrices and phase shifters using the asymmetric cantilevers based capacitive switch as a basic building block.

- Variable capacitor application of tunable switches.

- Study of high speed RF-MEMS switches.

References

[1]   *An introduction to MEMS (micro-electromechanical systems)," Prime FaradayTechnology Watch*,Available:http://www.primetechnologywatch.org.uk.

[2]   N. Maluf, *An Introduction to Micromechanical Systems Engineering, Microengineering*, *2ⁿᵈ Edition*, Artech House, Norwood, M.A., 2000.

[3]   S. D. Senturia, "Feynman revisited," in *Micro Electro Mechanical Systems*, MIT, Cambridge, MA, USA, 1994, pp. 309-312.

[4]   S. D. Senturia, *Microsystem Design*, *1ˢᵗ Edition*, Kluwer Academic Publishers, Boston, 2002.

[5]   J. A. Walraven, "Failure mechanisms in MEMS," in *IEEE International Test Conference (ITC)*, Albuquerque, N.M, USA, 2003, pp. 828-833.

[6]   G. M. Rebeiz, *RF MEMS: Theory, Design, and Technology*, *1ˢᵗ Edition*, John Wiley & Sons, New York, 2004.

[7]   L. P. Katehi, J. F. Harvey, and E. Brown, "MEMS and Si micromachined circuits for high-frequency applications," *IEEE Transactions on Microwave Theory and Techniques,* vol. 50, pp. 858-866, 2002.

[8]   L. E. Larson, R. H. Hackett, M. A. Melendes, and R. F. Lohr, "Micromachined microwave actuator (MIMAC) technology-a new tuning approach for microwave integrated circuits," in *Microwave and Millimeter-Wave Monolithic Circuits Symposium Digest*, Boston, MA, USA, 1991, pp. 27-30.

[9]   K. Rangra, "Electrostatic low actuation voltage RF MEMS switches for telecommunications," PhD, International Doctorate School in Information and Communication Technologies, University of Trento, Italy, 2005.

[10]   R. J. Richards and H. J. De Los Santos, "MEMS for RF/microwave wireless applications: the next wave," *Microwave Journal,* vol. 44, pp. 1-6, 2001.

[11] H. A. Tilmans, W. D. Raedt, and E. Beyne, "MEMS for wireless communications:'from RF-MEMS components to RF-MEMS-SiP'," *Journal of Micromechanics and Microengineering,* vol. 13, pp. 139-163, 2003.

[12] V. K. Varadan, K. J. Vinoy, and K. A. Jose, *RF MEMS and Their Applications*, *1ˢᵗ Edition*, John Wiley & Sons, England, 2003.

[13] M. Daneshmand, "Multi-Port RF MEMS switches and switch matrices," PhD, Electrical and Computer Engineering, University of Waterloo, 2006.

[14] *Advance Switch Technology*. Available: http://www.astswitch.com.

[15] G. M. Rebeiz and J. B. Muldavin, "RF MEMS switches and switch circuits," *IEEE Microwave Magazine,* vol. 2, pp. 59-71, 2001.

[16] K. Rangra, B. Margesin, L. Lorenzelli, F. Giacomozzi, C. Collini, M. Zen*, et al.*, "Symmetric toggle switch-a new type of rf MEMS switch for telecommunication applications: Design and fabrication," *Sensors and Actuators A: Physical,* vol. 123, pp. 505-514, 2005.

[17] P. Grant, M. Denhoff, and R. Mansour, "A comparison between RF MEMS switches and semiconductor switches," in *International Conference on MEMS, NANO and Smart Systems (ICMENS)*, Banff, Alberta-Canada, 2004, pp. 515-521.

[18] C. L. Goldsmith, Z. Yao, S. Eshelman, and D. Denniston, "Performance of low-loss RF MEMS capacitive switches," *IEEE Microwave and Guided Wave Letters,* vol. 8, pp. 269-271, 1998.

[19] Z. J. Yao, S. Chen, S. Eshelman, D. Denniston, and C. Goldsmith,"Micromachined low-loss microwave switches," *Journal of Microelectromechanical Systems, ,* vol. 8, pp. 129-134, 1999.

[20] F. Giacomozzi, C. Calaza, S. Colpo, V. Mulloni, A. Collini, B. Margesini*, et al.*, "Development of high con coff ratio RF MEMS shunt switches," *Romanian Journal of information science and technology,* vol. 11, pp. 143-151, 2008.

[21]   Y. Zhang, K. Onodera, and R. Maeda, "RF micro-electro-mechanical systems capacitive switches using ultra thin hafnium oxide dielectric," *Japanese journal of applied physics,* vol. 45, pp. 300-304, 2006.

[22]   K. Maninder, A. Sharma, K. Rangra, D. Kumar, and S. Singh, "Design of compact, high capacitance ratio MEMS switches for X-Band applications using high-*k* dielectric materials," in *NSTI-Nanotech,* Anaheim, California, 2010, pp. 332-335.

[23]   J. Y. Park, G. H. Kim, K. W. Chung, and J. U. Bu, "Fully integrated micromachined capacitive switches for RF applications," in *IEEE MTT-S*, Boston, MA, USA, 2000, pp. 283-286.

[24]   J. Y. Park, G. H. Kim, K. W. Chung, and J. U. Bu, "Electroplated RF MEMS capacitive switches," in *International Conference on Micro Electro Mechanical Systems*, Miyazaki, 2000, pp. 639-644.

[25]   E. R. Brown, "RF-MEMS switches for reconfigurable integrated circuits," *IEEE Transactions on Microwave Theory and Techniques,* vol. 46, pp. 1868-1880, 1998.

[26]   K. Entesari, "Development of High Performance 6-18 GHz Tunable/Switchable RF MEMS Filters and Their System Implications," PhD, University of Michigan, 2006.

[27]   D. Dubuc, L. Rabbia, K. Grenier, P. Pons, O. Vendier, J. Graffeuil*, et al.*, "Original MEMS-based single pole double throw topology for millimeter wave space communications," in *European Microwave Conference*, Munich, 2003, pp. 979-982.

[28]   C. Goldsmith, J. Randall, S. Eshelman, T. Lin, D. Denniston, S. Chen*, et al.*, "Characteristics of micromachined switches at microwave frequencies," in *IEEE MTT-S*, San Franscisco, California, 1996, pp. 1141-1144.

[29]   M. Ulm, M. Reimann, T.Walter, R. Muller-Fiedler, and E. Kasper, "Capacitive RF MEMS switches for the W-band " in *European Microwave Conference*, London, UK, 2001, pp. 287–290.

[30]   S. Pacheco, C. T. Nguyen, and L. P. Katehi, "Micromechanical electrostatic K-band switches," in *IEEE MTT-S*, Baltimore, Maryland, 1998, pp. 1569-1572.

[31]   D. Peroulis, S. P. Pacheco, K. Sarabandi, and L. P. Katehi, "Electromechanical considerations in developing low-voltage RF MEMS switches," *IEEE Transactions on Microwave Theory and Techniques,* vol. 51, pp. 259-270, 2003.

[32]   C. Calaza, B. Margesin, F. Giacomozzi, K. Rangra, and V. Mulloni, "Electromechanical characterization of low actuation voltage RF MEMS capacitive switches based on DC CV measurements," *Microelectronic Engineering,* vol. 84, pp. 1358-1362, 2007.

[33]   C. Dai, H. Peng, M. Liu, C. Wu, and L. Yang, "Design and fabrication of RF MEMS switch by the CMOS process," *Tamkang Journal of Science and Engineering,* vol. 8, pp. 197-202, 2005.

[34]   H. Jaafar, O. Sidek, A. Miskam, and S. Korakkottil, "Design and simulation of microelectromechanical system capacitive shunt switches," *American Journal of Engineering and Applied Sciences,* vol. 2, pp. 655-660, 2009.

[35]   S. Jaibir, K. Nagendra, and D. Amitava, "Fabrication of low pull-in voltage RF MEMS switches on glass substrate in recessed CPW configuration for V-band application," *Journal of Micromechanics and Microengineering,* vol. 22, pp. 025001-025010, 2012.

[36]   D. Peroulis, S. P. Pacheco, and L. P. Katehi, "RF MEMS switches with enhanced power-handling capabilities," *IEEE Transactions on Microwave Theory and Techniques,* vol. 52, pp. 59-68, 2004.

[37]   M. Song, J. Yin, X. He, and Y. Wang, "Design and analysis of a novel low actuation voltage capacitive RF MEMS switches," in *International Conference on Nano/Micro Engineered and Molecular Systems*, Sanya, China, 2008, pp. 235-238.

[38]   F. Guo, Z. Zhu, Y. Long, W. Wang, S. Zhu, Z. Lai*, et al.*, "Study on low voltage actuated MEMS rf capacitive switches," *Sensors and Actuators A: Physical,* vol. 108, pp. 128-133, 2003.

[39]   C. L. Dai and J. H. Chen, "Low voltage actuated RF micromechanical switches fabricated using CMOS-MEMS technique," *Microsystem technologies,* vol. 12, pp. 1143-1151, 2006.

[40]   J. B. Muldavin and G. M. Rebeiz, "High-isolation CPW MEMS shunt switches. 1. Modeling," *IEEE Transactions on Microwave Theory and Techniques,* vol. 48, pp. 1045-1052, 2000.

[41]   J. B. Muldavin and G. M. Rebeiz, "High-isolation CPW MEMS shunt switches. 2. Design," *IEEE Transactions on Microwave Theory and Techniques,* vol. 48, pp. 1053-1056, 2000.

[42]   K. Kiang, H. Chong, C. Hwan, L. Lok, K. Elgaid, and M. Kraft, "Development of a low actuation voltage RF MEMS switch," PhD, School of Electronics and Computer Science, University of Southampton, 2008.

[43]   S. Shen, D. Becher, Z. Fan, D. Caruth, and M. Feng, "Development of broadband low actuation voltage RF MEM switches," *Active and Passive Electronic Components,* vol. 25, pp. 97-111, 2002.

[44]   S. D. Lee, B. C. Jun, S. D. Kim, and J. K. Rhee, "A novel pull-up type RF MEMS switch with low actuation voltage," *IEEE Microwave and Wireless Components Letters,* vol. 15, pp. 856-858, 2005.

[45]   S. Dey and S. K. Koul, "Design and development of a surface micro-machined push–pull-type true-time-delay phase shifter on an alumina substrate for Ka-band T/R module application," *Journal of Micromechanics and Microengineering,* vol. 22, pp. 125006-125026, 2012.

[46]   K. Maninder, K. Rangra, D. Kumar, and S. Singh, "Parametric optimization of symmetric toggle RF MEMS switch for X-band applications," *Int J Recent Trends Eng,* vol. 2, pp. 95-98, 2009.

[47]   F. Solazzi, "Novel Design Solutions for High Reliability RF MEMS Switches," PhD, International Doctorate School in Information and Communication Technologies, University of Trento, 2011.

[48]   H. Yoon, Y. Sha, P. K. Sharma, K. Vinoy, V. K. Varadan, and V. V. Varadan, "Performance improvement of rf MEMS capacitive switches with high-dielectric-constant materials," in *International Symposium on Smart Structures and Materials*, Newport Beach, CA, USA 2001, pp. 38-45.

[49]   A. Persano, A. Cola, G. De Angelis, A. Taurino, P. Siciliano, and F. Quaranta, "Capacitive RF MEMS switches with tantalum-based materials," *Journal of Microelectromechanical Systems,* vol. 20, pp. 365-370, 2011.

[50]   A. Persano, F. Quaranta, A. Cola, A. Taurino, G. De Angelis, R. Marcelli*, et al.*, "Ta_2O_5 Thin Films for Capacitive RF MEMS Switches," *Journal of Sensors,* vol. 2010, pp. 1-5, 2010.

[51]   T. Gupta, *Copper interconnect technology*, *1st Edition*, Springer Science & Business Media, New York, 2010.

[52]   B. R. Kumar and T. S. Rao, "High-k Gate Dielectrics of Thin Films with its Technological Applications–A Review," *International Journal of Pure and Applied Sciences and Technology,* vol. 4, pp. 105-114, 2011.

[53]   R. K. Sharma, A. Kumar, and J. M. Anthony, "Advances in high-k dielectric gate materials for future ULSI devices," *Journal of The Minerals, Metals & Material,* vol. 53, pp. 53-55, 2001.

[54]   G. K. Fedder, "Simulations of Micromechanical systems," Ph.D Dissertation, Department of Electrical Engineering and Computer Sciences, University of California, Berkley, 1994.

[55]   J. M. Gere and S. Timoshenko, *Mechanics of Materials*, *3rd Edition*, U.K., Springer Science & Business Media, 1991.

[56]   J. B. Muldavin and G. M. Rebeiz, "Nonlinear Electro-Mechanical Modeling of MEMS Switches," in *IEEE MTT-S*, 2001, pp. 2119-22.

[57]   M. Bao, *Analysis and design principles of MEMS devices*, *1st Edition*, Amsterdam, Elsevier, 2005.

[58]   D. Elata and V. Leus, "Switching time, impact velocity and release response, of voltage and charge driven electrostatic switches," in *International Conference on MEMS, NANO and Smart Systems*, 2005, pp. 331-334.

[59]   V. Leus and D. Elata, "On the dynamic response of electrostatic MEMS switches," *Journal of Microelectromechanical Systems,* vol. 17, pp. 236-243, 2008.

[60]   C. Liu, *Foundation of MEMS, 1ˢᵗ Edition*, Pearson Education, Inc., New Jersey, 2006.

[61]   G. Bartolucci, R. Marcelli, S. Catoni, B. Margesin, F. Giacomozzi, V. Mulloni, *et al.*, "An equivalent-circuit model for shunt-connected coplanar microelectromechanical system switches for high frequency applications," *Journal of Applied Physics,* vol. 104, pp. 084514-084521, 2008.

[62]   C. Wong, M. Tan, and K. Liew, "Electrical characterisation of RF capacitive microswitch," *Sensors and Actuators A: Physical,* vol. 102, pp. 296-310, 2003.

[63]   C. P. Wen, "Coplanar waveguide: A surface strip transmission line suitable for nonreciprocal gyromagnetic device applications," *IEEE Transactions on Microwave Theory and Techniques,* vol. 17, pp. 1087-1090, 1969.

[64]   R. N. Simons, *Coplanar waveguide circuits, components, and systems, 1ˢᵗ Edition,* John Wiley & Sons, New York, 2004.

[65]   Coplanar Waveguide Calculator, http:// www.microwave101.com/encyclopedia.

[66]   D. M. Pozar, *Microwave engineering, 3ʳᵈ Edition,* John Wiley & Sons, Singapore, 2009.

[67]   N. Tas, T. Sonnenberg, H. Jansen, R. Legtenberg, and M. Elwenspoek, "Stiction in surface micromachining," *Journal of Micromechanics and Microengineering,* vol. 6, pp. 385-397, 1996.

[68]   D. Bansal, A. Bajpai, P. Kumar, A. Kumar, M. Kaur, and K. Rangra, "Design and fabrication of a reduced stiction radio frequency MEMS switch," *Journal of*

Micro/Nanolithography, MEMS, and MOEMS, vol. 14, pp. 035002-035009, 2015.

[69]   R. Gaddi, M. Bellei, A. Gnudi, B. Margesin, and F. Giacomozzi, "Interdigitated low-loss ohmic RF-MEMS switches," in *Proceedings of NSTI-Nanotech*, 2004, pp. 327-330.

[70]   R. Mahameed, M. A. El-Tanani, and G. M. Rebeiz, "A zipper RF MEMS tunable capacitor with interdigitated RF and actuation electrodes," *Journal of Micromechanics and Microengineering,* vol. 20, pp. 035014-035019, 2010.

[71]   Y. Zhang, K. Onodera, and R. Maeda, "RF- Micro- Electro-Mechanical Sytems Capacitive Switches Using Ultra thin Hafnium Oxide Dielectric," *Japnese Journal of Applied Physics,* vol. 45, pp. 300-304, 2006.

[72]   M. Angira and K. Rangra, "Design and investigation of a low insertion loss, broadband, enhanced self and hold down power RF-MEMS switch," *Microsystem Technologies,* vol. 21, pp. 1173-1178, 2015.

[73]   D. Bansal, A. Kumar, A. Sharma, P. Kumar, and K. Rangra, "Design of novel compact anti-stiction and low insertion loss RF MEMS switch," *Microsystem technologies,* vol. 20, pp. 337-340, 2014.

[74]   J. B. Muldavin and G. M. Rebeiz, "High-isolation inductively-tuned X-band MEMS shunt switches," in *IEEE MTT-S International*, Boston, USA, 2000, pp. 169-172.

[75]   S. Fouladi and R. R. Mansour, "Capacitive RF MEMS Switches Fabricated in Standard 0.35-CMOS Technology," *IEEE Transactions on Microwave Theory and Techniques,* vol. 58, pp. 478-486, 2010.

[76]   A. Lucibello, E. Proietti, F. Giacomozzi, R. Marcelli, G. Bartolucci, and G. De Angelis, "RF MEMS switches fabrication by using SU-8 technology," *Microsystem technologies,* vol. 19, pp. 929-936, 2013.

[77]   M. Angira, G. M. Sundaram, K. Rangra, D. Bansal, and M. Kaur, "On the investigation of an interdigitated, high capacitance ratio shunt RF-MEMS switch

for X-band applications," in *NSTI -Nanotech*, Washington D.C, USA, 2013, pp. 189-192.

[78]   W. Fang and J. Wickert, "Determining mean and gradient residual stresses in thin films using micromachined cantilevers," *Journal of Micromechanics and Microengineering,* vol. 6, pp. 301-309, 1996.

[79]   A. Sharma, D. Bansal, M. Kaur, P. Kumar, D. Kumar, R. Sharma*, et al.*, "Fabrication and analysis of MEMS test structures for residual stress measurement," *Sensors & Transducers,* vol. 13, pp. 21-30, 2011.

[80]   T. Kang, J. Kim, J. Lee, J. Lee, J. Hahn, H. Lee*, et al.*, "Low-thermal-budget and selective relaxation of stress gradients in gold micro-cantilever beams using ion implantation," *Journal of Micromechanics and Microengineering,* vol. 15, pp. 2469-2478, 2005.

[81]   C. D. Patel and G. M. Rebeiz, "An RF-MEMS switch with mN contact forces," in *IEEE MTT-S International*, 2010, pp. 1242-1245.

[82]   T. Kang, J. Kim, J. Kim, K. Hwang, B. Lee, C. Baek*, et al.*, "Deformation characteristics of electroplated MEMS cantilever beams released by plasma ashing," *Sensors and Actuators A: Physical,* vol. 148, pp. 407-415, 2008.

[83]   B. Schauwecker, K.M. Strohm, T. Mack, W. Simon, and J.-F. Luy, "Serial combination of ohmic and capacitive RF MEMS switches for large broadband applications," *Electronics Letters,* vol. 40, pp. 1-2, 2004.

[84]   M. Angira and K. Rangra, "Performance improvement of RF-MEMS capacitive switch via asymmetric structure design," *Microsystem Technologies,* vol. 21, pp. 1447–1452, 2015.

[85]   C. T.-C. Nguyen, "Microelectromechanical components for miniaturized low-power communications," in *International Microwave Symposium*, Anaheim, California, 1999, pp. 48-77.

[86]   S. Cheng, P. Rantakari, R. Malmqvist, C. Samuelsson, T. Vaha-Heikkila, A. Rydberg*, et al.*, "Switched beam antenna based on RF MEMS SPDT switch on

quartz substrate," *IEEE Antennas and Wireless Propagation Letters,* vol. 8, pp. 383-386, 2009.

[87]   S. P. Pacheco, D. Peroulis, and L. P. Katehi, "MEMS single-pole double-throw (SPDT) X and K-band switching circuits," in *IEEE MTT-S*, Phoenix, AZ, USA, 2001, pp. 321-324.

[88]   A. Malczewski and B. Pillans, "Single-pole double-throw switches using capacitive MEMS switches," *International Journal of RF and Microwave Computer‑Aided Engineering,* vol. 14, pp. 383-387, 2004.

[89]   K. Beilenhoff, W. Heinrich, and H. L. Hartnagel, "Analysis of T-junctions for coplanar MMICs," in *International Microwave Symposium Digest*, 1994, pp. 1301-1304.

[90]   Optical Suraface Profiler, http://www.taylor-habson.com.

[91]   Polytec Micro System Analyzer (MSA) 500, http://www.polytec.com.

List of Publications

Journal Papers

1. **M. Angira**, G.M. Sundaram, K. Rangra,"Performance improvement of a Reconfigurable Series-Shunt Switch via asymmetric structure based RF-MEMS capacitive switch", *International Journal of Advances in Engineering Sciences and Applied Mathematics, Springer,* vol.7, pp. 198-203, 2015.

2. **M. Angira** and K. Rangra, "A novel design for low insertion loss, multi-band RF-MEMS switch with low pull-in voltage," *Engineering Science and Technology, an International Journal (EBSCO Indexed), Elsevier,* vol.19, pp.171-177,2016.

3. **M. Angira** and K. Rangra, "Performance improvement of RF-MEMS capacitive switch via asymmetric structure design," *Microsystem Technologies (SCI and Scopus Indexed), Springer,* vol. 21, pp. 1447–1452, 2015.

4. **M. Angira** and K. Rangra, "Design and investigation of a low insertion loss, broadband, enhanced self and hold down power RF-MEMS switch," *Microsystem Technologies (SCI and Scopus Indexed), Springer,* vol. 21, pp. 1173-1178, 2015.

5. **M. Angira**, G. Sundaram, and K. Rangra, "A Novel Approach for Low Insertion Loss, Multi-band, Capacitive Shunt RF–MEMS Switch," *Wireless Personal Communications (SCI and Scopus Indexed), Springer,* vol. 83, pp. 2289-2301, 2015.

6. **M. Angira** and K. Rangra, "A low insertion loss, multi-band, fixed central capacitor based RF-MEMS switch," *Microsystem Technologies (SCI and Scopus Indexed), Springer,* vol. 21, pp. 2259–2264, 2015.

Conference Papers

1. **M. Angira**, G. M. Sundaram, and K. Rangra, "Improved Design of RF-MEMS Series-Shunt Switch for Reconfigurable RF Front End Applications," **in** *International Conference on MEMS and Sensors*, **IIT, Madras**, 2014, pp. 1-2.

2. **M. Angira**, G. M. Sundaram, and K. Rangra, "A novel interdigitated, inductively tuned, capacitive shunt RF—MEMS switch for X and K bands applications**," in** *International Conference on Nano/Micro Engineered and Molecular Systems (NEMS)***, Hawaii, USA,** 2014, pp. 139-142.

3. **M. Angira**, G. M. Sundaram, and K. Rangra, "Design, Simulation and Analysis of a high Reliability Series Ohmic RF-MEMS Switch for Telecommunication Applications," **in** *International Conference on Control, Computing, Communication and Materials*, **Allahabad, India**, 2013, pp. 1-4.

4. **M. Angira**, G. M. Sundaram, K. Rangra, D. Bansal, and M. Kaur, "On the investigation of an interdigitated, high capacitance ratio shunt RF-MEMS switch for X-band applications," **in** *NSTI -Nanotech***, Washington D.C, USA**, 2013, pp. 189-192.

5. **M. Angira**, G. M. Sundram, and K. Rangra, "Design and pull-in voltage optimization of series metal-to-metal contact RF MEMS switch," **in** *International Conference on Computing, Communication and Applications (ICCCA)***, Dindigul, India**, 2012, pp. 1-4.

Brief Biography of the Candidate

Mahesh Angira received his B.E in Electronics and Communication Engineering in 2003 from Maharishi Dayanand University (M.D.U) and M.Tech degree in Microelectronics and VLSI Design from Kurukshetra University, Kurukshetra, in 2007. He is currently working as Lecturer in the Department of Electrical and Electronics Engineering, Birla Institute of Technology and Science (BITS), Pilani. He has around 10 years of teaching experience. His research interests focus on the area of RF-MEMS Devices such as switches, multiple throw Switches, inductors, capacitors, phase shifters, and resonators.

Brief Biography of the Supervisor

Dr. Kamaljit Rangra received his Ph.D. from University of Trento, Italy and Master degree in Microelectronicsfrom Birla Institute of Technology and Science (BITS) Pilani, India. He is currently working as Chief Scientist, Semiconductor Device Area at CSIR-Central Electronics Engineering Research Institute (CEERI), Pilani, Rajasthan.

His research area includes Radio frequency MEMS, MEMS based IR & Inertial Sensors and vacuum microelectronics. He has been associated with various projects such: (1) Design, fabrication & characterization of RF MEMS switches; (2) HRD under NPMASS Project (Maintaining Si-Wafer fabrication Facility for supporting HRD; (3) Innovative high-k dielectric RF-MEMS switch development; (4) Advanced Microsensors & Microsystems: Design, Development & Applications; (5) Design, development and packaging of RF MEMS switches; (6) Digital micro-mirror devices (DMD); (7) Development of Medium Power RF MEMS Ohmic Contact Switch and (8) Pattern Up Plating (PuP) process for MIC fabrication. Some of the projects have successfully been completed while a few are in progress.

His teaching responsibilities include- Professor AcSIR new Delhi, Ex-Adjunct Professor, Bengal Engineering and Science University, Shibpur (West Bengal) and Tutor/Resource person CSIR- Human Resource Development Centre, at Ghaziabad. He is also Associate Editor of ISSS Journal and reviewer for (i) International Journal of Applied Electromagnetics and Mechanics, IOS Press, The Netherlands; (ii) AEÜE - International Journal of Electronics and Communications (Elsevier B.V.); (iii) Elsevier Journal of Materials and Design.

He has about 80 international journal publications to his credit in addition to several conference proceedings. He has successfully guided two doctoral students and presently guiding nine Ph.D. candidates. He is Fellow of IETE (1998), Institution of Engineers (IE) 2014, Metrology Society of India (MSI) 2012, member and Secretary (local Chapter), Semiconductor Society of India (SSI) and Secretary (local Chapter) Indian Physics Association (1995).